# Crack patterns on uneven substrates

Dissertation

zur Erlangung des mathematisch-naturwissenschaftlichen

Doktorgrades

"Doctor rerum naturalium"

der Georg-August-Universität Göttingen

-

im Promotionsprogramm ProPhys

der Georg-August University School of Science  (GAUSS)

vorgelegt von

Pawan Nandakishore
Bangalore, India

Göttingen, 2015

**Betreuungsausschuss**

Prof. Dr. Stephan Herminghaus  (MPIDS Göttingen)

Prof. Dr. Eberhard Bodenschatz (MPIDS Göttingen)

Dr. Lucas Goehring  (MPIDS Göttingen)


**Mitglieder der Prüfungskommission**

Dr. Lucas Goehring  (MPIDS Göttingen)

Prof. Dr. Andreas Tilgner  (Univ. Göttingen)


**Weitere Mitglieder der Prüfungskommission**

Prof. Dr. Stephan Herminghaus  (MPIDS Göttingen)

Prof. Dr. Cynthia A. Volkert  (Univ. Göttingen)

Prof. Dr. Michel Milinkovitch  (Univ. Geneva)

Dr. Florian Rehfeldt  (Univ. Göttingen)


Tag der mündlichen Prüfung: 27/10/2015

# Abstract

Cracks patterns are influenced by the substrates beneath them. From buried craters to crocodile skin, crack patterns are found over an enormous range of length scales. Regardless of their scale, substrates can impart geometry and symmetry to a crack pattern. There are two central problems discussed in this thesis - how does an uneven substrate affect a crack pattern? how can crack patterns be quantified? To answer these questions, crack patterns are generated by drying mud slurries over sinusoidal and radially sinusoidal substrates. It is observed that as the thickness of the cracking layer increases, the crack patterns transition from wavy to ladder-like to isotropic. Four main measures of the crack pattern are introduced to quantify the observations - one parameter which measures the relative alignment of these crack networks, one parameter that measures the orientation of cracked regions, one parameter which measures uses the Manhattan metric to compare crack patterns and Fourier methods which are used to characterise the transitions between crack pattern types. These results are explained these results with a model, based on the Griffith criteria of fracture. This model suggests that there is a transition region between wavy to ladder-like cracks. The metrics developed here and results can be adapted to any connected networks of cracks.

# Contents

# Chapter 1

# Introduction

Fracture patterns are common in nature. From graben patterns on the surface of Mercury to crack patterns in thin films, they cover a spectrum of length scales. Everyday examples of fracture patterns can be seen in mud puddles, drying paint, rocks, glaze in ceramics. Despite their prevalence, little is known about what influences the geometry and topology of a crack pattern. A crack pattern generally forms atop a substrate, the substrate holds the cracking material and when stresses build up, fractures in the cracking material occur, these fractures spread till they terminate at a boundary and newer fractures emerge and connect with the older cracks. In case of mud puddles and paint cracks, it is the drying that drives the mud or the paint to develop stresses within them, causing them to crack.

The current work aims to better understand how substrates affect crack patterns by achieving two goals -

- To quantify the effect of the substrates on crack patterns.

- To define new measures to measure a crack pattern.

The attempt is to develop general methods for analysing crack patterns and apply it to the current experimental system to study the effect of non flat substrate. The substrate generally imparts symmetry and orientation onto a crack pattern, hence any quantification must account for this in order to effectively describe a crack pattern.

In order to achieve the goals above, crack patterns are generated by drying clay slurries on sinusoidal and radially sinusoidal plates and studied. There are three control parameters to the problem, the amplitude and wavelength of the sinusoidal and radially sinusoidal plate and the layer height of the deposited slurry. Various parameters are defined to quantify crack patterns, these parameters are measured for crack patterns generated at increasing layer heights and compared to a numerical model.

The base unit of a crack pattern is a single crack, hence the physics of fracture and formation is essential in understanding how fracture patterns are influenced by the substrate. The physics of fracture comes under the purview of fracture mechanics which has long been a traditional engineering disciple. Fracture mechanics is a study of the failure of materials. It looks at formation of cracks and dynamics of crack propagation.

In the next few sections starting with basic elasticity, some simple ideas in fracture mechanics will be presented. Crack patterns formed due to mud cracks are discussed as a model system followed by a collection of examples highlighting crack patterns at various length scales. These examples are discussed in terms of how substrates impart symmetry and orientation onto a crack pattern. In some cases, the substrate can also be used to control the formation of cracks and crack pattern, these examples are also discussed.

## 1.1 Linear elasticity

Fracture is a complex process and depends on a material's structure. A simple example - take a chocolate bar and apply force on each end of the bar and the bar breaks, or pull on a sheet of plastic from any two ends and observe as the sheet comes apart into two pieces.

The chocolate falls under the category of brittle materials while the plastic sheet behaves like a ductile material.

Ductile materials undergo plastic deformation - they will remember the deformation even after the applied loading has been removed. Ductile materials do not easily fracture under stress. Deformations change the shape of a ductile material, this shape change is non reversible. A common example of ductile material is copper, which can be drawn out into long wires.

Brittle materials generally fracture under the influence of stress. For brittle materials like ceramics and plastics (Acrylic, PMMA), the threshold for deformation is lower than that of ductile materials.

Despite being structurally different (the chocolate has continuous structure compared to the fibrous structure of a wooden plank), two materials in the same category (brittle vs ductile) break in a similar manner. This hints towards the existence of underlying principles which govern how materials in each category deform and fail.

In order to understand how materials fail it is necessary to know how they will deform and behave under the influence of an external loading. The study of deformations and the subsequent effects comes under the theory of elasticity. In many ways, elasticity theory provides the tools required to talk about fracture mechanics. Hence, basic ideas about elasticity are discussed in this section. The core focus is on the strain and stress tensors, later few ideas about two dimensional elasticity are discussed as well.

### 1.1.1 Strain

The deformation of a body under the influence of an external force can be described by the strain tensor [85, 77, 55] -

$$
e_{ij} = \begin{pmatrix} e_x & e_{xy} & e_{xz} \\ e_{yx} & e_y & e_{yz} \\ e_{zx} & e_{zy} & e_z \end{pmatrix},
\tag{1.1}
$$

where the strain tensor components contain three normal strains $e_x, e_y$ and $e_z$ and three

shear strains $e_{xy}, e_{yz}$ and $e_{xz}$. The strain tensor is symmetric since it can be shown that $e_{ij} = e_{ji}$ [77, 55] where $i$ and $j$ are the components $x, y, z$. The notation $e_i$ represents $e_x, e_y$ or $e_z$, and the notation $e_{ij}$ represents $e_{xy}, e_{yz}$ or $e_{xz}$. It is also important to note that the first index in $e_{xy}$, refers to the surface normal and the second index points to the direction of deformation. The strain tensor can be expressed in terms of displacements where

$$e_{ij} = \frac{1}{2}\left(\frac{\partial u_j}{\partial x_i} + \frac{\partial u_i}{\partial x_j}\right), \tag{1.2}$$

where the $u_i$ and $u_j$ are displacements of the body.

For a bar with its long axis lying along the $x$ direction (figure 1.1 (a)), under the influence of a force $F_x$ and for small deformation, the component $e_x$ represents the extension per unit length of the bar along the $x$ axis. $e_x$ is positive when the bar is elongated due to force $F_x$, and negative when under compression. In figure 1.1 (a) the force $F_x$ lies parallel to the normal vector of $CD$. Hence $e_x$ is known as normal strain. The component $e_{xy}$ of the strain tensor is $e_{xy} = 1/2\gamma_{xy}$ (figure 1.1 (b)) where $\gamma_{xy}$ is the engineering strain. The shear strain in the block is proportional to the change in angle of the cube $\gamma_{xy} \approx \phi$. The angle $\phi$ is the change in the angle of the block $EFGH$ which is given by $\phi = \pi/2 - \theta$ or $\phi = \alpha + \beta$. This relation holds for small angles, when $\alpha \approx \tan\alpha$, which can be only true for $\alpha << 1$, the same condition holds for $\beta$ [77, 55]. All other components of the strain tensor can be defined in a similar fashion. The small angles condition means that the definition of the shear strain as the sum of $\alpha$ and $\beta$ is only valid for small strains.

The deformation of a body leads to build up of internal forces with within the body. These internal forces can be represented using the stress tensor.
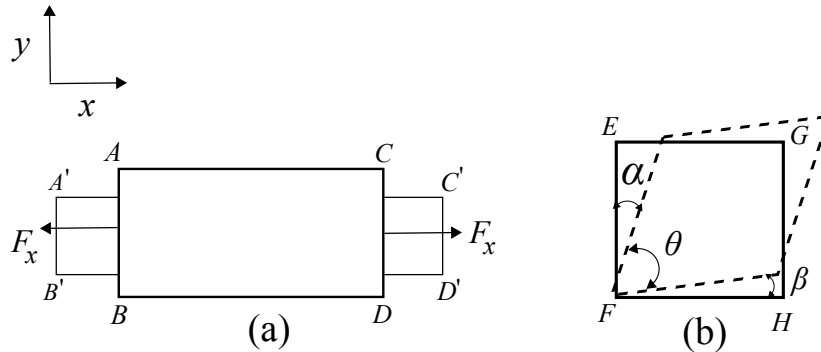


Figure 1.1: Normal strain and shear strain. In (a) a bar which lies along the $x$ axis is being pulled apart by a force $F_x$ the normal strain $e_x$ can expressed as $(A'C' - AC)/AC$ which is the extension per unit length. Figure (b) shows the deformation of a block $EFGH$ where the engineering strain $\gamma_{xy}$ can be expressed as the change in the angle of the block.

## 1.1.2 Stress

Points within a material body respond to deformations by developing internal forces which try to restore a body to equilibrium. Take for example a volume element of a 3 dimensional bar similar to the one in figure 1.1 (a), under the influence of a $F_x$. Internal forces will develop

within the body in response to the extension of the bar. The sum of all the forces within the bar must cancel out to zero since the bar is at rest. This means that forces between the various volume elements, according to Newton's 3rd law must cancel out. This is essential to express the next step where the forces on the volume can be expressed as forces on a surface [77, 55] -

$$\frac{\partial \mathbf{T^n}\left(\mathbf{x}\right)}{\partial \mathbf{x}} = \iint_S \mathbf{T^n}\left(\mathbf{x}\right)dS, \tag{1.3}$$

where $\mathbf{T^n}\left(\mathbf{x}\right)$ is the traction vector. For a cross section the bar, the surface $S$ is the surface that bounds the entire body. The notation $\mathbf{T^n}$ is used to represent $\mathbf{T^n} = [\overrightarrow{\mathbf{T^x}}, \overrightarrow{\mathbf{T^y}}, \overrightarrow{\mathbf{T^z}}]$ where each of the components can be written as [77] -

$$\overrightarrow{\mathbf{T^x}} = \sigma_x \hat{\mathbf{x}} + \sigma_{xy} \hat{\mathbf{y}} + \sigma_{xz} \hat{\mathbf{z}},$$
$$\overrightarrow{\mathbf{T^y}} = \sigma_{yx} \hat{\mathbf{x}} + \sigma_y \hat{\mathbf{y}} + \sigma_{yz} \hat{\mathbf{z}}, \tag{1.4}$$
$$\overrightarrow{\mathbf{T^z}} = \sigma_{zx} \hat{\mathbf{x}} + \sigma_{zy} \hat{\mathbf{y}} + \sigma_z \hat{\mathbf{z}},$$

where the $\sigma$'s can be written as -

$$\sigma = \begin{pmatrix} \sigma_x & \sigma_{xy} & \sigma_{xz} \\ \sigma_{yx} & \sigma_y & \sigma_{yz} \\ \sigma_{zx} & \sigma_{zy} & \sigma_z \end{pmatrix}, \tag{1.5}$$

and $\sigma$ is the stress tensor. Each component of the traction vector represents three components of the stress tensor ( equation 1.4). These components of the stress tensor are visualized in figure 1.2. It is important to note that the traction vector is defined with respect to a surface normal. In figure 1.2, for a normal vector $\vec{\mathbf{n}} = \hat{\mathbf{x}}$ which refers to a plane in $yz$, there will be only one component of the traction vector. This vector contains three component of the stress tensor which will be $\sigma_x, \sigma_{xy}, \sigma_{xz}$. The traction vector is essentially a surface force density which is integrated over the surface S bounding a material body to give the resultant force on the body.
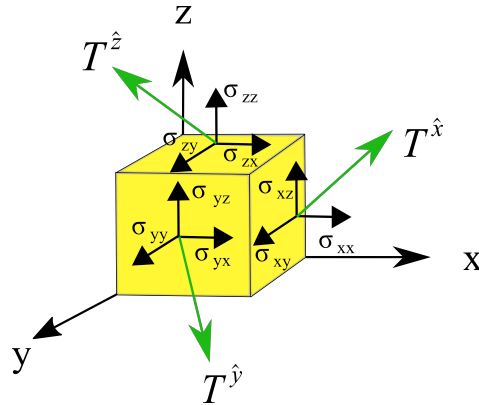


Figure 1.2: Traction vector and its components. Components of traction vector $\mathbf{T^n} = [\overrightarrow{\mathbf{T^x}}, \overrightarrow{\mathbf{T^y}}, \overrightarrow{\mathbf{T^z}}]$, where each component of the traction vector is expanded upon on volume element and shows the components of the stress tensor. Figure adopted from [77]

The $\sigma_i$ are all normal stresses and $\sigma_{ij}$ are shear stresses. Similar to the strain tensor, the stress tensor is symmetric, hence $\sigma_{ij} = \sigma_{ji}$.

Going back to the example of the bar in figure 1.1 (a). When the bar is pulled and held at rest, the forces on the bar balance out and the net force is zeros. If there were unbalanced forces in the bar, it would deform to account for them. Apart from the applied loading, the bar is also balances gravity, hence it is possible to write for any volume element of the bar [55]

$$\nabla \cdot \sigma + \rho g = 0. \tag{1.6}$$

This states that the sum of all forces acting on the body is zero, these forces are- internal stresses that balance out the applied loading and gravity. This is a necessary condition for the body to remain at rest.

Apart from gravity, there can be other external body forces acting on the body. These body forces (examples include magnetic forces) can be generalized and the above equation can be written explicitly as [77] -

$$\frac{\partial \sigma_{xx}}{\partial x} + \frac{\partial \sigma_{xy}}{\partial y} + \frac{\partial \sigma_{xz}}{\partial z} + F_{Bx} = 0,$$
$$\frac{\partial \sigma_{yx}}{\partial x} + \frac{\partial \sigma_{yy}}{\partial y} + \frac{\partial \sigma_{yz}}{\partial z} + F_{By} = 0, \tag{1.7}$$
$$\frac{\partial \sigma_{zx}}{\partial x} + \frac{\partial \sigma_{zy}}{\partial y} + \frac{\partial \sigma_{zz}}{\partial z} + F_{Bz} = 0,$$

where the body forces have three components, $\tilde{\mathbf{F}}_B = F_{Bx}\hat{\mathbf{x}} + F_{By}\hat{\mathbf{y}} + F_{Bz}\hat{\mathbf{z}}$. In the special case where body force is gravity acting in the $y$ direction according to figure 1.1 (a), then $F_{Bx} = F_{Bz} = 0$ and the only body force component remaining will be $F_{By} = \rho g$.

The set of equations present above are known as the equilibrium equations since they describe the equilibrium condition for a material body. They are crucial in the study of elasticity of a material since by solving the equilibrium equation with appropriate boundary conditions, it is possible to calculate the various stress acting on the body. This is relevant to fracture mechanics since it is the build up of stresses within a body that cause fracture. If the applied loading in figure 1.1 (a) were to exceed a threshold value then the internal stresses in the material will be large enough to break bonds between the individual molecules causing a crack to be initiated. Hence, an accurate description of the stresses in a material due to the applied loading is needed to predict the threshold value where fractures can be initiated.

So far, stress and strain have been looked at separately, however it can be shown that stress and strain are related. For an isotropic material, the relationship between the strain and the stress is expressed as [77, 55]

$$\sigma_{ij} = \lambda e_{kk}\delta_{ij} + 2\mu e_{ij}, \tag{1.8}$$

where $\lambda$ and $\mu$ are elastic constant. $\lambda$ and $\mu$ are the Lamé constants. The product $e_{kk}\delta_{ij}$ represents the diagonal components of the strain tensor. A note on notation, $\sigma_{ij}$ here represents all the terms of the stress tensor where if $i = j$ refers to the normal stresses, whereas $i \neq j$ refers to the shear stresses. The above equation means the internal stresses in a material can be expressed in terms of a material's elastic properties, and in terms of the strain in the material. It is interesting to note that normal stress in a material are dependent on both elastic

constants whereas the shear stresses are related to the strains by only the shear modulus. For example, $\sigma_x$ is dependent on the three normal strains $e_x, e_y$ and $e_z$ and on $\lambda$ and $\mu$, whereas $\sigma_{xy} = 2\mu e_{xy}$. Equation 1.8 also suggests that if stress is applied along one of the coordinate axis there will be strain in all coordinate axis. This is represented in figure 1.1 (a) where the stresses within the bar in the $x$ direction cause displacement and strain in the $y$ direction as well. The above equation can also be expressed in terms of the strain [77, 55]-

$$e_{ij} = \left(\frac{1+\nu}{E}\sigma_{ij}\right) - \frac{\nu}{E}\sigma_{kk}\delta_{ij}. \tag{1.9}$$

Here $\nu = \lambda/[2\,(\lambda + \mu))]$ is called the Poisson's ratio and $E = \mu\,(3\lambda + 2\mu)/\,(\lambda + \mu)$ is the Young's modulus.

The description of stress and strain according to equations 1.1 and 1.5 are three dimensional. Sometimes, a problem in elasticity can be reduced to a two dimensional version. This approach is also commonly used in fracture mechanics to simplify a system making it easier to analytically solve the equilibrium equations (equation 1.7) and acquire the stresses around a crack. Next, a two dimensional formulation of elasticity is presented.

## 1.2  Two dimensional formulation of elasticity

The formalism of elasticity, which has been discussed so far, is for three dimensions. However, for many systems a two dimensional formulation of elasticity is sufficient and captures the essential physics. Two dimensional elasticity is also commonly used in fracture mechanics. Typically a plane stress condition is used to solve the stress in a film due to cracking.

Linear elasticity can be reduced to two dimensions confining all the strains or stresses to a single plane ([77, 84]). The first condition to be discussed will be plane strain which is an approximation useful for a thick plate. These are plates which are long in the $z$ direction compared to the dimensions of the plate in the $xy$ plane. Under this condition, the strain tensor becomes

$$\mathbf{e} = \begin{pmatrix} e_x & e_{xy} & 0 \\ e_{yx} & e_y & 0 \\ 0 & 0 & 0 \end{pmatrix}. \tag{1.10}$$

The $z$ direction strain tensor components are zero hence the strain tensor becomes two dimensional. Normally for a thick plate, applying a strain in the $xy$ direction would also cause a strain in the $z$ direction, this is known as Poisson's effect. Take a 3 dimensional version of the bar in figure 1.1 (a), where the force is being applied in the $x$ direction, if the height of bar which is its dimension in the $z$ direction is very large compared to the $x$ and $y$ dimensions, the strain tensor components $e_z, e_{yz}, e_{xz}$ would be very small and since the strain tensor is symmetric, $e_{zy}, e_{zy}$ would also be small. Mathematically, the strain tensor for the thick plate can be simplified be setting the $z$ components of the strain tensor to zero.

The stress tensorfor the plane strain condition can be written using equation 1.8-

$$\sigma = \begin{pmatrix} \sigma_x & \sigma_{xy} & 0 \\ \sigma_{yx} & \sigma_y & 0 \\ 0 & 0 & \nu\left(\sigma_x + \sigma_y\right) \end{pmatrix}, \tag{1.11}$$

where $\nu$ is Poisson's ratio. Despite there being no strain in the $z$ direction, the normal stress in the $z$ direction is non zero. Hence, a plane strain condition does not mean that the stress in the body will be confined to a plane.

Suppose, now the height of the 3 dimensional bar is reduced from being very large in the $z$ direction to very small compared to the dimensions of the bar in the $xy$ plane. Such a condition represents a thin film. For thin films, only stress in the $xy$ plane are relevant and the stress in the $z$ direction can be ignored. The stress tensor for plane stress condition becomes [77]

$$\sigma = \begin{pmatrix} \sigma_x & \sigma_{xy} & 0 \\ \sigma_{yx} & \sigma_y & 0 \\ 0 & 0 & 0 \end{pmatrix}. \tag{1.12}$$

For thin films, the normal stress and shear stress in the $z$ direction will be negligible hence, there are no $z$ components of the stress tensor. The strain tensor under the plane stress condition becomes[77]

$$\mathbf{e} = \begin{pmatrix} e_x & e_{xy} & 0 \\ e_{yx} & e_y & 0 \\ 0 & 0 & -\dfrac{\nu}{1+\nu}\left(e_x + e_y\right) \end{pmatrix}. \tag{1.13}$$

Here the $z$ component of the strain is non-zero, which means that regardless of height of the film being small the strains in the $z$ direction will still present.

Plane strain and plane stress are commonly used in fracture mechanics. Plane strain conditions are normally used to solve the problem of a crack traversing in a film bonded to a rigid substrate, moving parallel to the direction of a uni-axial stress. Solutions to such problem are given by Beuth [12]. Plane stress is commonly used in conditions where the crack propagates along the surface normal. A simple example is the tearing of a paper sheet, if the paper sheet were placed in the $xy$ plane and a loading was applied in the $x$ direction, a crack would initiate and propagate in the $xy$ plane. Since the sheet is thin, a plane stress formulation must be used to solve for the stress and strain with the sheet.

The tearing of paper sheet is a common example of fracture. An interesting question that arises when studying the tearing of paper is under what conditions will a tear in the paper propagate? Two methods are discussed in the next section which answer this question.

## 1.3   Driving a single crack

Crack growth can be explained using an energy balance argument. This model was presented by Alan Griffith (1921) expresses the total energy of a crack in a plate under uni-axial loading perpendicular to the direction of crack propagation [40]. The total energy of such a system is a product of the strain energy released due to crack growth and the amount of energy

required to new surfaces due to cracking. Strain energy in the body is built up due to the applied loading, it is a product of the strain and stress in the body $U_E = (1/2)\sigma_{ij}e_{ij}$ [77]. The amount of energy required to create new surfaces is propotional to the length of the crack and is given by $U_s = 2\gamma a$ [57] where $\gamma$ represents the surface energy per unit area and $a$ is the length of the crack. The term $\gamma a$ is multiplied by 2 to account for the two surfaces created. The total energy can be written as $U = U_E + U_s$ [57]. A threshold can be defined by taking the first derivative of $U$ with respect to the crack length and setting this this to zero $dU/da = 0$. This condition is known as the Griffiths criteria[57, 37]. A crack that meets the Griffiths threshold will only propagate if applied loading is increased, above this threshold a crack will keep propagating without the need for an external applied loading.

While the Griffith criteria are illuminating with respect crack propagating, they are not easily applicable to systems since they require the calculating of the total energy without taking into account dissipative forces. A alternate approach was put forward by Irwin (1957) where he considered crack tips as points where stresses are concentrated. He defined the criteria for crack extension in terms of the amount of stress at the crack tip. He introduced the idea of the stress intensity factor which can be used to predict the point of fracture. The stress intensity factor is dependent on the the size of the crack, geometry of the body in which the crack is propagating, and is proportional to the stress in the cracking body. The benefit of this approach is that the stress intensity factors can be empirical acquired and used to predict when a material will crack further. The stress intensity factor breaks up crack extension into three different modes. A sheet of paper lying in the $xy$ plane can be torn in three ways- first it can be pulled apart by a uni-axial force in the $xy$ plane, which is equivalent to applying a normal stress perpendicular to the direction of crack propagation. This mode which cause the crack to grow in a straight line is called opening. Second method is by applying a shear stress, this mode is know as sliding. A third method is to tear the sheet out of plate. This means a loading is applied in the $z$ direction to cause the sheet to tear out of its plane. This mode is known as tearing. The three modes of fracture capture the different ways cracks can extend into a material.

While the stress concentration approach is useful in expressing the stress around a crack tip, is generally limited in use, since it cannot address situations like dynamic fracture processes, where cracks spontaneously propagated fast, wavy cracks where a crack oscillates back and forth around a direction of propagation or the spontaneous splitting of the crack tip. Furthermore, multiple cracks may be created in a material, and as these cracks grow they may interact and intersect with each other which leads to the formation of a crack pattern. Such is the case with the system of mud cracks which is being studied in this thesis.

### 1.3.1 Mud cracks

So far the discussion has been focused on a single crack driven by an uni-axial external applied loading. Mud cracks differ from the above since mud cracks do not have uni-axial loading conditions, they can meander and they interact and intersect with other cracks. In drying mud puddles, cracks intersect and form complex geometries making it difficult to apply the

ideas like the Griffith criteria or stress concentration factor in order to understand how cracks will propagate in the system. Nevertheless, energy arguments like the Griffiths criteria can be used as a guide to understand how cracks extend in mud puddles. Before discussing the formation of crack patterns, the mechanism driving crack formation in mud is discussed.

The driving force behind the formation of mud cracks is the internal stresses built up due to evaporation of water within pores. In wet mud, a network of clay particles form the frame of a porous network filled with water. The pores of the network are filled with water; evaporation causes the water to recede creating tiny menisci within the pores. The pressure difference at the air water interface leads to contraction of the clay network. Since the clay network adheres to a boundary, the clay network resists contraction, which leads to the build up of internal stresses in the material [13, 37]. The internal stress of such a network are represented as an effective stress $\bar{\sigma} = \sigma_{ij} - p\delta_{ij}$ [13] where $\sigma_{ij}$ is the stress in the clay network and the $p$ is the capillary pressure. The pressure $p$ is positive for compression hence it is subtracted from the stress in the clay network. For a drying slurry the pressure becomes more and more negative over time hence the effective stress in the porous medium increases. The term $p\delta_{ij}$ comes from the assumption that there are no shear stresses in the network due to the capillary forces because the drying slurry is assumed to be isotropic [13].

A crack can emerge from defects within the drying slurry. The build up of effective stress causes the crack to release the stress locally. The first crack propagates until it hits the boundary and terminates. Meanwhile a second crack will emerge and start propagating, if it approaches close to the first crack, it bends and intersects the first crack at approximately 90°. Figure 1.3 shows an example of a T-junction in a mud crack generated on a flat substrate. This is because cracks release more stress normal to the direction of propagation then in their direction propagation. Many cracks emerge and propagate as the slurry dries, forming junctions as they intersect with each other. This process continues until the average spacing between the cracks reaches proportional to the height of dried slurry, at this point the cracks do not propagate further but starting opening. This is the point of crack saturation, where the cracks can grow no further.[6]
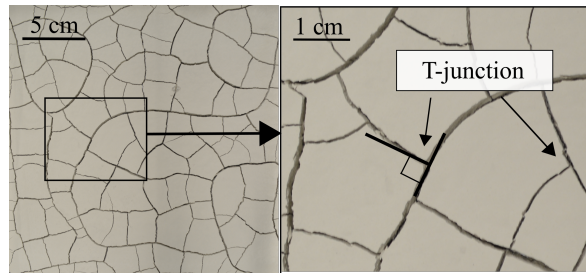


Figure 1.3: Intersection of cracks on a flat substrate. Crack pattern is generated by drying a Bentonite slurry. In this figure many cracks can be seen to intersection at approximately 90°. This happens because cracks tend to bend to in order to release the maximum amount of strain energy.

The physics of the formation of the crack pattern shown in figure 1.3 is scale free. If the same experiment is done at the kilo-meter scale, provided all factors in the system scale with

the crack spacing, the thickness of the crack will increase by the scaling factor. This is not restricted to mud cracks. The scale free nature of the crack pattern would not change even if the pattern was generated over a non flat substrate. As long as the structure of the substrate is scaled accordingly, the crack pattern generated on the substrate will remain the same.

In the next section, examples of crack patterns at the kilometer, meter and micrometer scales are presented. Many of these crack patterns do not form on flat substrates and the driving force behind crack formation are different from poroelastic forces which drive mud cracks. These examples serve to highlight how universal crack patterns are which is the motivation behind studying how crack pattern form on non flat substrates and developing methods to quantify them.

## 1.4 Big to small - crack patterns over various length scales

In nature cracks there are seldom single, isolated cracks. Most fracture processes lead to multiple cracks which interact and form a crack pattern. Simple examples of crack patterns are cracks in mud puddles [52], which were mentioned in the last section or paint cracks [48].

One defining feature of crack patterns is that they form network-like structure where the nodes of the network represent intersections between two or more cracks ([16, 15]). These nodes shall be referred to as crack intersection points. In some cases, the stress within the cracking material is insufficient for crack propagation, this leads to cracks that are either completely disconnected from the crack network, or cracks with only one end terminating at a crack intersection point [42]. Cracks in a crack pattern can be classified based whether or not they are connected to the crack network. Cracks connected to other cracks at both ends will be referred to as **connected cracks** , cracks connected only at one end with the second end free with be called **hanging cracks** and cracks disconnected from the crack network with be called  **unconnected cracks**. Most crack patterns form a base closed network with few hanging and unconnected cracks. The presence of a large number of hanging and unconnected cracks hints that the crack pattern has not matured[42].

Attempts have been made to cast geological fracture patterns as networks and study their network properties ([86, 59]). Here the metric between two crack intersection points becomes irrelevant. The crack pattern is replaced with an equivalent graph, and properties of the graph are measured ([5, 38]).

Not all crack patterns can be cast as a closed network[4]. Three examples of such crack patterns are given in the figure 1.4.

Many crack patterns presented below form on uneven substrates which influence the structure of the crack pattern. The substrate affects the crack pattern by imparting symmetry and topology to it. If the substrate decides what type of crack pattern forms, is it possible that by studying the symmetry and topology of the crack pattern, the structure of the substrate can be predicted? To answer this question, two approaches can be taken- one method involves directly measuring the effect of the substrate on the crack pattern. This requires access to the substrates of all the crack patterns presented below, these substrates can be scaled down

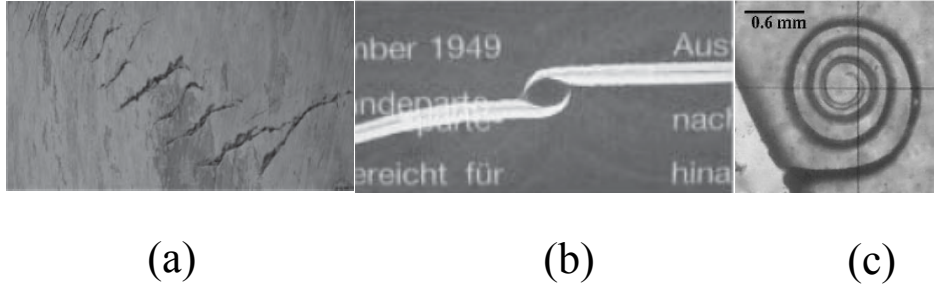(a)                              (b)                              (c)

Figure 1.4: Echelon, En Passant and spiral cracks: (a) Echelon cracks on a rock's surface. The cracks are parallel to each other and roughly the same length. Echelon cracks are a combination of all three modes of fracture ([75], [70]). Figure adapted from [38]. (b) En Passant cracks occur when two cracks, parallel but not lying in the same line, travelling toward each other intersect ([33, 38]). Figure adopted from Fender et al[33]. (c) Spiral cracks occur due to detachment of a film from the surface. Here, mode 1 and 2 fracture dominate. Such spiral crack patterns have been observed in egg albumin as well. Figure adapted from [38]

.

and studied for different conditions. It is a difficult approach since substrates, for example, at the planetary scale are not easily accessible. Such an approach would also not work well with bonded films or soft substrates since they may break if the cracking layer is being removed. This approach also destroys the crack pattern, which is required to understand how the substrate affects the cracking material. A better approach is to study the crack pattern and find ways to relate the topology of the crack pattern to the substrate. For a given substrate, crack pattern can be generated for various layer heights and quantified. By studying how the crack pattern changes with layer height, it would be possible to correctly decipher the effect of the substrate on the crack pattern. This is the approach used in the thesis. This approach requires development of measurement parameters which can quantify a crack pattern. In order to do so, it is essential to look at crack patterns at various length scales to understand how these crack patterns were formed and how can they be classified according to their structure.

Combining ideas from the last section and this section, the reasons to measure crack patterns can be broadly broken down into two points-

- To understand how various fracture driving mechanism influence the formation of cracks and crack patterns.

- To decipher how the substrate affects the symmetry and topology of a crack pattern.

### 1.4.1 Kilometer scale

The examples below show a rich variety of crack patterns at the kilometer scale. An important question to keep in mind while going through these examples is what role do the substrates play in the determination of the crack pattern? Two main examples are discussed -graben patterns in craters and polygonal terrain on Mars. The graben pattern have a circular
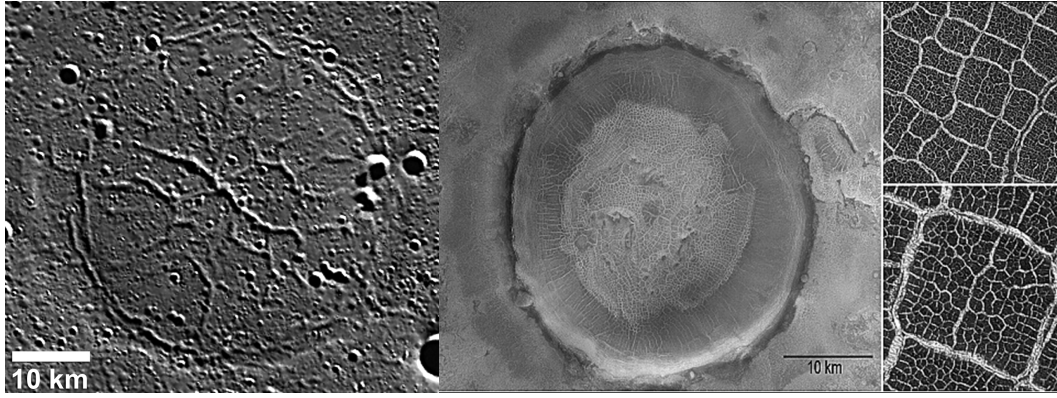
<div align="center">(a)          (b)          (c)</div>

Figure 1.5: (a) Graben pattern on the surface of Mercury. These patterns for due to repeated deposition of lava over an impact crater. Notice the radial symmetry of the graben pattern. Figure adapted from [34]. (b) Polygonal terrain in a 14 km diameter crater. Figure adapted from [31] (c) Here polygonal terrain of two length scales can be observed, the larger length scale polygonal terrain is 70-350 m size, the smaller length scale polygonal terrain is 5-20 m in size Figure adopted from [31]

.

symmetry, which reflect the symmetry of the substrate. The polygonal terrain show crack patterns that form due to thermal contraction of a layer above the substrate.

Cracks have been observed on the surfaces of all the inner celestial bodies- Mercury[14], Venus[8],the Moon[32] and Mars[63]. They have also been seen on the surface of Jupiter's moon Europa ([44],[39]). This suggests that cracks are ubiquitous to moons and planets. The surface of a moon or a planet is hardly constant, geological processes, meteor impacts and gravitational forces of others constantly introduce stresses on a celestial body's surface ([89?, 21? ]). These stresses can generate cracks that range in length from hundreds of kilometres to hundreds of meters .

On Mercury, graben patterns have been observed in ghost craters (buried craters) ([43],[14]). Grabens are depressions created in a surface due to slip. Grabens and graben networks have been observed on Venus[53], the Moon[60], Earth and many other planetary bodies ([65],[76]). Ghost craters ([7],[21]) form due to filling and cooling of lava. These craters typically range in size between 20 km to 60 km [14]. Apart from graben patterns, craters contain wrinkle ridges [74], and graben that extend radially outward from the crater[34]. Unsurprisingly, these craters lie in regions of high volcanic activity. Freed and Blair [14, 34] showed in a set of papers that three mechanisms could lead to the formation of graben patterns: thermal contraction, uplift of the basin floor and subsidence due to cooled lava within the crater. They concluded that the repeated filling and cooling of craters, essentially thermal contraction, lead to the graben patterns observed in figure 1.5 (a).

Figure 1.5 (b) shows polygonal terrain on the surface of Mars. El maary et al. ([30],[31]) suggest that the larger thicker cracks could have formed due to dessication while the smaller
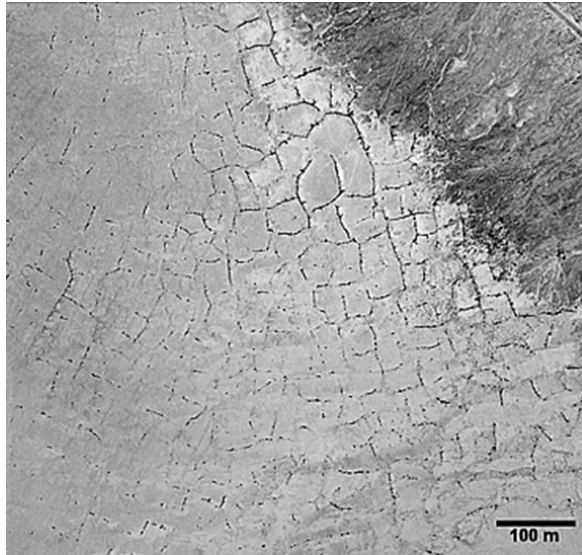
Figure 1.6: Cracks due to dessication. Coyote lake, Califonia, US. The crack spacing varies from 30 to 75 cm in size. Figure adapted from [31]

cracks within could be due to thermal stresses. Dessication cracks are driven by poroelasticity [26] and on Earth, dessication cracks have been observed in dried lakes. Another typical example of dessication cracks are mud cracks, which can be commonly observed in dried puddles ([52],[41]). Thermal contraction cracks form because, changes in temperature can lead to expansion and contraction in the material [54]. Large scale changes or cyclic changes in temperature over long term can cause enough stresses in the material to build up, which can lead to fracture. An example of thermal contraction cracks on Earth is the cracking of lake ice. As the temperature drops during the evenings, lake ice cracks due contraction. During morning and mid day, ice melts and fills the cracks in between. Thermal contraction cracks are most commonly found in the polar regions of Earth[49]. In both cases, the contraction of the material leads to cracking, hence dessication cracks and cracks due to thermal stresses are generally known as contraction cracks.

Both dessication and thermal contraction cracks tend to form similar crack patterns. The difference lies in the length scale of the crack pattern. For example, in figure 1.6 shows a crack network formed due to dessication of a dried lake on Earth. Crack spacing of ranging from 30 m to 75 m have been observed [31].

The graben patterns found atop craters have radial symmetry and the polygonal terrain has cracks that form square like cracked regions. The crack are almost perpendicular to each other. For the graben patterns, the symmetry of the substrate is obvious, while this is not true for the polygonal terrain. These are two types of crack patterns that form due to two different mechanism. Below crack patterns at the centi-meter scale are presented.

## 1.4.2 Centimeter scale

To find crack patterns, one hardly needs to go as far as Mercury or Mars. From paint cracks to craquelure, many examples of crack patterns exist from the centimetre to the meter

scale. The focus here on crack in paintings, where environmental effects on the substrate determines if a painting cracks or not, and memory effects in pastes where periodic driving forces determine the structure of the crack patterns.

Craquelure is defined as a dense crack pattern. It is commonly found in paintings and in glaze. The study of craquelure has received much attention because of its applications to conservation of paintings[2, 19, 20, 9].Figure 1.7 (a) shows an image of a painting where the right part of the painting, glued to a wooden piece whereas the left side of the canvas is left hanging ([10],[9]). Fixing the canvas prevents cracks from occurring.

Karpowickz [46] measured the strain in a gel under uniaxial stress, and postulated that cracks in a painting could be due to viscoelastic recovery after drying. He also showed how exposing brittle thin films to high humidity causes contraction of the film leading to a "typical craquelure pattern" [47].

Berger and Russell [11] measured the stress change in a canvas due to varying environmental conditions. In figure 1.7 (b), the top plot shows the changing temperature and relative humidity, and the bottom plot shows the change in stress due to large scale changes in humidity. Berger and Russell suggest that in order to conserve an oil painting and prevent cracks, a canvas must be stretched so that it remains stiff. The tension in the canvas can be compromised due the change in the environmental conditions, mainly humidity. Cyclic changes in humidity or temperature can either overstretch or contract the canvas. They suggest that one of the best ways to prevent cracks is to attach a rigid support to the canvas in order to prevent loss of tension.

Nakahara et al.[68, 62] studied the memory effects in pastes. They found that pastes had "remembered" the direction of vibration, and when dried and formed cracks in a direction opposite to the direction vibration. In other cases, pastes cracked along the direction of flow. Figure 1.8 shows a dried magnesium carbonate hydroxide paste that has cracked in a direction perpendicular to vibration direction, and parallel to the direction of flow. They conducted experiments with colloidal particles and showed that in a paste, decreasing particle size leads to a stronger memory effect due to vibration.

The driving force of fracture for the two systems presented here are the same. In both cases, drying causes stress in the cracking materials and crack patterns form. Unique to each system is an external factor that affects the cracking process. In the paint cracks, the structure of the substrate gets altered due to change in humidity. By studying the crack pattern is it possible to determine how the substrate changes? In order to understand this, crack patterns must be generated using substrates of varying stiffness in order to determine conclusively if a stiffer substrate will necessarily prevent paint cracks. Cracks in pastes with memory are a unique system. There is no variation in the substrate however a driving force alter the cracking medium and induces internal stresses within the material. Quantifying the crack pattern would allow a comparison between the crack pattern and the driving force that generated the crack pattern. This in turn could assist in predicting what type of crack pattern will be generated based on the magnitude and direction of shaking. The next set of examples will deal with micro-scale cracking.
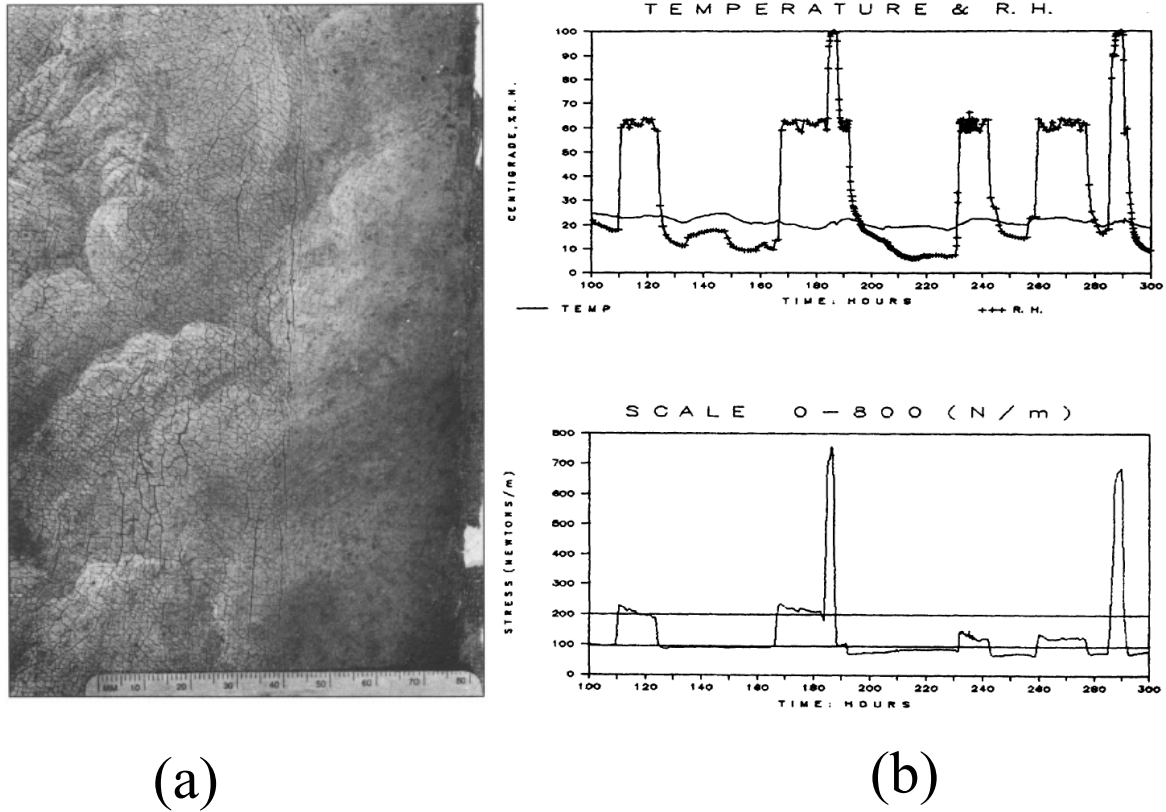
$$(a) \qquad\qquad\qquad (b)$$

Figure 1.7: Role of substrate in formation of craquelure: Experiments to study the effect of changing environmental conditions on the canvas .(a) On the left side of the painting, crack patterns are observed. On the right side of the painting, no crack are observed due to the present of a wooden support. Figure adapted from [10] . (b) Top panel shows the changing environmental conditions with respect to time to which the canvas is exposed. The line with pluses represents the change in relative humidity. The solid line represents the change in temperature which is generally allowed to vary between 22°-25° C. (b) The bottom panel represents the change in stress due to the change in environmental conditions. Notice that the maxima in stress occur at the same time points as the maxima of the relative humidity [11]. Figure adopted from [11]

.

### 1.4.3 Microscale and below

Three types of crack patterns are presented here - cracks in a gallium nitride film, cracks in blood droplets and finally cracks in an Au/PDMS bilayer. The cracks in the gallium nitrite films and the Au/PDMS bilayer occur due to misfit strains that occur between the deposited material and the substrate. These misfit strains occur due to difference in elasticity and are common in epitaxial growth processes as well since, in process of deposition or growth of the material, any defects cause strains to build up in the the crystal structure and this in turn causes fractures.

Fracture patterns at the micron scale are shown in figure 1.9. In figure 1.9 (a), a gallium nitrite film is deposited on a silicon substrate [78]. The film is approximately $5\mu$m in thickness. Thin films of such size are routinely used in industry, especially in building circuits for micro
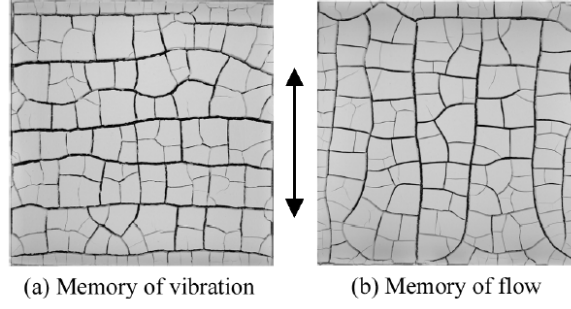
| (a) Memory of vibration | (b) Memory of flow |

Figure 1.8: Memory effects in pastes: (a) memory of vibration- A water poor paste of magnesium carbonate hydroxide (volume fraction $\rho = 12.5\%$) is shaken at an amplitude $a = 15$mm and frequency $f = 2$Hz [68] . The arrow shows the direction of shaking. Primary cracks are perpendicular to the direction of vibration; secondary cracks are parallel to the direction of vibration [68]. (b) A water rich paste of magnesium carbonate hydroxide (volume fraction $\rho = 6.7\%$) is shaken in the direction of the arrow. Here, the primary cracks are perpendicular to the direction of shaking [68]. What do the crack patterns tell us about the stress distribution inside the medium?

mechanical electronics machines (MEMS) [69, 3]. In figure 1.9 (a) the thicker cracks are the primary cracks, and thinner cracks are the secondary cracks. Cracking in microfilms at such length scales can be disastrous. Numerous attempts have been made to better understand how cracking occurs in thin films [12, 91, 88, 90] some of these ideas are discussed in the next section.

Figure 1.9 (b) shows a dried and cracked droplet of blood. Blood is a colloid that consists of plasma and celluar matter which include red blood cells, white blood cells and platelets. Sobac and Brutin [80] showed how a drying droplet of blood have two regimes, and how in the second regime, which is defined primarily by diffusion, a radial crack pattern is formed. In a follow up paper in 2014 [81], they show how as a gelation front reaches the center, cracks follow. The drying mechanism is similar to that of the coffee ring effect. They also showed that the crack spacing, is roughly proportional to the thickness of the drop of blood. As a droplet dries fully, in the center of the dried blood droplet, an isotropic crack pattern forms. They observed delamination along the edges of the droplet as well.

Figure 1.9 (c) shows a pattern created using controlled cracking in gold, PDMS bilayer. Here, micro-groves were built into the PDMS substrate then a gold film was deposited and cracked. By controlling the frequency of notches at will and the spacing between the notches, it is possible to create crack patterns [28, 50, 51].

Kim et al.[51] describe methods to use controlled fracture to create nano and micro-structures. When PDMS is strained then exposed to plasma and the strain is released, cracks form [72, 18, 67]. This is because the surface of the PDMS oxidizes which creates a thin stiff layer. The elastic mismatch between the stiff surface and interior of the PDMS causes cracks to occurs [58]. By precisely controlling the stress it is possible to control crack spacing and by controlling the oxidation time of PDMS surface, the crack depth can be controlled. In this paper, Kim et al. refer to various other methods of nano fabrication and suggest potential
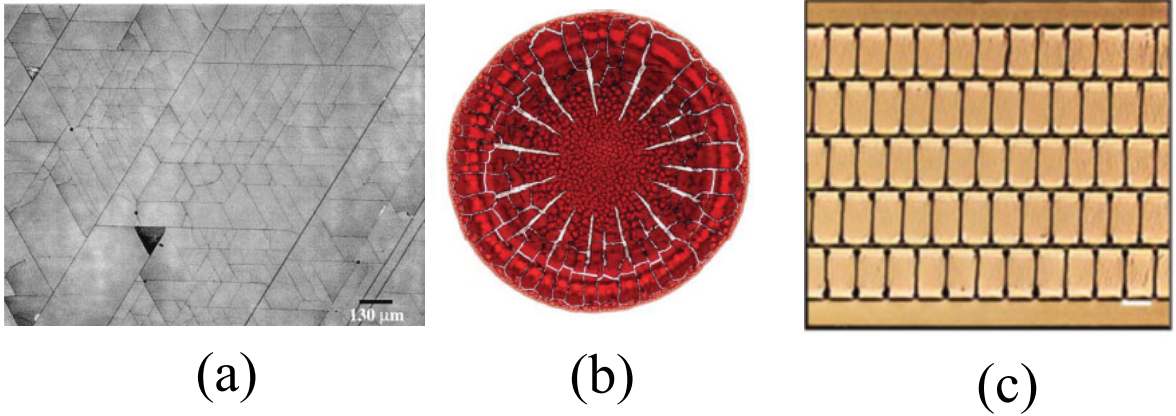
application to biological systems [51].



(a)   (b)   (c)

Figure 1.9: Crack patterns at the mirco-scale: (a) $5\mu m$ thick gallium nitrite film. Cracks appear along the cleavage planes. Cracks tend to intersect at $60°$. Darker cracks are the primary cracks, the second generation of cracks are fainter and are in general parallel to each other [78]. Figure adapted from [78] . (b) Crack pattern of a dried blood droplet. Droplet diameter is 8.6 mm, at room temperature of $22°C$ and relative humidity of $RH = 42\%$. Initially as the droplet dries, it gels[80] . The region of geletion shrinks and during this shrinkage, crack form along the edges and propagate inwards[81]. Inside the droplet, a finer crack pattern can be seen [80]. Figure adapted from [80]. (c) Crack pattern generated by on a Au/PDMS bi-layer. Gold is deposited onto a layer of PDMS under strain. The PDMS layer contains notches. A detailed method of fabrication is presented in [50]. Figure adapted from [80].

The three crack patterns presented conclude the examples of crack patterns at different length scales. From the micro scale to the macro scale, in all the examples, the substrates play a major role in determining how crack patterns form and propagate. In two of the cases - memory pastes and blood cracks- although there is no substrate, external influences alter how the crack pattern can evolve. In the case of blood cracks, the crack pattern can change based on the temperature, humidity or pH of the environment. This may happen due to change in drying rate or change in the structure of the cells within in the blood droplet.

Some references have been made to quantifying crack patterns. In the next section, previous attempts to quantify crack patterns will be discussed.

## 1.5   Quantification of crack patterns

There are numerous approaches that have been attempted quantify a crack pattern. There are two approaches used- one approaches involves generating either a purely artificial network or an artificial network based on a real network and developing methods to analyse them. The second approach involves using real crack networks to define measures for a crack pattern.

Andresen et al. study fracture outcrops by representing them as an artificial networks and measuring network parameters [5]. Such an approach has also been used by Valentini et al. to analyse rock fractures networks [86]. Fracture outcrops are lines of cracks that are part

of exposed geological structures. Examples of these geological structures are large boulders or sedimentary rocks. Andresen et al. took various fracture outcrops and generated networks by labelling cracks as nodes. The intersection between the cracks are labeled as edges which connect the nodes. They measured the degree distribution, the clustering coefficient, the efficiency of the network and the characteristic path length. The degree $k$ of a node is the total number of neighboring nodes. If the degree distribution $P(k)$ follows a power law, then the network is considered scale free. The clustering coefficient measures the local connectivity of the network. The clustering coefficient has a value between 0 and 1 where values close to 1 represents a condition where two neighbours of a single node share an edge of the network. The clustering coefficient is a means to measure the local connectivity of the network. Such local measures would be useful pattern seen in polygonal terrain where local structure exists with a larger crack pattern. The efficiency $E$ of the network is a measure of how well different parts of the networks are connected to each other, and this is a global measure of the pattern. $E$ is proportional to the inverse of the distance between two nodes in the network. It falls between 0 and 1 except for the case where $E = \infty$. This too can be generally applied to many crack patterns. For example, comparing the blood cracks and the memory paste cracks, $E$ may be smaller for the blood cracks since very few radial cracks are connected to each other ( white regions in the figure 1.9 (b)) whereas in figure 1.8 a path between any two vertices of the crack pattern can be found by travelling along the crack pattern. The last parameter they mention is the characterstic path length L which represents the average distance between any two nodes in the network. The average path length is large for fracture networks that have a small $E$ value since the network is not well connected. While the methods discussed by Andresen et al. work well at characterizing networks, they may not be easily applicable to real crack patterns. Firstly, they require a crack pattern with a large number of cracks, in order to plot any meaningful distributions of $P(k)$. With systems like that of Nakahara et al., it would be difficult to get the adequate statistics. Secondly, the measures contain very little information about the substrate of the crack pattern. This is required initially to understand how a crack patterns evolve.

Hafver et al. [42] took a different approach where rather than using existing crack patterns as models they generated artificial crack patterns and made measurements on them. Their cracks were straight lines whose position was chosen according to a probability which was weighted by a distance map of the pattern, and whose the orientation was chosen randomly. Once a line was placed, it was extended in both directions until it either met another line or hit a boundary. Hafver et al. had two control parameters for their patterns: $\gamma$ which controls the homogeneity of the pattern and $\omega$ which controls the topology of the pattern. $\gamma$ could take the values $-2 \leq \gamma \leq 2$ whereas $0 \leq \omega \leq 1$. For a value of $\omega = 0$ lines form a tree like structure and for $\omega = 1$ the lines generate polygonal structures. A pattern with $\gamma = 2$ and $\omega = 0$ is an isotropic pattern where most lines have one free end. The free end refers to one end of the line not intersecting with the boundary, or with any other line. On the other extreme where $\gamma = -2$ and $\omega = 0$ most of the lines in the pattern lie at the boundary; no lines are present in the center of the image. Increasing the value of $\omega$ to 1 with $\gamma = 2$, generates a pattern

where the majority of lines lie along the diagonal to the square boundary or perpendicular to the diagonal. Values of $\gamma = 2$ and $\omega = 1$ generate an isotropic pattern where there are no free ends for any line, all lines are connected on both ends to either another line or to the boundary. Using $\omega$, Hafver et al. define an order parameter $R = (1-\omega)/(1+\omega)$ which is the ratio of the free ends to the number of intersections of lines. Since replacing the lines with cracks does not affect the definition of the parameter, they propose that $\omega$ can be used as a measure of crack patterns as well. Another order parameter they define is the measured value of $\gamma$. They measure $\gamma$ based on the temporal hierarchy of the pattern. Both the parameters are applied to crack patterns in gelatin confined to a Hele-Shaw cell, ice fractures on Mars and weathering cracks on the surface roads. Similar to the parameters of Anderesen et al. such a parameter does not characterise the symmetry of the pattern. A radial crack pattern can either have cracks extending radially outwards or cracks that lie parallel to boundary, the two parameters can be tuned such that in both those cases the values of $\omega$ and $\gamma$ are the same. Furthermore, the parameter $R$ is then dependent on the number of free ends in the crack pattern, hence if a crack pattern were allowed to evolve for long enough, $R$ will drastically change. This is a benefit for time lapse imaging of a crack pattern but if the crack pattern has an overall directionality, which can be imposed by the substrate, then $R$ would not be able to capture the influence of the substrate.

Bohn et al. [16] took an experimental approach to defining an order parameter. They studied the temporal and hierarchical evolution of glaze in ceramics by analysing a crack patterns generated by drying starch slurries on a rectangular polymethylmethacrylate (PMMA) substrate. They show that orientation of the first fracture is non-deterministic for low layer heights and with increasing layer height, the orientation and structure of the first crack becomes deterministic. They quantify this using two order parameters, these are $\delta = |d_1 + d_2|/\sqrt{A}$ and $\Delta = \sqrt{d_1^2 + d_2^2}/\sqrt{A}$ where $d_1$ is the distance along the rectangle, between one end of the crack and the center of the left edge of the rectangle, $d_2$ is the same, however for the right edge. The definitions of these are shown in figure 1.10. Both parameters $\delta$ and $\Delta$ yield 0 if a crack divides rectangular region into two equal halves. For a curved crack $\delta > 0$ and $\Delta > 0$. These parameters approach close to zero with increasing layer heights. The large spread in values of $\delta$ and $\Delta$ at low layer heights is what signifies the disorder whereas at large layer heights the standard deviation of both order parameters is small. Both these order parameters can be written according to the symmetry of the region bounding the crack pattern, however, since they pertain to only a single crack, they cannot be used to analyse current experiments because the information about the first crack is lost in a mature crack pattern.

The various methods to quantify crack patterns that have been presented above have a certain realm of applicability. The $\delta$ and $\Delta$ parameters serve to quantify a crack in a rectangular domain, the network parameter presented by Andersen et al. are suited for crack patterns with large number of intersections, the parameters $R$ and $\gamma$ are best suited to study an evolving crack pattern. None of these parameters contain any information about the orientation or the symmetry of the substrate, hence it is difficult to apply them to the
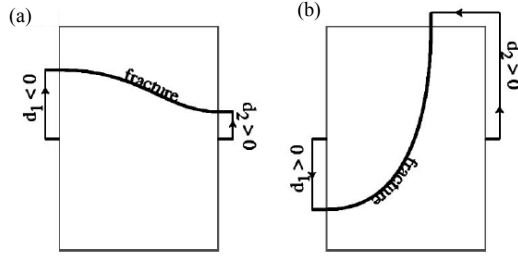
Figure 1.10: Definitions of $d_1$ and $d_2$. Figure reproduced from [16]

current problem.

## 1.6    Scope of the thesis

The thesis is divided into 6 chapters. This section concludes the end of chapter 1 which aims to present introductory ideas about the research problem. The second chapter contains the experimental details and information about the image processing methods used to prepare the images for analysis. Two types of uneven substrates are used in generating cracks patterns- sinusoidal plates and radially sinusoidal plates, details about the number of plates and variation in amplitudes and wavelengths of the plates are discussed. The procedure of preparation of the slurry is also discussed. Some preliminary raw images of crack patterns are shown. Once images of crack patterns have been acquired, they must be processed, such that metrics and measure can be applied. The image processing of crack patterns is also discussed in chapter 2 - Materials and methods.

Chapter 3 - Analysis of crack patterns - defines new measures that are used to classify crack patterns. These measures employ the symmetry and orientation of the substrate to quantify crack patterns generated in chapter 2. The algorithm of each measure is described in this chapter and a few crack patterns are analysed as examples. Along with the measurement parameters, the method to measure the crack spacing is also presented.

In chapter 4 - Results, the data for different measurement parameters are presented. The chapter begins with the data for time evolution of a measurement parameter. This is done to set a minimum time of drying for the experiments, it also shows that the measurements are made on crack patterns that do not evolve further i.e that a crack pattern is mature. The measurement parameters are plotted with respect to increasing dimensionless layer height. The crack spacing is also plotted with the layer height $H$ in centimeters.

Chapter 5 - Discussion presents the analysis of the data from chapter 4. The effectiveness of quantification is discussed. The order parameters are compared to each other and their extremes are discussed. The experimental results are compared with finite element model (FEM) simulations carried out by Lucas Goehring.

The final chapter - Future directions - presents a host of new ideas that can be explored, it primarily discusses the micro scale and geological equivalents of the current experimental setup.

# Chapter 2

# Materials and methods

In order to study crack patterns over uneven substrates, clay slurries are dried over sinusoidal substrates and radially sinusoidal substrates. This chapter presents the experimental details and preliminary stages image analysis of these crack patterns. It aims to describe how the experiments were carried out, some preliminary observations and image processing procedures which convert the raw images into binary and skeleton images.

The first section in the chapter describes the experimental setup and the procedure followed to generate crack patterns. The experimental setup consists of five sinusoidal plates and two radially sinusoidal plates. These two types of plates represent two different but simple symmetries. The preparation of the bentonite slurry is also described in this section.

As mentioned in the chapter 1, the control parameters for the experiment are the amplitude $A$, the wavelength $\lambda$ for the sine wave plate and the layer height of the clay is $H$. The amplitude and wavelength are fixed values for each plate. The choice of layer heights for each plate and their values are discussed in section 2.1.1. Preliminary observations about the types of crack patterns are also given there.

Section 2.2 provides methods required to prepare the crack pattern for analysis. The crack patterns generated due to dried bentonite slurries were imaged. These images are converted to binary images, and then skeleton images for further analysis. The procedure for this conversion is described. Once the skeleton images are generated and spurs are removed, the points where two or more cracks intersect are found. Using these points, a list of all neighbouring vertices for each vertex are identified and stored.

## 2.1 Experimental setup and procedure

In order to generate crack patterns, bentonite slurries were dried over sinusoidal and radially sinusoidal substrates. All substrates used in the experiment were 20 cm by 20 cm. Plates 1-5 were made using computer numerical control (CNC) milling with a resolution of 400 $\mu$m for plates 1, 4 and 5, and a resolution of 200 $\mu$m for plates 2 and 3. These substrates were made of acrylic since it is perfectly stiff compared to the dried mud slurries. In these substrates, the height profile along the height, which shall be referred to as the $z$ direction is given by $z\,(x,y) = A\sin\,(2\pi x/\lambda)$. A list of amplitude A, and wavelengths $\lambda$ is presented in table 2.1.
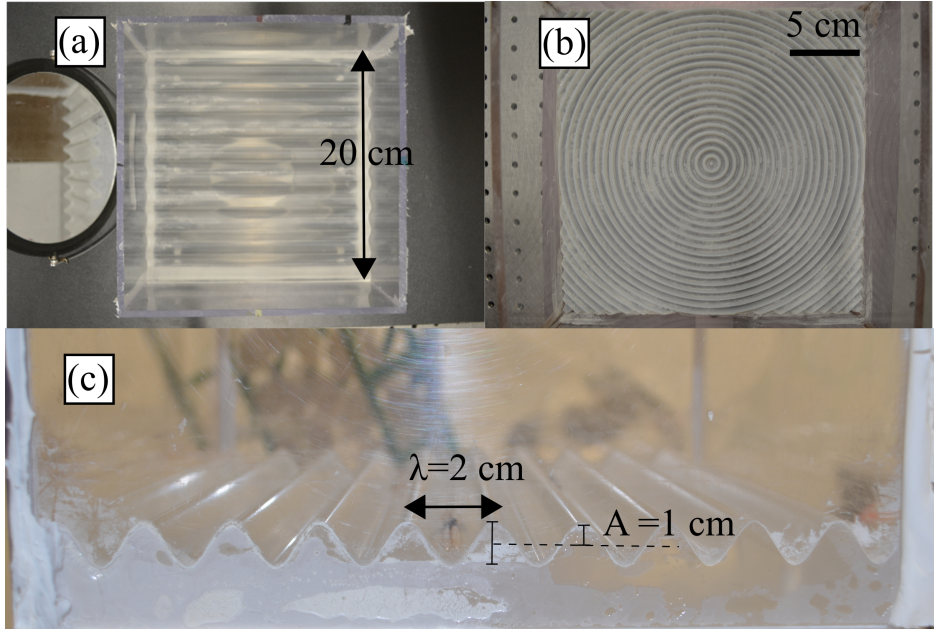
Figure 2.1: Substrate images . (a) is a top down view of plate 1 . (b) is a top down view of radial plate 1. (c) is a side view of plate 1.

The radially sinusoidal plates 1 and 2 were 3d-printed by the company 4D concepts since it was not possible to use CNC milling to create the radial structure of the plates. The height profile of the radial plates is given by $z\left(r,\theta\right) = A\sin\left(2\pi r/\lambda\right)$. The radially sinusoidal plates were made using acrylic photo-polymer. Figure 2.1 contains examples of a sinusoidal and a radially sinusoidal plate. Figure 2.1 (a) shows a top down view of the sinusoidal plate 1 while figure 2.1 (b) shows radial plate 1 and figure 2.1 (c) shows the side view of plate 1. A flat plate made from acrylic was used as the control plate for all the experiments. This plate has the same dimensions as the rest of the plates.

In order to prepare bentonite slurries, bentonite (Acros Organics) was mixed with Millipore deionized water with a weight ratio of 1:2 i.e twice as much clay compared to the weight of the water was added. A commercial scale was used to weight the bentonite and the distilled water. In all cases, two separate containers were used to prepare the slurry, bentonite powder was weighed and stored in the first container; the distilled water was weighed and stored in the second container. The bentonite powder was carefully added to the second container. It was ensured that the bentonite powder landed in the center of the second container to prevent power sticking to the edges of the container. The second container was set to rest until all the bentonite was wet. After this, the mixture was stirred vigorously for 5 minutes. After stirring, the resulting slurry was immediately poured on the substrate and left to dry. Different proportions of the bentonite and water were tested. Higher ratios of bentonite to water were prone to the memory effect studied by Nakahara et al. [68], lower ratios of bentonite contained too much water which would fill the container but was too thin, it contained too much excess water [68].

Crack patterns were generated with a range of bentonite weights, ranging between 60 to 300 grams (for all plates, refer to table 2.2) in 10 gram increments. The lowest bentonite

weight was chosen such that the slurry barely covered the top of the peaks and when these slurries had dried, it left a thin layer of dried bentonite on the peaks. Such thin layers contained either fine cracks or no cracks at all.

The bentonite weights were translated to layer heights by calculating the density of the bentonite sediment. In order to calculate the density, bentonite slurries were prepared and allowed to settle in 5 graduated cylinders and in flat plate. The flat plate data was generated for masses of 80, 100, 200 grams of bentonite. Both were imaged for 6 hours after which the layer height of the settled bentonite layer was measured. It was observed that after 150 minutes, the layer heights remained unchanged in both geometries. In case of the flat plate, the dried layer heights were also measured after the slurries dried. The graduated cylinders did not dry for several days hence the dry layer height could not be measured. The results for the wet layer height of the cylinders and the flat plate were averaged and the density was found to be $0.49 \pm 0.12$ g/cm$^3$. This density was then used to convert bentonite weights to layer heights.

The substrates and the slurries were placed on a levelled surface to dry. For plates 1-5, the drying was accelerated by two halogen lamps placed above the clay surface. While the room was always kept closed during the experiments, there was no humidity or temperature control. The halogen lamps generally maintained the temperature near the surface of the drying slurry at approximately 50°C, therefore the drying times were low. For example, a slurry containing 60 g of bentonite would dry and form a crack pattern in approximately 2 hours. As the bentonite weights were increased the drying times also increased. In general, a minimum of 4-6 hours of drying, based on the bentonite weight, was allowed in all experiments. For the radially sinusoidal plates, the halogen lamps could not be used since the acrylic photo-polymer melts if the temperature is above 40°C. Hence, the slurries were dried using a small heater which maintained the room temperature at 30°C. The slurries on the radial plate, including the low layer height slurries were dried overnight to ensure that the crack pattern was mature enough. In case of large layer heights, usually with slurries that contained more than 200 g of bentonite, the slurry was left to dry for 36 hours.

As the slurries dried, they were imaged using an overhead camera. The cameras used were digital SLR cameras (Nikon D5100 and D5200). Images were taken after every minute for plates 1-5 and the flat plate, whereas images were taken every 5 minutes for the radially sinusoidal plates since the drying was slower.

### 2.1.1 Preliminary observations

The range of bentonite masses and layer heights for each plate is given in table 2.2. The layer height $H$ is in centimeters, and $h = H/\lambda$ is the dimensionless layer height. For plates 1, 4, 1r and 2r the lower mass ranges were not explored since it was not possible to spread the bentonite slurry evenly.

As the slurry dries, the crack pattern form sequentially. The first set of cracks propagate until they hit the boundary, after this they start opening further. These cracks are referred to as primary cracks. At intermediate layer heights, primary cracks lie parallel to the peaks

| Plate | $A$ (cm) | $\lambda$ (cm) | $a = A\backslash\lambda$ |
|---|---|---|---|
| Wave plate | | | |
| 1 | 0.5 | 2 | 0.25 |
| 2 | 0.25 | 1 | 0.25 |
| 3 | 0.25 | 0.5 | 0.5 |
| 4 | 0.5 | 1 | 0.5 |
| 5 | 0.25 | 2 | 0.125 |
| Radial wave plate | | | |
| 1r | 0.25 | 0.5 | 0.5 |
| 2r | 0.25 | 1 | 0.25 |

Table 2.1: List of amplitudes and wavelengths of the various plates. 1r and 2r are also called radial plates 1 and 2.

| Plate | Mass range (g) | $H$ (cm) | $h = H/\lambda$ |
|---|---|---|---|
| Wave plate | | | |
| 1 | 90-300 | 0.46-1.53 | 0.23-0.76 |
| 2 | 60-300 | 0.30-1.53 | 0.30-1.53 |
| 3 | 60-300 | 0.30-1.53 | 0.60- 3.0 |
| 4 | 100-300 | 0.51-1.53 | 0.51-1.53 |
| 5 | 80-300 | 0.40-1.53 | 0.20-3.0 |
| Radial wave plate | | | |
| 1r | 80-300 | 0.40-1.53 | 0.20-3.0 |
| 2r | 80-300 | 0.40-1.53 | 0.20-3.0 |

Table 2.2: List of bentonite masses, layer heights and dimensionless layer heights.

of the substrate. For low layer heights, most of the primary cracks were curved, whereas for large layer heights, the primary cracks did not show any direction preference.

The secondary cracks occurred generally after the primary cracks had stopped propagating. Most secondary cracks tend to be smaller in length and thickness than primary cracks. They started to grow either in a region between two primary cracks, or stemmed from the edge of a single primary crack. For intermediate layer heights, the secondary cracks were perpendicular to the primary cracks, which was true for low layer heights as well. However, for low layer heights many of the secondary cracks were curved. They start growing and terminate at a primary crack. For large layer heights, many secondary cracks that originate from primary cracks tend to be unconnected on one end.

In order to analyse the crack pattern images, it is necessary to quantify the connectivity of the crack pattern. This involves identifying the points where two cracks intersect (which are known as crack intersection points) and calculating a connectivity matrix. The next section deals with methods required to prepare the crack pattern for such analysis.
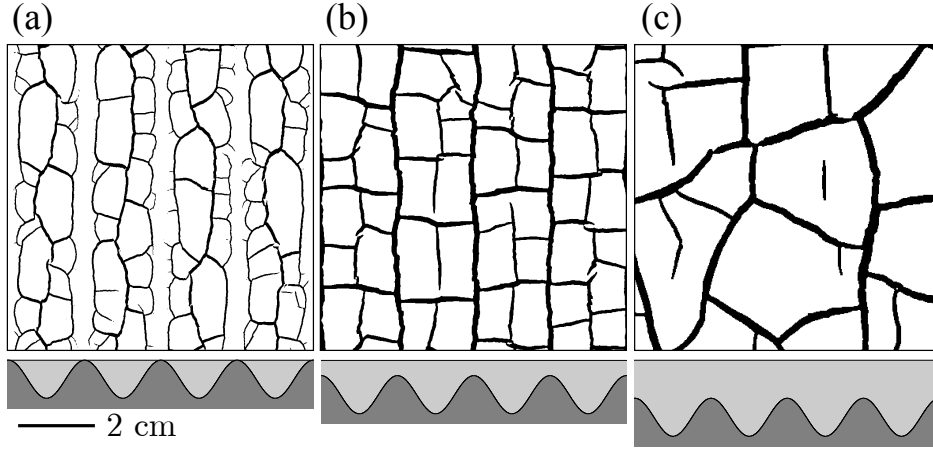
Figure 2.2: Examples of (a) wavy (b) ladder-like and (c) isotropic crack patterns, the substrates and layer heights are shown below.

## 2.2 Image processing

The images obtained in the last section are processed to obtain information about the crack pattern image. The images are cropped and processed to acquire a contrast adjusted grayscale image. After this, MATLAB is used to further clean, binarize and skeletonize.

Once skeleton images of the crack pattern are available, the vertices of the skeleton are identified. The connections between the identified vertices are constructed and connections are presented in form of a connectivity matrix. Using the skeleton image of the crack pattern, the vertex location, and the connectivity matrix, tools are developed to quantify crack patterns.

The amount of pre-processing required differs from image to image. Certain images require minimal or no pre-processing. In the case of unconnected cracks and the radial unconnected cracks, for example, no pre-processing stage is required in order to analyse images. In other cases, extra care must be taken while pre-processing the images to ensure that relevant detail is captured. Examples of this (large mud cracks) will be discussed in this chapter.

The methodology referred to in figure 2.3 is applied primarily to mud cracks. For other crack patterns, this methodology may change based on the type of raw image of the crack pattern. This is especially true for images similar to figure 2.7 (a). This is because the contrast between the cracks and the background will vary with different images. In the current experiments, the lighting conditions allowed for a good contrast for larger cracks. Fine cracks, in general are difficult to capture. Since the focus here is on defining measures on a connected crack pattern, finer cracks are removed.

### 2.2.1 Pre-processing of images

The goal of the pre-processing stage is to ensure that all the images are of the same type i.e binary and skeleton images. This step is necessary for batch processing of images. In all cases, regardless of the initial image type, the final image after pre-processing is a grayscale image of the crack pattern where cracks are represented by the black region and the un-cracked
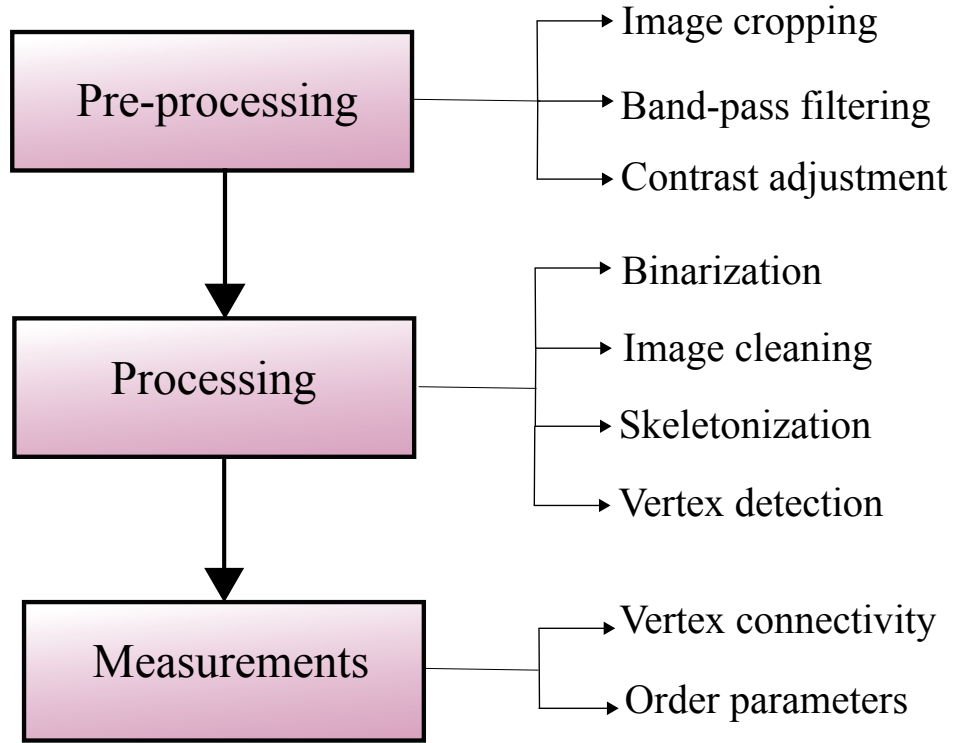
Figure 2.3: The steps of image processing. In the pre processing phase, three essential functions are carried out: cropping, band-pass filtering and contrast adjustment. Processing the image involves binarization and cleaning the binary image, followed by skeletonization of the image and vertex detection. In order to make measurements, the vertex connectivity must be acquired, using which measurement parameters are calculated.
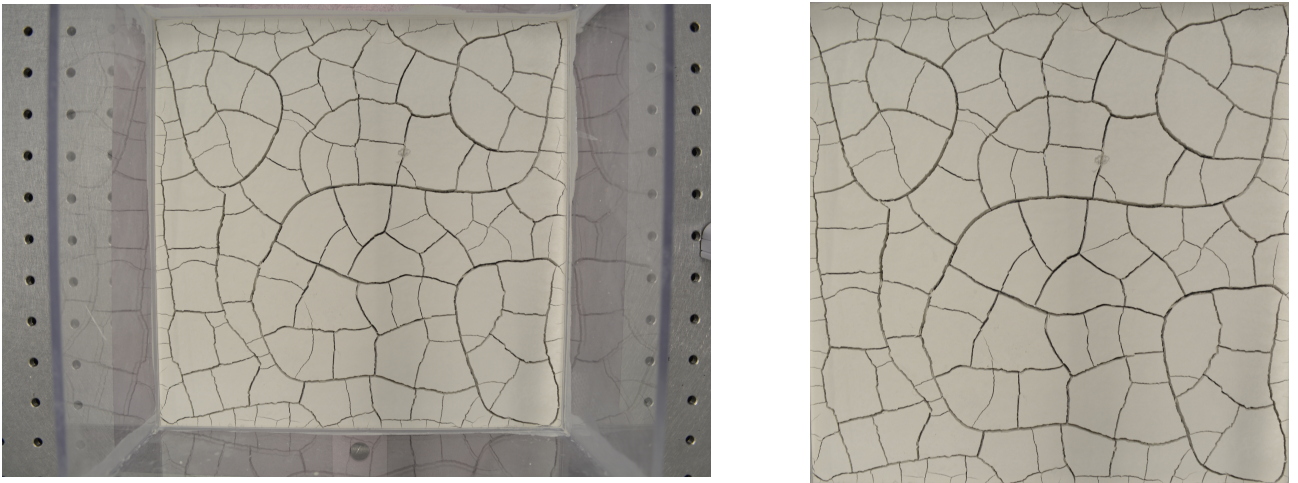


Figure 2.4: Raw and cropped images of a crack pattern. (a) Image of a crack pattern over a flat substrate. (b) cropped version of (a). Edges of the image are removed to focus only on the crack pattern. The images are converted to 8 bit and further processed.

regions are represented by the white region.

The first step in pre-processing the image involves correcting and cropping the image.

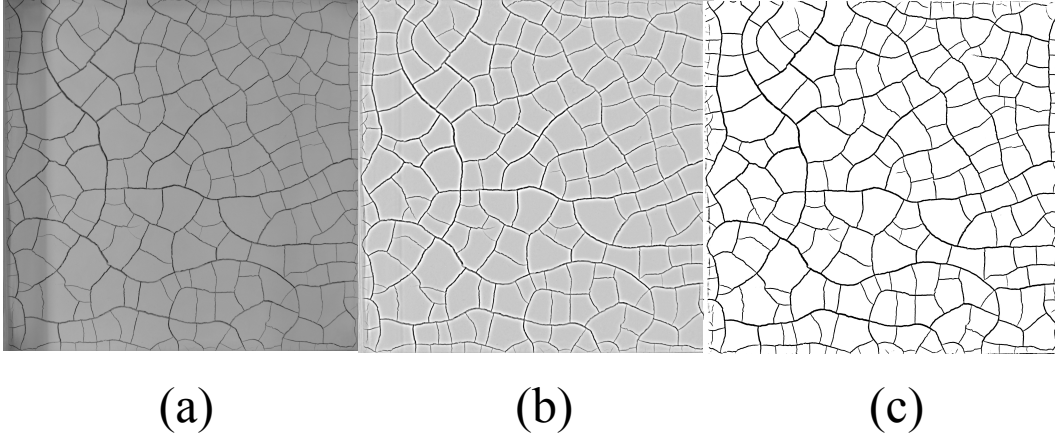<div align="center">(a)          (b)          (c)</div>

Figure 2.5: An example of uneven lighting in a crack pattern image. (a) Image of a crack pattern with uneven lighting. The dark band on the left side of (a) is the shadow due to the wall of the container. (b) shows band-pass filtered image of (a). No noticeable shadow is observed. (c)shows a contrast adjustment image of (b). No effect due to the shadow is observed in the final grayscale image.

Image correction involves rotation. In each experiment, the position of the substrate with respect to the camera can change due to the placement of the substrate. This can be easily corrected by rotating the image. The rotation corrections are small (maximum adjustments - 1.0°), therefore they were carried out using imageJ.

Images such as the one shown in figure 2.4 (a) do not need any kind of rotation correction. Figure 2.4 (a) is cropped along the edges, the cropped image is shown in figure 2.4 (b).

The second step in pre-processing the image involves putting the image through a band-pass filter. The images are first converted to 8 bit, then the band-pass filter is applied. The details of the band-pass filtering process are discussed in [45]. The band-pass filter in imageJ allows for structures within a range to be filtered, an upper size of 40 pixels and lower size of 3 pixels was used for all images. The documentation for the ImageJ band-pass filter can be found in [1]. An example of uneven lighting is shown in figure ?? (a). The band-pass filter also ensures that the cracks in the image are highlighted well enough.

Once the band-pass filter has been applied and the resulting image is acquired, the last step is contrast adjustment. The band-pass filtered image is a grayscale image, hence it has a maximum and a minimum value, figure 2.6 (b) shows an example of a contrast adjusted grayscale image.

### 2.2.2 Processing stage

The contrast adjusted images allow for large scale batch processing of images in MATLAB. The first step of the processing stage was creating a binary image of the crack pattern. The binarization of the image was done with a fixed threshold. The fixed threshold values was acquired from MATLAB using the 'graythresh' function, which uses the Ostu method to threshold a grayscale image [71].

Creating binary images from grayscale images can leave undesired features in the form

of small isolated pixels or regions. Such features can occur due to uneven lighting, hence it is best to apply the band-pass filter to each image before analysis. Effective application of the band-pass filter can eliminate the need to even clean the image. It is also possible that certain unwanted structures are present in the cracking material itself. In case of mud cracks, impurities in the mud appear as small black regions in the binary image. Such impurities can be removed by setting a threshold for object size, below which all objects are deleted. An example of image cleaning is presented in figure 2.7, where the binary image of a blood droplet is shown. In figure 2.7 (a) two crack patterns are presented. The first consists of the large primary cracks with radial symmetry, the second is the pattern formed by the smaller black cracks. The current method isolates the primary crack pattern however, in the process, a small part of the secondary crack pattern appears in the binary image as well. This can be either manually removed or can be removed after creating a skeleton image. The above discussion serves as an example of the process of cleaning a binary image. In general, for images with good contrast (figure 2.7 (a)), it is easy to threshold the image according to the color rather than converting them to grayscale images.
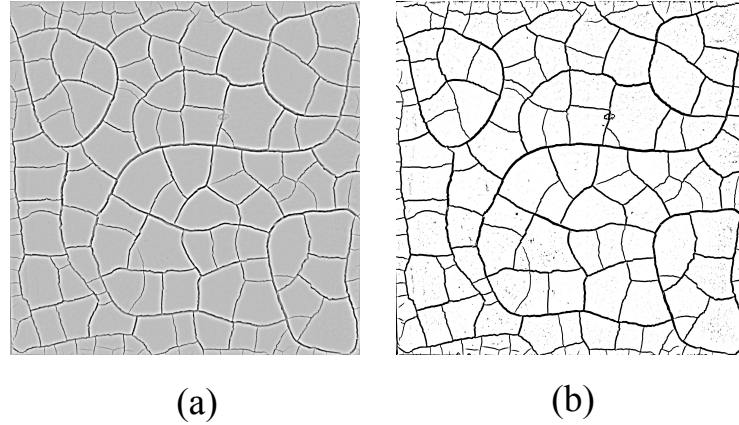


(a)                                    (b)

Figure 2.6: Band-pass filtered and contrast-adjusted images. (a) band-pass filtered image where 3 pixels is the size of the smallest filtered structure and 40 pixels is the largest filtered structure. (b) contrast adjusted image of the figure (a).

A binary image is a single matrix consisting of 0's and 1's which contains the minimum essential information about the crack pattern, it also preserves the shapes and boundaries of the crack pattern. As shown later, in case of the mud cracks, the binary images are used calculate the crack spacing.

Binary images can be further simplified by creating skeleton images. The process of skeletonization involves removing pixels from the edges until structures that are one pixel thick are left over. Figure 2.8 shows binary and skeleton images of a crack pattern. Skeletonization of an image can create spurs, as shown in figure 2.8 (b). Spurs are artificial branches attached to the crack network. They can be as small as a couple of pixels (as seen in figure 2.8 (c)) and can be as big as ten pixels.

While MATLAB has methods to remove spurs, a different approach is used here. A labelled matrix is created from the skeleton image. In the labelled matrix, the pixels in each closed region are assigned a unique value. For example, in figure 2.9, each closed region is
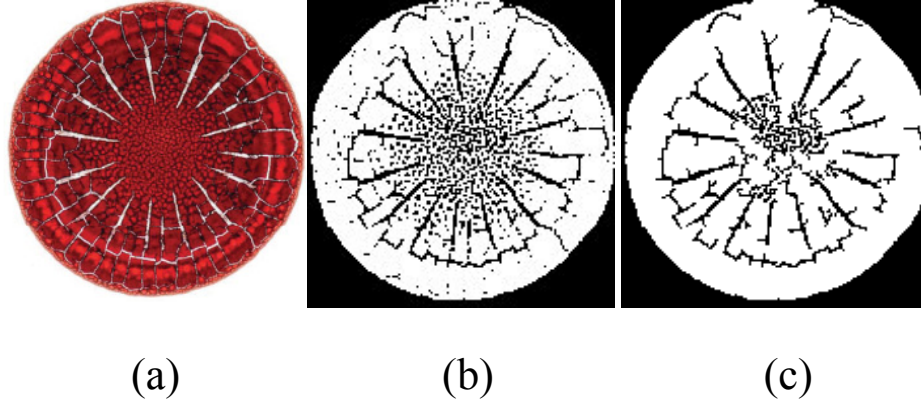
Figure 2.7: Binary image of a blood droplet. (a) the color image of a dried blood droplet (b) contrast adjusted grayscale image. (c) binary image where any feature which is less than 20 pixels in size has been deleted. This ensures that isolated regions and pixels are removed. The pattern in the center of the image is due to the small cracks present in the center of the droplets. Adapted from Brutin et al. [80]

assigned a label. The RGB image in figure 2.9 is a color representation where each label is assigned a distinct color. The images in figure 2.9 are cropped from a larger image which is a skeleton of figure 2.8 (a). The circled numbers in figure 2.9 (a) are a subset of all the closed regions in figure 2.8 (a). A labelled image will contain a set $\mathcal{R}$ number of closed regions

$$\mathcal{R} = \{\mathcal{R}_0, \mathcal{R}_1, \mathcal{R}_2....\mathcal{R}_n..\mathcal{R}_N\} \qquad (2.1)$$

where $N$ represents the total number of regions. All pixels that belong to the $n^{th}$ region where $1 \leq n \leq N$ will have the same value.

A square of length 3 pixels centered around a pixel which is part of the crack network and lies between region 2 and 5 (see fig 2.9 (b) will encompass 9 pixels. This is the pixel neighbourhood which share three label values- $0, 2, 5$. If the same procedure is carried out on a pixel in the pixel neighbourhood of the spur figure 2.9 (b), only two label values will be present- $0$ and $5$. For each pixel that forms the crack pattern, it is possible to define a pixel neighbourhood. Furthermore, a list of labels can be written down which identify the neighbouring labeled regions for each pixel. If $B$ is the total number of black pixels, for the $b^{th}$ black pixel in a labelled skeleton image, where $1 \leq b \leq B$ , it is possible to write a $\mathcal{L}_b$ which is a list of unique label values extracted from the pixel neighbourhood. Then the condition for a pixel to be part of the crack network is

$$n\,(\mathcal{L}_b) \geq 3 \qquad 1 \leq b \leq B, \qquad (2.2)$$

where $n\,(\mathcal{L}_b)$ is the number of elements in the set $\mathcal{L}_b$. Any pixels that do no satisfy this condition are considered spurious pixels. Note, that the set $\mathcal{L}_b$ also contains the label value zero which represents the cracks in the labeled skeleton image. Equation 2.2 becomes an effective criteria for identifying spur pixels. All that remains to be done is to replace the label of the end of spur pixel with that of label of its parent region. In this case, the label of end of spur pixel will be changed from 0 to 5, eliminating the spur. This criteria is set for all
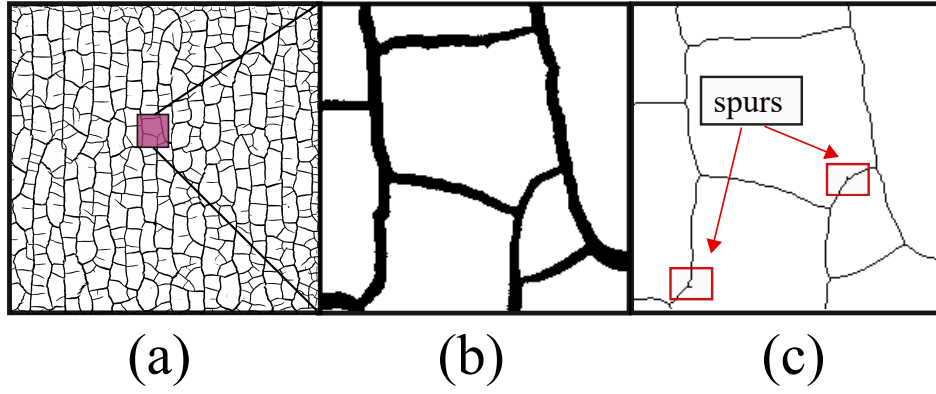
Figure 2.8: Binary and skeleton image. (a) is a binary image. Figure (b) is a section of the binary image of a crack pattern shown in figure (a). Figure (c) shows the skeleton image of figure (b) with spurs. These spurs occur due to the process of creating a skeleton image. Figure (b,c) are 200 pixels by 200 pixels in size.
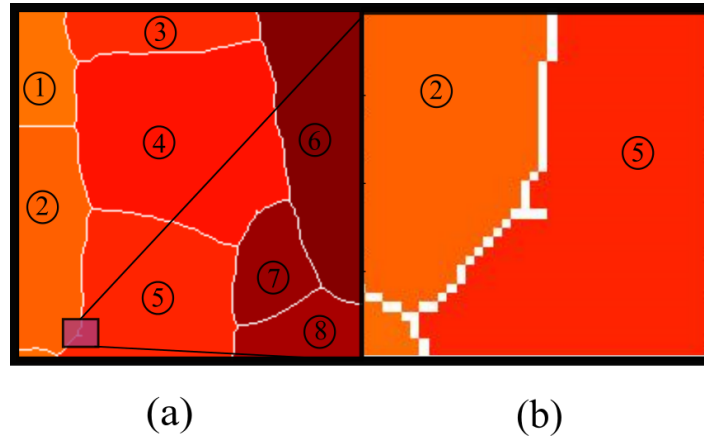


Figure 2.9: Spurs and labels. (a) Labelled matrix converted to RGB. Each of the circled numbers in (a) represents a closed region. (b) Zoom of the indicated region which contains a single spur.

the pixels in the skeleton image. This process not only eliminates spurs but also eliminates unconnected cracks, leaving a connected network of pixels without dead ends.

The labeled matrix approach is useful for not just spur elimination, but also to find crack intersection points. MATLAB has its own node detection algorithm that can be used to detect nodes in a skeleton image. This algorithm is used in some parts of this thesis, mostly due to its advantage of being faster than the labeled matrix approach. However the labeled matrix approach gives good results for a single connected network.

Similar to the spur elimination algorithm, the unique values of labels in a square neighbourhood of $3 \times 3$ pixels around a pixel is extracted from a labeled image. If there are four or more unique labels in the square region, then the pixel is considered to be a crack intersection point. This condition for the $b^{th}$ pixel can be written as

$$n\left(\mathcal{L}_b\right) \geq 4 \qquad 1 \leq b \leq B. \tag{2.3}$$

Figure 2.10 (a) provides a visualization where crack intersection points are identified with

blue circles. Figure 2.10 (b) is a zoom into one of the crack intersection points. The crack intersection point lies at the intersection of more than three regions



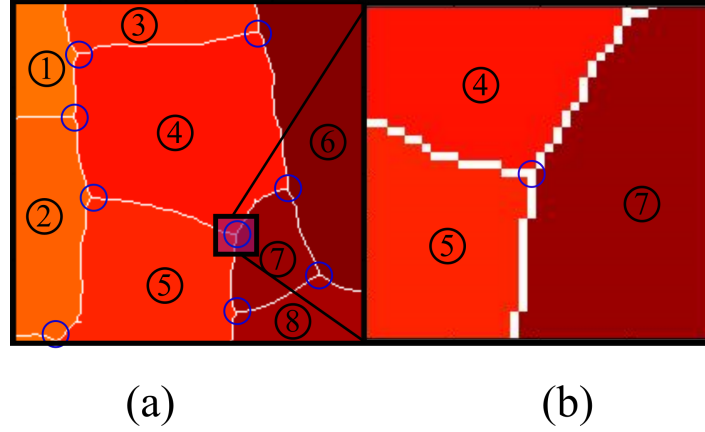(a)                                           (b)

Figure 2.10: Crack intersection points.    (a) Blue circles indicate crack intersection points. (b) Three regions  (regions 4, 5, and 7) surround a crack intersection point. A square region around a crack intersection point will overlap with three label values. Notice that this overlap is true for all the crack intersection points in  (a).

### 2.2.3    Vertex connectivity

Each crack intersection point is connected to other crack intersection points.  The next logical step is to find out, given a crack intersection point, what are its neighbouring crack intersection points?

Two crack intersection points $c_1$ and $c_2$ are neighbours if and only if the condition

$$\mathcal{M} = n \left( \mathcal{L}_{c_1} \cap \mathcal{L}_{c_2} \right) = 4 \tag{2.4}$$

is satisfied where $\mathcal{M}$ is the total number of elements in the intersection of two labels. This can be seen in figure 2.9 (a). For instance, the crack intersection point formed by regions 1,2 and 4 has three neighbours. The condition in equation 2.4 is tested for all pairs of crack intersection points and a list of neighbours is compiled.

For each crack intersection point c , $\mathcal{N}_c$ can be defined as a list of its neighbours. For example, for point A the $\mathcal{N}_A = \{B, C, D\}$. This list of neighbours is calculated for all crack intersection points and used to make measurements on the crack network. The details of these measurements will be covered in the next chapter.

## Summary

This chapter presents the sequence of image processing steps: starting from the experimental procedure to finally acquiring a binary, skeleton image along with a connectivity matrix for crack intersection points.

The experimental procedure for generating crack patterns is described in the first section of the chapter, followed by a brief description about the types of crack patterns observed
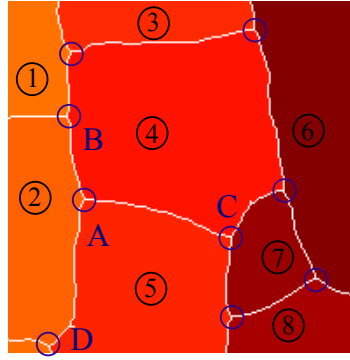
Figure 2.11: Neighbours algorithm. Point A is at the intersection of three regions -2, 4 and 5 and has three neighbours, points B, C and D. With point B, point A shares two regions- 2 and 4. With point C, it shares two regions- 4 and 5. With point D, it shares region 2 and 5. Apart from this, the third region, which is shared by all the crack intersection points is the crack pattern skeleton. This algorithm is repeated for all crack intersection points.

with increasing layer height. Two set of plates are used where radial plates 1 and 2 generate crack patterns with radial symmetry. The main control parameter for the experiments is the layer height. The layer height depends on the mass of bentonite used during each trial of the experiments. In a sequence of trials, the bentonite mass is increased by 10 grams and crack patterns are generated.

Images of the crack pattern are captured and processed. The image processing step is needed to ensure the quantification of the crack pattern. Raw images of the crack pattern, which are in jpeg format are converted to 8 bit, then a band-pass filter is applied to them. Structures upto 40 pixels and down till 3 pixels are filtered. The filtering process removes uneven lighting especially shadows. The filtered image is contrast adjusted to generate a grayscale image. This grayscale image is converted to a binary image, then to a skeleton image.

The second part of image processing involves elimination of spurs and the acquisition of crack intersection points, its neighbours and a connectivity matrix. Spurs are eliminated by converting a skeleton image of a crack pattern to a labelled image, then checking pixel neighbourhood of all the pixels that form a connected crack network. By applying equation 2.2 to the pixel neighbourhood spurs are eliminated. Crack intersection points are also identified in a similar way, where equation 2.3 is use to decide if a point qualifies as a crack intersection point or not. Once the crack intersection points have been identified, its first neighbours are identified and stored as a list.

In the next chapter, all the components- from the binary image to the list of neighbours for each crack intersection points, are used to define measures of a crack pattern

# Chapter 3

# Analysis of crack patterns

In the previous chapter, the prerequisites for analysis of a crack pattern were developed. These prerequisites are: a labeled skeleton image of the crack pattern, a list of all the crack intersection points and a list of neighbours of each crack intersection point. Using these, the tools required to quantify these crack patterns are developed in this chapter.

So far, the description of crack patterns has been limited to a qualitative classification of being wavy, ladder-like and isotropic. This chapter presents methods which attempt to quantify the structure of a crack pattern. The methods are presented for images of sinusoidal plates, and unless stated otherwise, also apply to radial plates. These analysis methods are later applied to images of crack patterns for increasing layer heights, the data and the interpretation is presented in the next chapter.

The content of this chapter is roughly divided into two sections, as shown in figure 3.1. The first section deals with various measures which provide robust methods for quantifying crack patterns. They condense information about the crack pattern into a single number, which can be used, as seen in the next chapter, to show how substrates affect a crack pattern with changing layer height. Three measures for a crack pattern are presented: the orientation of crack intersection point neighbours, the orientation of cracked regions and the orientation of individual cracks. The first order parameter involves measuring angles at crack intersection points. Here angles are measured between the horizontal and $\vec{\mathbf{r}}_{ij}$, which is the vector between the $i^{th}$ crack intersection point and its $j^{th}$ neighbour. The crack angles are measured for neighbours of the $i^{th}$ crack intersection point using which an angle distribution is generated. This angle distribution is condensed into a single value. In this section, the methods to calculate angles for both sinusoidal and radially sinusoidal plates are described. Angles are calculated for a crack pattern on sinusoidal and radially sinusoidal plates and the resulting angle distributions are shown. The angles distributions are multiplied with a $\cos(4\theta)$ function and the value for $S_{Angles}$ is calculated. This value is used as a measure of order of a crack pattern in the next chapter.

The second measure is the orientation of cracked regions. This parameter involves detecting isolated cracked regions, fitting them with ellipses, and measuring their orientation. The average value of the orientation, $S_{Ort}$, is used as measure of order. The orientation of each ellipse is a local measure of the order. The required methods to detect the cracked regions

and calculate their orientation are described.

The third measure is the measurement of crack orientation, using methods developed for measuring the orientation of cracked regions, the orientation of crack skeletons is measured and angle distributions are plotted. The angle distributions calculated from the measurement of crack orientation are analyzed in the same way as the angle distributions acquired from measuring angles around crack intersection points. This method is similar to the first measure since both involve calculating the orientation of cracks. This method is a direct measure of the orientation of the cracks; it can be applied to unconnected cracks as well, whereas the first measure requires a crack network in order to be used.

The second set of topics covered in the chapter involve two global methods of quantifying crack patterns- the Manhattan metric and the Minkowski parameters. Other methods which assist in describing the crack pattern quantitatively are- calculation of the crack spacing, determination of crack lengths and determination of number of crack per wavelength of the sinusoidal plate using Fourier methods.

The Manhattan metric approach is an attempt to define a global order parameter. The Manhattan metric provides a measure of the distance between two points on a grid by traversing either in the $x$ direction or the $y$ direction, but not a combination of both. Such a metric is used to study geometries known as taxicab geometries. Simple examples of taxicab geometries are, traveling in the grid like streets of Manhattan ( after which the metric has been named) or moving on a chessboard. The analogy of the Manhattan metric is used to calculate the distance traveled along the cracks between two crack intersection points. A ratio of the straight line distance between the two crack intersection points and the distance traveled along the crack is used to define a parameter $s_{Man}$. This parameter is calculated for all pairs of crack intersection points which are sorted based on the symmetry of the substrate. The mean of $S_{Man}$ is used to represent a measure of order of the crack pattern.

Another global parameter that is presented uses Minkowski parameters to quantify the structure of a crack pattern. The Minkowski parameters are defined in the context of a foreground and a background of a spatially varying pattern. The foreground in the current case are the crack intersection points which are plotted as single black pixels on a background of white pixels. For increasing radii of disks that have their origins at these single pixels, the three Minkowski parameters for two dimensions - the area, the boundary and the Euler number are measured. A sample crack pattern is analyzed using the Minkowski parameters and results are plotted for increasing radius of disks. The Minkowski parameters, unlike the previous order parameters are not presented as a single value that provides a measure of the crack pattern. Instead three plots, one for each Minkowski parameter, are generated and shown.

The Minkowski parameters are followed by methods which describe the measurement of the crack spacing of a crack pattern. The crack spacing is measured in order to detect correlations between the substrate structure and the geometry of the crack pattern. Furthermore, the crack spacing of an isotropic crack pattern is known. Hence, the question asked is: will crack spacing at large layer heights approach the crack spacing for previously measured

isotropic crack patterns? The crack spacing is measured in two ways. One involves using the line dropping method where lines are plotted on a skeleton image of the crack pattern and the distances between the crack and line intersections are measured and averaged. The second method involves measuring the areas of cracked regions. The side of a square of the same area is also used as a measure of the crack spacing.

The lengths of cracks are measured in order to calculate and study the change in the distribution of crack length. The length of each crack is measured using the same methods developed in the section where orientation of cracks are measured.

The final section of this chapter is one where Fourier methods are used to analyse the crack pattern generated on a sinusoidal substrate. This is necessary in order to determine for a given layer height, and answer of how many cracks there are per wavelength in a mature crack pattern. The methods to calculate the spectral power of the crack density of a sample crack pattern are described using the example of a ladder-like crack pattern. The spectral power is plotted against the wave-number, which represents the number of wavelengths in the dimensions of the sinusoidal plate.

**Analysis of crack pattern**

**Measures**            **Other methods**

| Crack angles distribution |
|---|

| Orientation of cracked regions |
|---|

| Orientation of cracks |
|---|

| Manhattan metric |
|---|

| Minkowski parameters |
|---|

| Crack spacing |
|---|

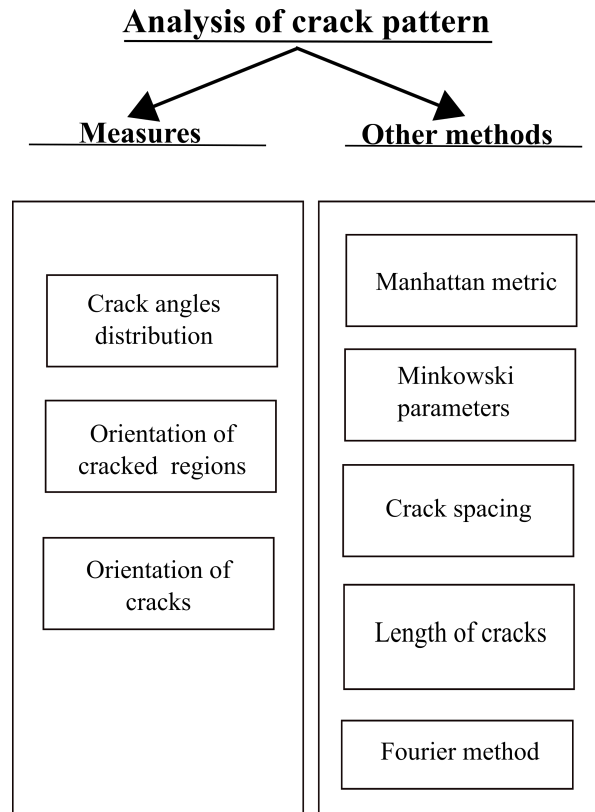| Length of cracks |
|---|

| Fourier method |
|---|

Figure 3.1: An outline of the topics in the chapter. The chapter can be divided into two sections. The measures aim to assign a single number to a crack pattern which quantifies the effect of the substrate on the crack pattern, while the second section contains various methods to describe the geometry and topology of a crack pattern.

## 3.1 Crack angles distribution

The distribution of crack angles serves as a useful tool for comparison of crack patterns. In this section the methods to acquire the angle distribution and the subsequent order parameters are presented. A skeleton image of the crack pattern is used to measure the crack angles. In the skeleton image, after identifying each crack intersection point, the crack angles are calculated between the horizontal unit vector $\hat{x} = [1\ 0]$ and $\vec{r}_{ij}$, which is the vector that connects the $i^{th}$ crack intersection point with its $j^{th}$ neighbours. Take the example in figure 3.2. Let $\hat{x}$ be the horizontal unit vector that lies on the dashed green line. Then, the angle $\theta_1$ is defined by -

$$\cos\theta_1 = \frac{\vec{r}_1 \cdot \hat{\mathbf{x}}}{|\vec{r}_1|}. \tag{3.1}$$

Similarly $\theta_2$ and $\theta_3$ can be calculated. Figure 3.2 (a) is an image of the crack pattern, and figure 3.2 (c) is the corresponding angle distribution.
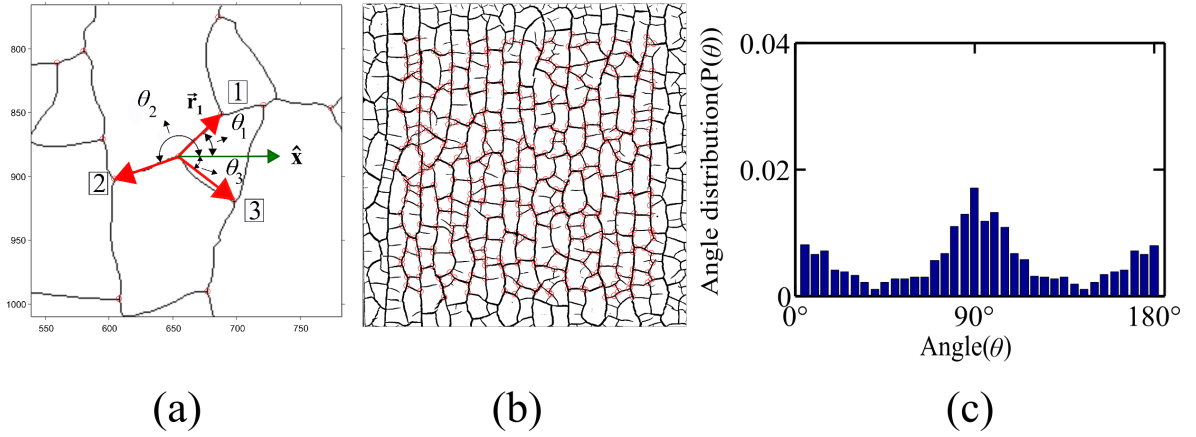


Figure 3.2: Angle distribution of a crack pattern over sinusoidal substrate. (a) depicts the the three neighbouring crack intersection points to the $i^{th}$ crack intersection point. The red vectors join the crack intersection point to its neighbours, an example of this it the vector $\vec{r}_1$. The angle $\theta_1$ is defined between the $1^{st}$ crack intersection point and the green vector which is $\hat{x} = [1\ 0]$, it is perpendicular to the peak. (b) represents the full crack pattern from which the crack intersection point in (a) is selected. The red points are the crack intersection points. Figure (c) is an angle distribution of the all the measured angles. This angle distribution goes from $\theta = 0°$ to $\theta = 180°$ and has 36 bins.

For the radial crack pattern in (figure 3.3), a crack intersection point and its neighbours are shown in figure 3.3 (a). The equivalent of the horizontal vector $\hat{x}$ is the radial unit vector $\hat{r}_{\parallel}$ which is parallel to the vector that connects the center of the image and the $i^{th}$ crack intersection point. The angle $\theta_1$ is calculated using-

$$\cos\theta_1 = \frac{\vec{r}_1 \cdot \hat{\mathbf{r}}_{\parallel}}{|\vec{r}_1|}. \tag{3.2}$$

For all crack intersection points, angles between $\vec{r}_{ij}$ and the direction of the substrate $\hat{x}$ or $\hat{r}_{\parallel}$ (depending on the system's symmetry) are calculated and plotted as a histogram. The
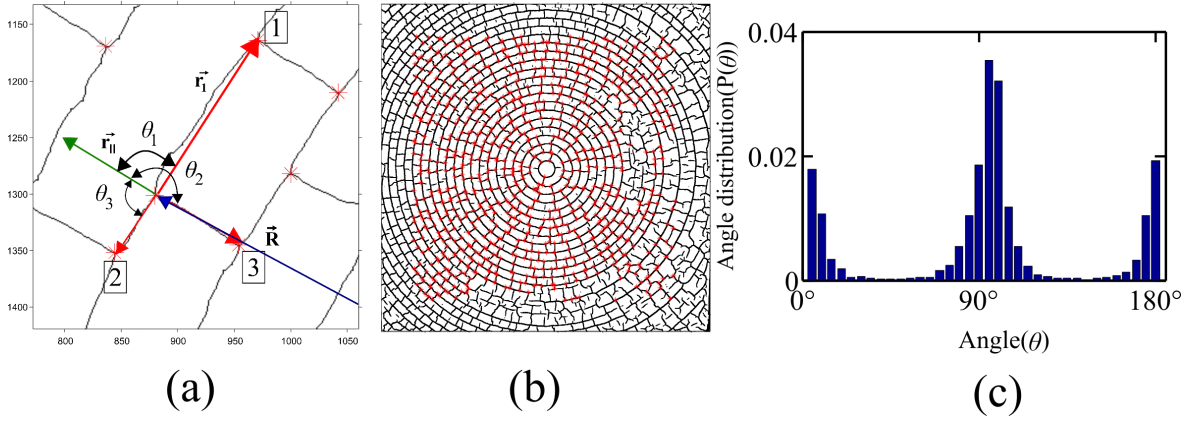
Figure 3.3: Angle distribution of a crack pattern over radial sinusoidal substrate. (a) shows the neighbours of the $i^{th}$ crack intersection point which is part of a crack pattern generated on a radially sinusoidal plate. The blue vector connects the center of image and the $i^{th}$ crack intersection point. The vector $\hat{\mathbf{r}}_\parallel$ is the vector perpendicular to circle lying atop the peak. This vector is parallel to the blue vector. Figure (b) is a radially symmetric crack pattern generated over the radially sinusoidal substrate. The red points are crack intersection points. Figure (c) is angle distribution for the image in (b). The majority of the angles lie around $0°, 90°$ and $180°$.

histogram satisfies the equation -

$$\frac{1}{N} \sum_{i=1}^{N} \mathrm{P}' (\theta_i) d\theta = M, \tag{3.3}$$

where $\mathrm{P}' (\theta_i)$ is the probability distribution for the angles. N is the total number of bins for the angle distribution. $\theta_i$ refers to the center value of the $i^{th}$ bin. In general, $N = 36$ bins are used to generate the angle distributions, hence $\theta_1 = 2.5°, \theta_2 = 7.5°$ and so on. M is the total number of angles measured over all crack intersection points. The probability distribution is normalized by dividing the total count of angles in each bin by M such that,

$$\frac{1}{N} \sum_{i=1}^{N} \mathrm{P} (\theta_i) d\theta = 1 \tag{3.4}$$

where $\mathrm{P} (\theta_i) = \mathrm{P}' (\theta_i)/M$. Since each crack pattern will have varying numbers of crack intersection points and hence varying number of measured angles, applying this normalization condition scales the angle distribution such that it falls between 0 and 1 allowing for direct comparison between two crack patterns.

Sample angle distributions are presented in figure 3.2 (c) figure 3.3 (c). For the crack pattern in figure 3.3 (b), the angle distribution has peaks at $\theta = 0°, 90°, 180°$ (figure 3.3 (c)). Once an angle distribution has been generated, it is multiplied by a $\cos 4\theta$ function and summed over $\theta$ to give the following order parameter,

$$\mathrm{S}_{\mathrm{Angles}} (\theta) = \sum_{i=1}^{N} \left[\cos (4\theta_i) \, \mathrm{P} (\theta_i))\right], \tag{3.5}$$

where $N$ is the total number of bins of $\theta$.

From equation 3.5, $S_{\text{Angles}}$ will lie between 1 and -1. The $S_{\text{Angles}} = 1$ case represents cracks that lie parallel to the substrate, while $S_{\text{Angles}} = 0$ case represents an isotropic crack pattern, and $S_{\text{Angles}} = -1$ caseS represents cracks that lie at $45°$ from the substrate.

The $S_{\text{Angles}}$ parameter requires prior information about the symmetry of the crack pattern. For example, in case of the radial plates, without knowing about the radial symmetry of the substrate, it is not possible to determine whether equation 3.1 or equation 3.2 should be used to calculate the angle distribution. However, once the symmetry has been determined, $S_{\text{Angles}}$ allows for comparisons between crack patterns (presented in the next chapter). It simplifies an angle distribution down to a single number that can be assigned to each crack pattern.

## 3.2  Orientation of cracked regions

In a mature crack pattern, intersecting cracks form closed loops that create isolated regions of the cracking material. This is shown in figure 3.4. The orientation of these cracked regions is calculated and the average orientation is used as a measure of the crack pattern.

A single isolated cracked region in a binary image can be described using a function $B\left(x_i, y_i\right)$ which sets all the pixels within the isolated region to zero and all the points outside the region to one. $B\left(x_i, y_i\right)$ can be though of as a intensity level in an image where -

$$B\left(x_i, y_j\right) = \begin{cases} 1 \text{ pixel outside cracked region} \\ 0 \;\; \text{pixel inside cracked region} \end{cases} \tag{3.6}$$

where the $\left(x_i, y_j\right)$ coordinates represent the pixel locations in the image. $i = 1..B$, $j = 1..B$ where $B$ is the total number of pixels in the image. In the above argument, the function $B\left(x_i, y_i\right)$ represents a single cracked region as a discrete body. For ease of description the cracked region will be considered a continuous body, hence $x_i \to x$ and $y_i \to y$.

The central moments of the cracked regions are calculated, using which the orientation $\theta$ is given by [24]

$$\tan 2\theta = \frac{b}{c-a}, \tag{3.7}$$

where $a, b$ and $c$ are the central moments are defined by,

$$a = \iint x'^2 B\left(x', y'\right) \, \mathrm{d}x'y' \, \mathrm{d},$$
$$b = 2 \iint x'y' B\left(x', y'\right) \, \mathrm{d}x'y' \, \mathrm{d}, \tag{3.8}$$
$$c = \iint y'^2 B\left(x', y'\right) \, \mathrm{d}x'y' \, \mathrm{d},$$

where $x' = x - \bar{x}$ and $y' = y - \bar{y}$ where $\left(\bar{x}, \bar{y}\right)$ are the coordinates of the centroid of the image. A covariance matrix is defined using $a, b$ and $c$ whose eigenvalues are the major and minor axis of an ellipse [24]. Figure 3.4 shows the elliptical fit of cracked regions of two crack patterns.
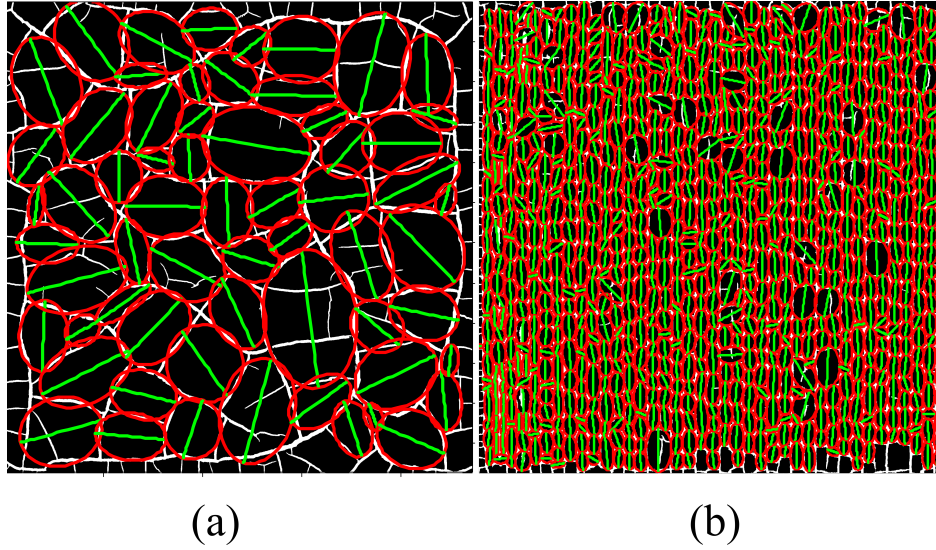
<div align="center">(a)          (b)</div>

Figure 3.4: (a) shows the elliptical fits of cracked regions which form an isotropic crack pattern. The red curves represent the ellipses and the green lines represent the major axes of the ellipse. The major axes of majority of the ellipses do not align with the y direction (bottom to top of the image). (b) shows the elliptical fits on cracked regions which form a ladder-like crack pattern. The ellipses are aligned in the y-direction.

The orientation of each cracked region is calculated and the the measure $S_{Ort}$ is defined where

$$S_{Ort} = \langle \cos\ (2\theta) \rangle,$$

this leads to

$$S_{Ort} = \begin{cases} 1 & \text{major axis of the ellipses parallel to the substrate} \\ 0 & \text{major axis at } 45° \text{ to the substrate} \\ -1 & \text{major axis perpndicular to the substrate} \end{cases} \tag{3.9}$$

MATLAB provides a convenient way to calculate properties of isolated cracked regions. The MATLAB function 'regionprops' measures many object properties. Out of the list of object properties from 'regionprops', the following are used for visualizing the elliptical fits and calculating the value of $S_{Ort}$ - Orientation, Area, Centroid, MinorAxisLength and MajorAxisLength. The Orientation property uses equation 3.7 in order to calculate the angle of the cracked region with respect to the substrate. The Area property is used as criteria in order to exclude smaller pieces, especially along the edges, from influencing the total average value. Only if the condition $(Area) > 100$ pixels is satisfied, a region is used in the final calculation for $S_{ort}$. The Orientation, Centroid, MajorAxisLength and MinorAxisLength quantities are used to draw an ellipse around a single cracked region (See figure 3.4)

## 3.3 Orientation and length of cracks

The individual cracks in a crack pattern can be isolated. To achieve this, starting from a gray-scale image, a skeleton image is acquired. In the skeleton image, the crack intersection

<div align="center">39</div>

points are identified. A square of length 3 pixels is drawn around each crack intersection point. The value of the pixels inside this neighbourhood is set to the value of the pixels in the un-cracked region of the image. This means that the value of all the pixels inside the square region is set to 1. This deletes crack pixels in the square disconnecting the crack network and leaving individual cracks as independent pieces which can be detected and measured using the methods in the previous section (i.e 'regionprops'). A typical example is presented in figure 3.5. The crack pattern in figure 3.5 (a) is reduced to a skeleton image, then, as shown in figure 3.5 (b) a square is drawn around the crack intersection points. In figure 3.5 (c) the regions deleted around the crack intersection point are highlighted. Deleting crack intersection points on both ends of the crack isolates the crack from the network. In figure 3.5 (d), all the isolated crack skeletons are detected and ellipses are drawn around each isolated piece representing a crack.
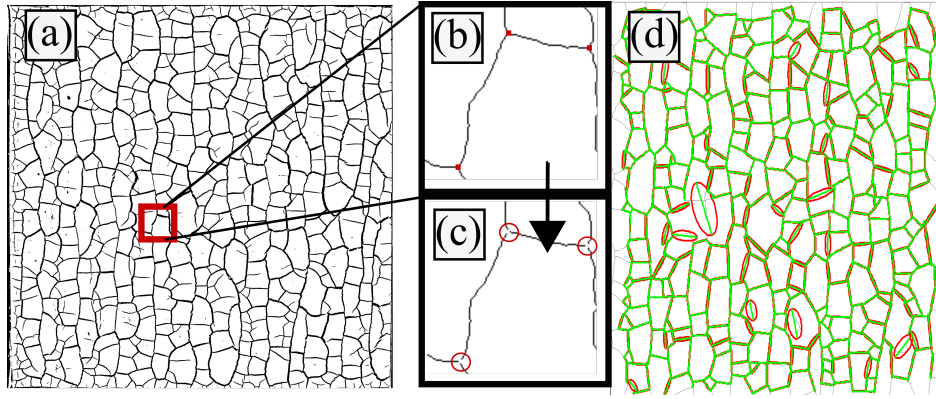


Figure 3.5: Figure (a) A sample crack pattern using which a crack skeleton is created. In figure (b) the red regions are crack intersection points. The black pixels in these regions are removed leaving crack skeletons isolated from the crack network. In figure (c), the regions near the crack intersection points have been replaced with white pixels, they are identified with red circles. Figure (d) shows all detected isolated crack skeleton. Similar to figure 3.4 the isolated objects are detected using 'regionprops'. The red regions represent the boundaries of the elliptical fit and the green lines are the major axis of the fitted ellipse.

Two measurements are made on isolated skeletons of cracks. These measurements are the crack orientation and crack length.

### 3.3.1 Orientation of cracks

The orientation of cracks is measured by creating isolated crack skeletons then using 'regionprops' to detect and measure them. Similar to section 3.2 (Orientation of cracked regions), the orientation of each crack skeleton is acquired from the 'Orientation' property of 'regionprops'. Orientations are rescaled to lie in between $0°$ and $180°$ and plotted as an angle distribution in a similar fashion to figure 3.2 (c). Similar to figure 3.2 (c), the normalized angle distribution is multiplied with $\cos 4\theta$ and the parameter $C_{Ort}$ is calculated according

to equation 3.5. The value of $C_{Ort}$ is compared with $S_{Angles}$ figure 3.2 (c) is

$$S_{Angles} = 0.41$$
$$C_{Ort} = 0.40$$

(3.10)

The parameter $C_{Ort}$ serves as a comparison to $S_{Angles}$ . Both parameters measure the orientation of the cracks that lie between two crack intersection points. Measuring the orientation of crack skeletons is a more general approach since it does not require a connected crack pattern. Such a method is applicable beyond crack patterns as well, wrinkle ridges on the surface of Mars [34] to networks and beyond. Wrinkle ridges are unconnected structures which form due to contraction of lava during cooling. They tend to form near the edges of craters and such features can be quantified by the same methods used the calculate $C_{Ort}$ .

### 3.3.2   Length of cracks

In the previous section, isolated cracks were detected using 'regionprops'. One of the outputs of 'regionprops' is 'PixelList'. This provides a list of pixels belonging to the detected object. Using this list, two quantities pertaining to the crack length are acquired- the average crack length and the distribution of crack lengths. The basic algorithm to acquire each of these quantities is presented here. Comparisons between crack patterns from different plates and over a range of layer heights are presented in the next chapter.

Using the pixel list of the detected object, the end points of each crack must be identified. This is done using the endpoints algorithm in the function 'bwmorph'. Alternatively, the end points can be identified by going pixel by pixel in the pixel list and counting the number of neighbouring black pixels. For the pixels which have only one black pixel as a neighbour, this is assigned as the endpoint of the isolated crack.

The values in 'PixelList' are stored in an $n \times 2$ array. The first pixel in 'PixelList' will be the pixel with the lowest $x$ and $y$ coordinates. An example of this is shown in figure 3.6 (a), where the yellow box represents a pixel which has the lowest x and y coordinates in the collection of pixels which represent the isolated crack skeleton. In order to get the crack length, the following operations are performed on 'PixelList' -

- Since the end points have been identified, the distance between a single endpoint and each pixel in the crack skeleton is calculated. This is represented by

$$d_i = \sqrt{(y_i - y_{end})^2 + (x_i - x_{end})^2}$$

(3.11)

where $x_{end}$ and $y_{end}$ are the coordinates of one of the end points of the crack skeleton (in figure 3.6 (a), shown as red points) $x_i$ and $y_i$ are the coordinates of a pixel in the crack skeleton. All the distances between $(x_{end}, y_{end})$ and the rest of the crack skeleton pixels are stored in $d$, where $d_i$ represents the distance between the $i^{\text{th}}$ element of 'PixelList' whose coordinates are $(x_i, y_i)$ and the end point whose coordinates are $(x_{end}, y_{end})$.

- The collection of distances is contained within the array $d$ which is sorted such that $d$ goes from the smallest to the largest value; the first element represents the end

point pixel $(x_{end}, y_{end})$ hence $\mathsf{d}_1 = 0$. The rest of $\mathsf{d}$ goes from the closest pixel to $(x_{end}, y_{end})$ till the second end point. The last element of the sorted $\mathsf{d}$ array is the distance between the two end points of the crack skeleton. Sorting $\mathsf{d}$ requires a sequences of rearrangements of its elements, this sequence of rearrangements is applied to 'PixelList'. This ensures that the first and the last element of 'PixelList' are the end points of the crack skeleton and 'PixelList' represents the sequence of pixels going from one end point to another.

- The distances between each pixel in 'PixelList' is calculated and to this, the distance between the end points and the nearest crack intersection points is added to this. The distances are summed and this sum represents the crack length for a single crack skeleton

- The crack length is divided by the x-dimension of the whole image which is in pixels. This normalizes the crack length. For example, the x dimension of the full image of the crack skeleton represented in figure 3.6 (a), is 1830 pixels, the normalized crack length is 0.0208. The normalized crack length is multiplied by 20 cm which is the width of the container. The gives the crack length in centimetres. For figure 3.6 (a), the crack length is 0.416 cm.

The above algorithm provides a method to calculate the crack length of a single crack. This algorithm is applied to all cracks in a skeleton image of a crack pattern and a crack length distribution is generated. The crack length distribution for figure 3.2 (b) is shown in figure 3.6 (b).
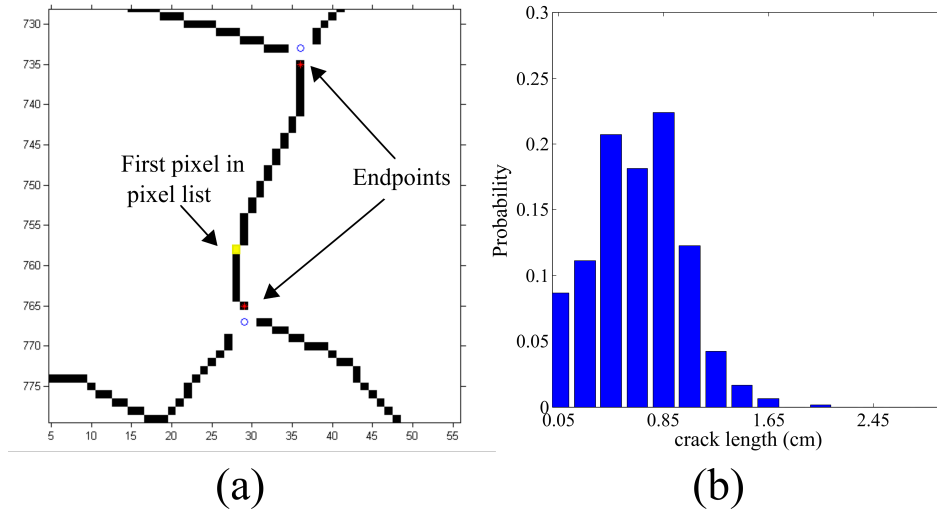


(a)            (b)

Figure 3.6: Figure (a) is a cracked skeleton. Two red points (towards the top of the image and the bottom of the image) highlight the end points of the crack skeleton. The blue circles near the end points indicate the crack intersection points. To accurately calculate the crack length, the pixel to pixel distance between each pixel on the crack skeleton is calculated, in addition the distance between the end points of the crack skeleton and the closest crack intersection points are also calculated. Figure (b) is the normalized distribution of crack lengths for figure 3.5 (d)
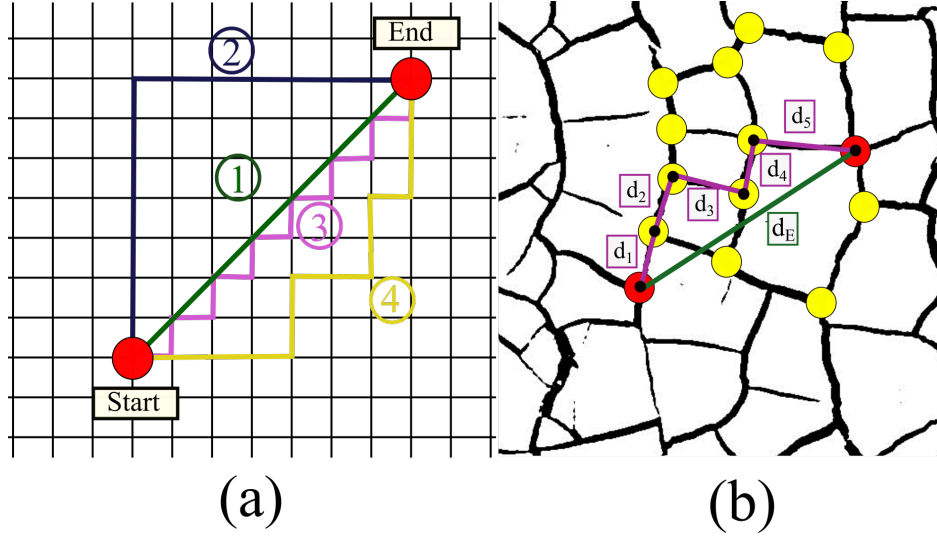
.

Figure 3.7: (a) A cartoon of a taxicab geometry. Line 1 is the path that minimizes the Euclidean distance between two points. This path is unique. For the Manhattan distance in figure (a) the path is not unique, all the paths 2, 3 and 4 have the same Manhattan distance. Figure (b) shows two paths. The first path (green line) $d_E$ shows the Euclidean distance between the two crack intersection points, the second path (purple line) which shows the Manhattan distance. The ratio $d_E/d_{Man}$ will be $1/\sqrt{2}$ for a grid like structure.

## 3.4 Manhattan metric

The Manhattan metric provides an alternate method to measure distances between crack intersection points.

In Euclidean geometry, the shortest path between two points is a straight line. The norm of the vector that connects two points is the Euclidean distance. In $\mathbf{R}^2$, this distance is $d = \sqrt{(y_2 - y_1) + (x_2 - x_1)}$. There are some geometries where Euclidean distances cannot be calculated. An example of this is the grid presented in figure 3.7 (a). Staying on the grid from the start node to end node is possible only by travelling either in the x direction or along the y direction. Such a geometry is known as the taxi-cab geometry. A combination of transverse displacements along both x and y direction, which is the essence of the Euclidean distance, is not possible in a taxicab geometry. Since the shortest distance between two points cannot be defined in terms of Euclidean distance, a new metric is defined. This metric is known as the Manhattan metric [56]

$$m = |x_1 - x_2| + |y_1 - y_2| \tag{3.12}$$

Hence, the distance between two points in a Cartesian coordinate system can be measured using either the Euclidean distance, or by the Manhattan distance if restricted to moving on a grid. While in the case of the Euclidean distance there is only one path which minimizes the distance between two points, in the case of the Manhattan metric, there are multiple paths that minimize distances between two nodes on a grid.

Moving on a crack pattern is similar to moving along a grid. The crack intersection points

become the nodes of the grid, and the cracks become the connecting lines between nodes. However, the analogy ends there. Depending upon the crack pattern, each neighbouring pair of nodes or crack intersection points are connected by curves. Hence the distances between these crack intersection points are apporoximately Euclidean. In case of ladder-like crack pattern, these curves are horizontal or vertical cracks similar to a grid, in case of an isotropic crack pattern, these curves can be meandering cracks with curvature.

The general definition for the Manhattan distance, on a crack pattern, between two non -neighbouring crack intersection points is

$$d_{Man} = \sum_{i=1}^{N} d_i \tag{3.13}$$

where $d_i$ represents the Euclidean distance between two neighbouring crack intersection points. In figure 3.7 (b), $d_{Man}$ is the sum of the $d_1$ to $d_5$. The Euclidean distance $d_E$ between the two crack intersection points is presented for comparison.

In figure 3.7 (b), $d_{Man}$ is dependent on the geometry of the crack pattern, whereas $d_E$ is dependent on the location of the crack intersection points in real space. For all pairs of non neighbouring crack intersection points, the condition

$$d_E \leq d_{Man} \tag{3.14}$$

holds true. On a ladder-like crack pattern, travelling from a crack intersection point on the top of the image to the bottom of the image, the ratio of $d_E$ and $d_{Man}$ would be close to 1. Whereas, in case of an isotropic crack pattern, this is not the case. The ratio of $d_E$ and $d_{Man}$ is represented as-

$$s_{Man} = \frac{d_E}{d_{Man}} \tag{3.15}$$

The parameter $s_{Man}$ is calculated for a single pair of crack intersection points. For sinusoidal plates, $s_{Man}$ is calculated for all crack intersection points that form pairs between the top part of the image to bottom -

$$S_{Man} = \sum_{i=1}^{N} \frac{(s_{Man})_i}{N} \tag{3.16}$$

where $N$ is the number of pairs of crack intersection points.

Taking figure 3.8 (a) as an example, $S_{Man}$ is calculated in the following way -

- Starting with a labeled skeleton image of the crack pattern, the crack intersection points are detected . For each crack intersection point, its neighbours are identified.

- The crack intersection points are sorted according to their location. All crack intersection points that lie in top 1/3 and the bottom 1/3 of the image are stored in a separate arrays. Figure 3.8 (a) shows sorted crack intersection points on a crack pattern.

- An adjacency matrix is calculated for all crack intersection points. This is done by creating an $N \times N$ matrix, where $N$ is the number of crack intersection points. The neighbours for each crack intersection point are identified from the neighbours list and the Euclidean distance between is stored in the adjacency matrix as -

$$A[i,j] = \sqrt{(y_j - y_i) + (x_j - x_i)} \qquad (3.17)$$

where $A$ is the adjacency matrix and where $i$ and $j$ are neighbouring crack intersection points. For the $i^{th}$ column of A, only those rows are non zeros whose index represent the neighbours of the $i^{th}$ crack intersection point are non zero, the rest of the rows are zero. Figure 3.8 (b) shows a simple cartoon of whose adjacency matrix is-

$$A = \begin{pmatrix} 0 & 0 & d_{13} & 0 & 0 & 0 \\ 0 & 0 & d_{23} & 0 & 0 & 0 \\ d_{31} & d_{32} & 0 & d_{34} & 0 & 0 \\ 0 & 0 & d_{43} & 0 & d_{45} & d_{46} \\ 0 & 0 & 0 & d_{54} & 0 & 0 \\ 0 & 0 & 0 & d_{64} & 0 & 0 \end{pmatrix} \qquad (3.18)$$

- Pairs of crack intersection points are constructed where one crack intersection point belongs to the top part of the image and the second point belongs to the bottom of the image.

- For each pair of crack intersection points, the angle between the substrate and vector connecting the pair of crack points is calculated. If the angle lies in between $-5°$ and $5°$ ( where $0°$ is parallel to the ridges on the substrate) then, the pairs of crack intersection points combined with the adjacency matrix are put into the MATLAB function 'graphshortestpath', otherwise the pair is ignored. For each pair of crack intersection points, this function uses the Djikstra algorithm [73] to find the shortest path between two points on a network. 'graphshortestpath' outputs the sequence of crack intersection points needed to travel in order to get from the starting crack intersection point to the ending crack intersection point. Using Euclidean distances in the adjacency matrix, it also outputs the total distance travelled along the crack pattern. This distance is stored in a separate array. The distance along the crack between pairs of neighbours is calculated for all pairs.

- The Euclidean distance between the pair of crack intersection points is calculated for all pairs. This is divided by the distance acquired using 'graphshortestpath' and the final result is averaged which gives the value of $S_{Man}$.

For radial crack patterns, the pairs are sorted by considering crack intersection points which are inside a circle that has a diameter of $1/4$ of the image and crack intersection points that are located outside a circle with a diameter $1/3$ the size of the image. Both the circles are centred about the image. The pairs are formed by selecting one crack intersection point from the inside region and another crack intersection point from the outside region. The rest of the analysis is carried out in a similar fashion.

In case of ladder-like cracks $S_{Man}$ tends to be close to 1, for isotropic crack patterns the lower limit of the value is $1/\sqrt{2}$.
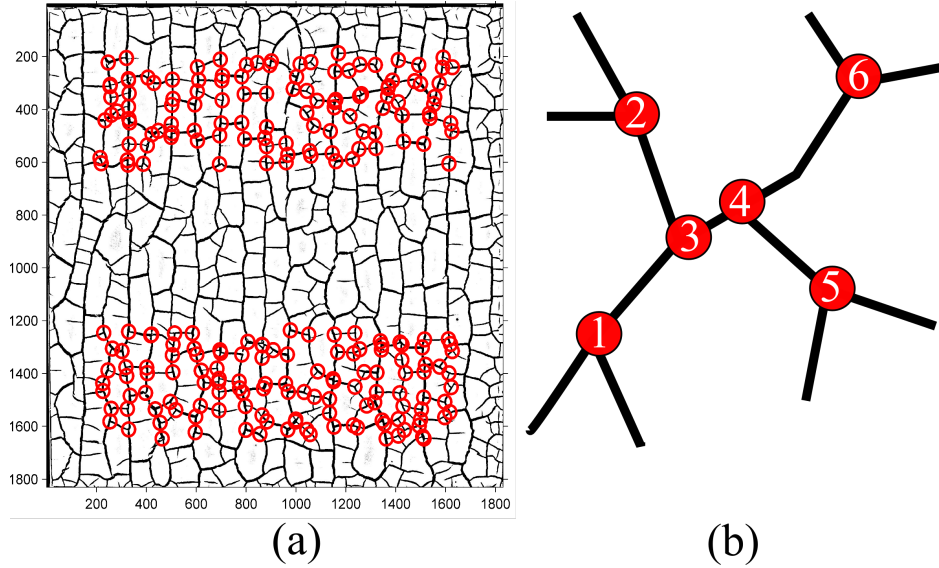
Figure 3.8: Definition of the Manhattan metric (a) shows the crack intersection points sorted according to their location. A crack intersection point from the top 1/3 of the image and a crack intersection point from the bottom 1/3 are paired and the ratio of the Euclidean distance and Manhattan distance $s_{Man}$ is calculated. This is done for all pairs of crack intersection points in figure (a). Some of the points are missing from the top and the bottom since 10% of points from each edge are ignored to prevent boundary effects. (b) is an example of a connected set of points. The connections of figure (b) are represented in the adjacency matrix equation 3.18.

## 3.5 Minkowski parameters

The Minkowski parameters are useful to describe spatial structures as they provide a global measure of an spatial pattern by taking into account geometrical and topological information. The three Minkowski parameters in two dimensions are the area $A$ boundary length $U$ and the Euler number $E$. They are calculated in the the following manner -

- First, all crack intersection points are detected in a crack pattern and stored.

- Circles of radius 5 pixels are centred on each crack intersection point. These circles can be generated by two methods. One involves plotting the crack intersection points in separate image as single pixels. Then a disk is used as a structuring element to erode the image. A second method, which is more efficient involves drawing circles around each crack intersection point then converting them to masks. figure 3.9 was generated using the second method.

- Images like the one presented in figure 3.9 (a) are generated for various values of radius. Following this, the Minkowski parameters are measured and stored for each radius value.
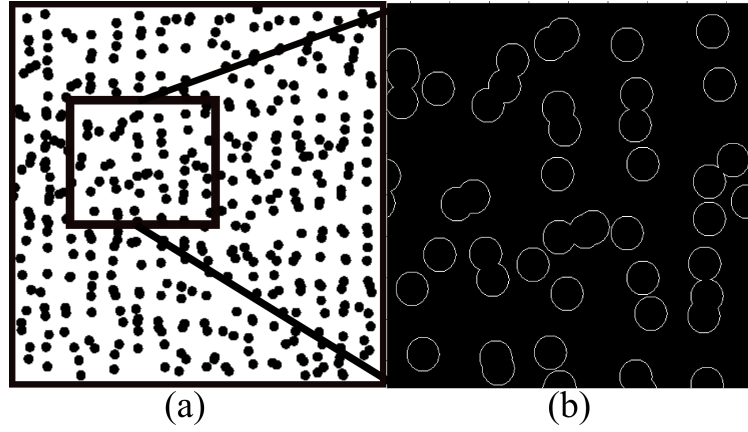
(a)                    (b)

Figure 3.9: Figure (a) is a binary image with circles centered at crack intersection points. This image is a snapshot of the code where for increasing radius, the existing circles are replaced with circles of larger radius. In this snapshot image, the measurement of Minkowski parameters are carried out. The sum of all the black pixels in the image is the total area which is normalized by total number of pixels in the image. Figure (b) shows the boundary pixels for a subset of objects in figure (a).

The Minkowski parameters are calculated using the following equations

$$A = \frac{n\,(\mathcal{B})}{n\,(\mathcal{P})}$$
$$U = \frac{n\,(\mathcal{U})}{n\,(\mathcal{P})} \tag{3.19}$$
$$E = N_{objects} - N_{holes}$$

where $\mathcal{B}$ is the set of black pixels in an image and $n\,(\mathcal{B})$ is the total number of boundary pixels in the image. $\mathcal{U}$ is the set of boundary pixels and $n\,(\mathcal{U})$ is the total number of black pixels in the image. $\mathcal{P}$ is the the collection of all the pixels and $n\,(\mathcal{P})$ is the total number pixels in the image. $N_{Objects}$ are the number of objects in the image. The number of objects and number of holes are defined with respect to foreground and background pixels. MATLAB recognizes objects as a connected regions which has a pixel value of 1, holes as connected regions with a pixel value of 0.

Figure 3.10 shows three plots of Minkowski parameters with increasing radius for the crack pattern in figure 3.9  (a). Figure 3.10 (a) shows the change in the total area of the image occupied by the disks with increasing radius. In figure 3.10 (a) the increase in total area is steep. At approximately 60 pixels radius, disks start overlapping which reduces the rate of increase in area. Figure 3.10 (b) shows the total number of boundary pixels (normalized by the area) with respect to increasing radius. For non overlapping discs the total number of boundary pixels increases with increasing radius. As the disks overlap, the $U$ quickly falls to zeros. As the disks overlap, regions two regions are formed. The first region is formed by the black overlapping disks, is the background and the second region is formed by the trapped foreground regions within the background region. Increasing the radius causes $A$ to increase since the foreground shrinks. However, the same effect causes the total number of boundary

pixels to decrease dramatically, because the number of holes keeps decreasing. The peak in figure 3.10 (b) represents a region with the largest number of boundary pixels. Beyond this limit, the disks overlap and the foreground regions start shrinking. At approximately $r = 80$ pixels, the image contains a single large background object. This behaviour is confirmed by the change in Euler number in figure 3.10 (c) where the number of isolated foreground regions, which are the number of objects keeps increasing, until they reach a maximum. Beyond this point a single region is created which is reflected in the drop of the euler number to 0.

## 3.6 Crack spacing

The crack spacing for a crack pattern is calculated using two different methods: one method involves, dropping randomly generated lines onto a crack pattern, and measuring the distance between two crack intersections. The second method involves calculating the crack spacing using the crack regions. The area of individual cracked regions is calculated and the side length of the square is used as the crack spacing.

### 3.6.1 Crack spacing using line dropping

The crack spacing algorithm is adapted from [38]. In order to calculate the crack spacing, random lines are constructed by generating a single point on the line and the orientation of the line. These lines are then placed on a skeleton image. It is important to to note that the crack spacing will differ based on the what type of image is used. The skeleton image is ideal to ensure that every single crack is captured. Once a line has been placed on the image, the intersections between the line and crack pattern are calculated. These intersection points are marked, then the distance between each intersection point is calculated, this value represents the crack spacing. This procedure is carried out for many lines. Here, the number of dropped lines is fixed at 1000 lines. The distances between intersecting points are calculated, and then a contraharmonic mean of the crack spacing is used to generate the average crack spacing for the crack pattern.

### 3.6.2 Crack spacing using cracked region

A second method to calculate crack spacing is to treat the areas of cracked regions as the areas of squares and use to the length of the sides of these squares as a measure of separation. The algorithm to detect cracked regions has been previously described and it is used to find the order parameter $S_{\mathrm{Ort}}$ in the section 3.2. This algorithm can be modified to output the area of a cracked region $A$. The side of a square with equivalent area $A$ is calculated. The side of the square is converted from pixels to centimetres by multiplying it by the ratio $20 \mathrm{~cm}/\sqrt{A_{\mathrm{Image}}}$ where $A_{\mathrm{Image}}$ is the area of the image.
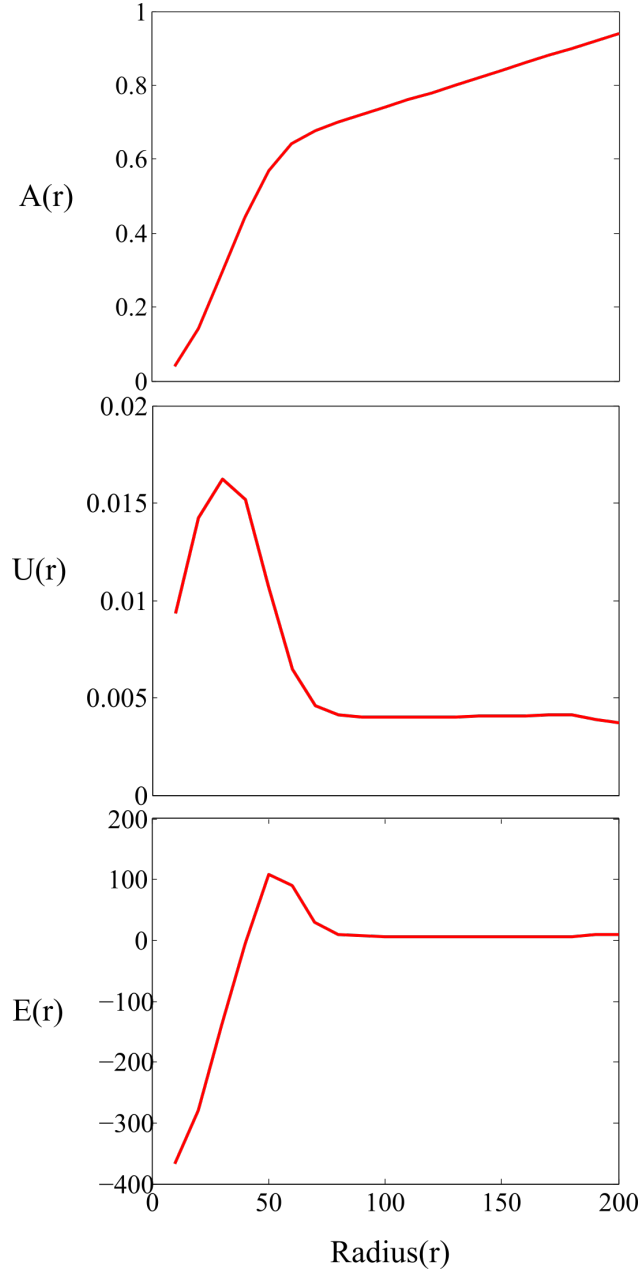
Figure 3.10: Figure (a-c) present the plot of all three Minkowski parameters- the area of the object $A(r)$, the boundaries of the object $U(r)$ and the Euler number $E(r)$. The Minkowski parameters are plotted against increasing radius in increments of 5 pixels. Figure (a) shows that as the radius increases there is transition at approximately 75 pixels. In case of $U(r)$ and $E(r)$ there are peaks at approximately 50 pixels. Such peaks and transitions are seen for all crack patterns. The interpretation of these behaviour will be presented in the next chapter.
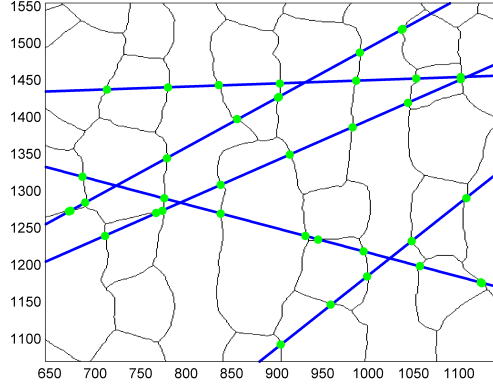
Figure 3.11: A snapshot the line dropping algorithm. The green dots are the intersections of the line with the crack pattern. The line dropping code is best used with a skeleton image. This is to ensure better intersection between the crack pattern skeleton and dropped lines. For all crack patterns 1000 lines are dropped to measure the crack pattern.

## 3.7 Fourier method to analyse crack patterns

The evenly spaced primary cracks in a ladder -like crack pattern and the periodic structure of the substrate suggests the application of Fourier methods to quantify the crack pattern.

To use Fourier methods, the crack density must first be calculated. The Fourier transform of the crack density would then allow determination of number of cracks per wavelength of the substrate.

The crack density is calculated by summing all the black pixels in the direction parallel to the peaks and plotting them along the direction perpendicular to the peaks. Take the example of figure 3.12 (a), the peaks are parallel to the $y$ direction, hence the black pixels which represent the cracks are summed along $y$ and are plotted against the $x$ direction. Hence in figure 3.12 (b), at a given value of $x$, the ordinate represents the total number of black pixels in the $y$ direction, normalized by the $y$ length of the image

$$C_d\,(x) = \frac{N_p\,(x)}{S_y} \tag{3.20}$$

where $S_y$ is $y$-size of the image, $B_N\,(x)$ is the number of black pixels in the $y$ direction and $C_d\,(x)$ is the normalized crack density. In figure 3.12 (b) the large peaks signify the primary cracks; the smaller peaks signify secondary and tertiary cracks.

The spectral power, which is given by the absolute value square of Fourier transform of $C_d$ is calculated and plotted against the wavenumber $\xi_x$, seen in  figure 3.12 (c). Spectral power serves to distinguish between the ladder-like crack patterns, which are periodic, and the wavy and isotropic patterns, which are non periodic. For a ladder-like crack pattern, since the cracks align with the substrates, there are sharp peaks where the wave number $\xi_x$ of the crack pattern is an integer multiple of the wavelength $\lambda$ of the substrate. It serves to plot the spectral power with respect to the relative wavenumber $\xi_x\lambda$, where $\xi_x\lambda = 1$ signifies a crack on top of the peak of the substrate, $\xi_x\lambda = 2$ signifies a crack atop the peak and a crack in the trough of the substrate and so on.

In the next chapter, the above Fourier methods are applied to all layer height for all sinusoidal plates with an amplitude to wavelength ratio of 0.25 and 0.5. The relationship between the layer height and number of cracks per wavelength is elucidated.

## Summary

This chapter presented various methods that will be used to analyse crack patterns in the next chapter. An attempt has been made to provide a step by step description of the algorithms that were used to study the crack patterns.

Section 3.1 shows how to calculate the angle distribution for the angles that form between neighbouring cracks and the vertical direction. The order parameter $S_{Angles}$ is constructed by multiplying the angle distribution $P(\theta)$ by $\cos 4\theta$. It is shown that $S_{Angles}$ falls between 1 and -1, where $S_{Angles} = 1$ indicates cracks that are parallel to the peaks of the substrate, $S_{Angles} = 0$ that there is no preference in direction and $S_{Angles} = -1$ that they are at either $45°$ or $135°$ to the substrate. A complement to the crack angle distribution is the distribution of angles acquired by detecting the orientation of individual cracks. These two methods are compared and for the same crack pattern it is shown that the values acquired for $S_{Angles}$ are similar. It must be stressed that such a comparison in no ways proves that these two methods are equivalent, and as will be shown with the data in the next chapter, there are differences between the two methods.

In the second section, the method to calculate the orientation of cracked regions is described. This method involves isolating cracked regions and calculating their second moment which is used to evaluate equation 3.7 from which the angle of the cracked region can be calculated. The orientation of all cracked regions in a crack pattern is calculated and averaged to yield $S_{Ort}$ which lies between 1 and -1. $S_{Ort} = 1$ represents a crack pattern where the major axis of the elliptical fits to the majority of the cracked regions lie parallel to a curve that lies atop the peaks of the sinusoidal and radially sinusoidal plates. The methods developed in section 3.2 are used to also calculate the orientation of individual cracks and also to isolate crack skeletons whose lengths are measured to acquire crack length distributions.

Apart from the crack angles parameter $S_{Angles}$ and the orientation of crack regions $S_{Ort}$, two other measures of the crack pattern are presented, these are Manhattan metric and the Minkowski parameters. Both these are global measures of a crack pattern. The Manhattan metric is used to defined the parameter $S_{Man}$ which is the ratio of the Euclidean distance travelled and the Manhattan distance travelled between two crack intersection points. $S_{Man}$ is calculated for pairs of crack intersection points where each element of the pair is picked from top and bottom of the image. The mean value of $S_{Man}$ yields the parameter $S_{Man}$ which is equal to 1 for crack patterns where there are crack going in the y-direction i.e parallel to the peaks of the substrate. The three Minkowski parameters which are used to compare spatial patterns are described in the context of crack patterns. These three Minkowski parameters are the area $A(r)$, the $U(r)$ of the disks which have origins at crack intersection points and the $E(r)$ which is number of objects subtracted by the number of holes.
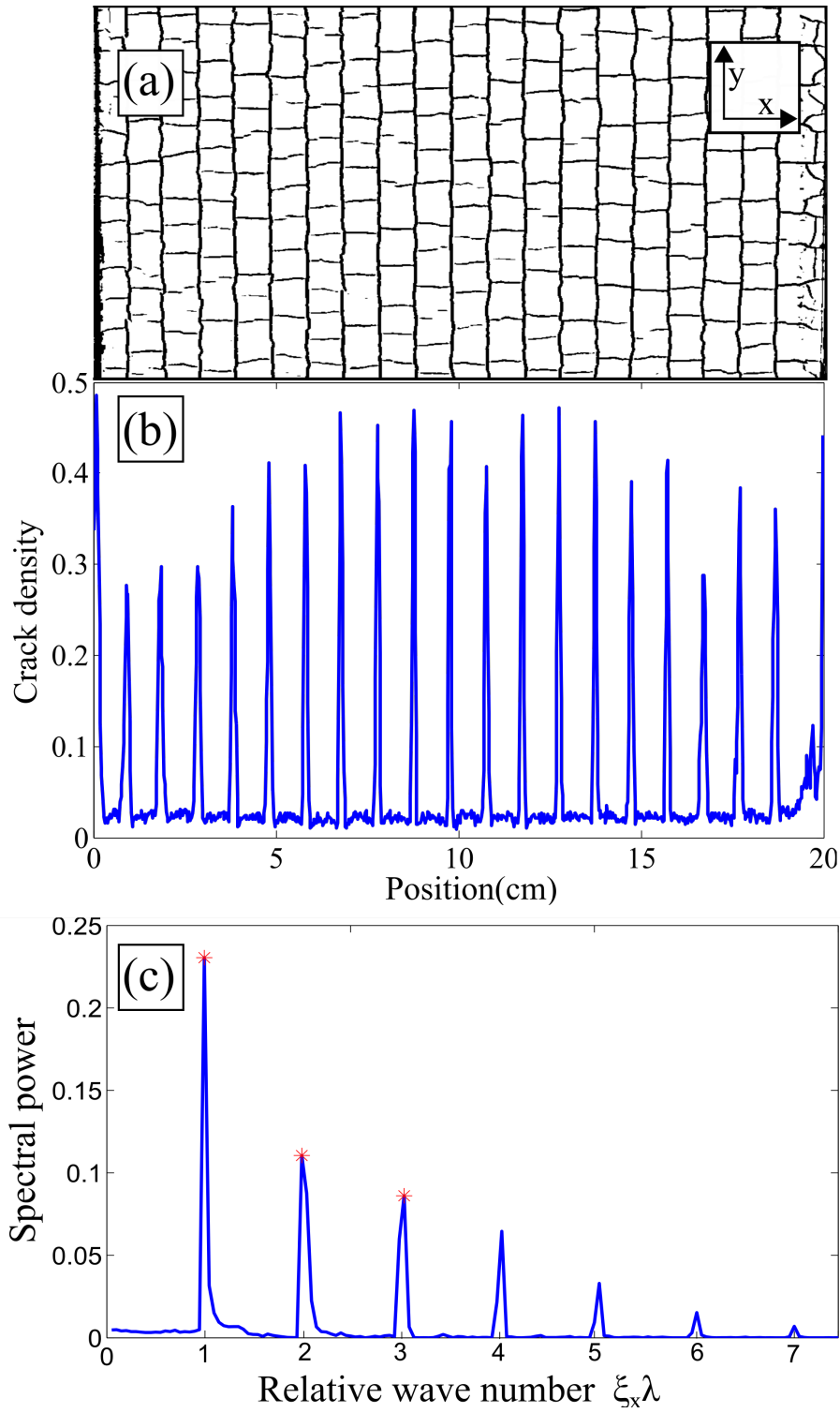
Figure 3.12: (a) is a crack pattern at $h = 0.29$. (b) is a plot where the ordinate is the x position (in pixels) of the image. The range of the plot is the total number of black pixels per x position. (c) Fourier transform of figure 3.12 (a). The spatial frequency here represents the number of wavelengths in a 20 cm plate where the base wavenumber is $\xi = 20$ i.e there are 20 wavelengths within the dimensions of the substrate. The red stars represent the base, the second and the third multiples of the spatial frequency of the substrate's oscillations.

There are two methods presented in order to calculate the crack spacing of a crack pattern, one involves using the line dropping algorithm another involves calculating the sides of a

square with the same area as the area of a cracked regions. In the next chapter, both these will be compared to see which, if any, is sensitive to the effect on the substrate.

The chapter closes by describing methods which use Fourier transforms to quantify the number of cracks per wavelength. The crack density for a sample image is calculated, which in turn is used to calculate the spectral power. The spectral power is plotted against the wave-number and it is observed that peaks occur at multiples of wave-number 20 for the sample image.

In the next chapter, the above methods will be applied to crack patterns over a range of increasing layer heights and the change in the order parameters, the crack spacing and other methods shown in figure 3.1 will be presented and discussed. One important aspect that has not been mentioned in this chapter, and is the opening section of the next chapter, is the time evolution of the order parameters. Since time lapse images of each crack pattern were taken, the order parameters are measured over a range of time points and are plotted to check whether they converge to a single value. This is also an essential check to ensure that the crack pattern is mature and the fluctuations, if any, in the order parameters are minimal.

# Chapter 4

# Results

This chapter presents the results obtained by applying the methods of crack pattern analysis which were discussed in the previous chapter.

- This chapter opens by classifying experimentally observed crack patterns as either wavy, ladder-like or isotropic. The resulting classification is plotted for each dimensionless layer height, it allows for comparisons with the data acquired from crack pattern quantification. It is a guide to the types of crack patterns found at each layer height.

- The second section deals with the time evolution of $S_{Angles}$ . This example is presented to show that the crack patterns which are measured are mature crack patterns. It is necessary to ensure this condition because, for example, $S_{Ort}$ is sensitive to the area of the cracked region, which will change over time if the crack pattern is not mature. In case of $S_{Angles}$ and $C_{Ort}$ , if further connections in the crack patterns are formed between cracks, this can alter the over all angle distribution, although the effect will be small.

- The third section deals with the results of calculating the power of the Fourier transform of the crack density. The Fourier methods are applied only to the sinusoidal plate. The Fourier methods show that beyond a certain $h = H/\lambda$ value, the spectral power of the crack density falls to zero. The data for individual plates are individually discussed in the next chapter.

- The fourth section combine the application of the three parameters $S_{Angles}$ , $C_{Ort}$ and $S_{Ort}$ to crack patterns and shows the subsequent result.

- The fifth section presents the data for the crack spacing over all layer heights. The crack spacing over a flat plate is compared with the results for the sinusoidal plates. The crack spacing of all but the radially sinusoidal plates are shown.

- The final section presents the measurements of the crack lengths. The idea is to explore if there are changes in the length of a crack connecting two crack intersection points due to crack pattern transitions with increasing layer heights.

## 4.1 Observations of crack pattern transitions

In chapter 2, the procedure to generate crack patterns on an uneven substrate was described, some elementary observations about the different types crack patterns were mentioned as well. The control parameter for the experiments are- the amplitude of the substrate $A$, the wavelength of the substrate $\lambda$, and the layer height $H$. Variations of these three parameters are responsible for the observed transitions in the crack pattern. Figure 4.1 shows observational results based on the type of the crack pattern where crack patterns are classified as either wavy, ladder-like or isotropic. There observations are made by eye. Since the main control parameter in the experiments is the layer height, the amplitude to wavelength ratio is plotted against the layer height in figure 4.1. In figure 4.1, each point represents a crack pattern, and its type is determined purely by observation. The classification of the pattern helps in forming a hypothesis which can be tested against the measurements of the crack pattern.

The observations in figure 4.1 are made for plates 1-5. For $A/\lambda = 0.5$ no wavy cracks are observed, up till $h \approx 1$ ladder-like cracks are present. In the region $1 \leqslant h \leqslant 1.25$ some crack patterns seem to be isotropic, others are ladder-like. There were some crack patterns which were a combination of both ladder-like cracks and isotropic cracks. This classification was based on which pattern dominated the overall pattern. Beyond $h = 1.25$, all of crack patterns were isotropic. For $A/\lambda = 0.25$, all three types of crack patterns were observed. The overlap region between wavy cracks and ladder-like cracks is $0.35 \leqslant h \leqslant 0.5$, above this region ladder-like cracks are observed until a second region $0.75 \leqslant h \leqslant 1$ where the transition from ladder-like to isotropic cracks seems to occur. When $A/\lambda = 0.125$ the regions of transition between wavy to ladder-like to isotropic seem very sharp. This is primarily because there is only one plate with an $A/\lambda = 0.125$, plate 5. With all the other $A/\lambda$ ratios, due to multiple plates, a certain amount of ambiguity is there in deciding the type of crack pattern. For the same layer height, two plates with the same $A/\lambda$ ratio may have different type of crack patterns in transition regions described above.

There are two interesting questions which can be posed. What is the nature of the transition from ladder-like cracks to isotropic cracks? Observations by eye suggests that the ladder-like to isotropic transition is continuous. How can we check this? Furthermore, is it possible that beyond a certain layer height, only a single type of crack pattern can be found? These are questions that will be answered through quantification of the crack pattern. Quantification provides a means of checking how the crack pattern will evolve due to the changes in the control parameters.

## 4.2 Time evolution of parameters

Time evolution of the measurement parameter $S_{Angles}$ is studied to ensure that the crack pattern is mature before making a measurement. Figure 4.2 shows the time evolution of $S_{Angles}$ for the crack pattern shown in inset of the same figure. The blue dashed line represents the final value $S_{Angles} = 0.65 \pm 0.04$. The green lines represent error values. The error values
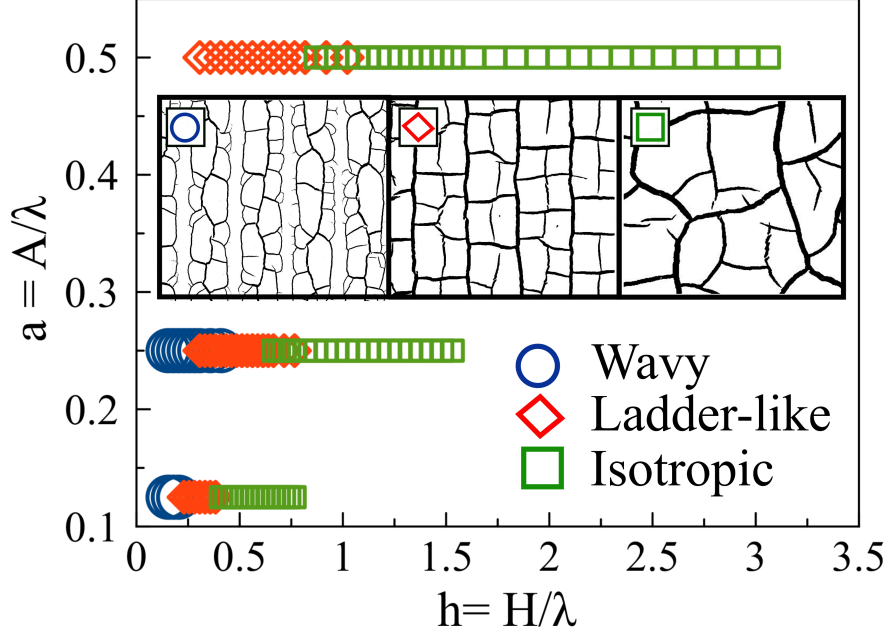
Figure 4.1: Crack pattern transitions due to change in control parameters. The crack patterns are sorted on the basis the amplitude to wavelength ratio a of the substrate. Based on observations, one of three types of crack patterns: wavy, ladder-like or isotropic are assigned to each crack pattern. For each amplitude to wavelength ratio, crack patterns are identified over increasing dimensionless layer height h. The inset images are examples of wavy (left most image), ladder-like crack pattern (second from left) and an isotropic crack pattern (right most image).

are acquired by segmenting the final image into 4 equal, non overlapping pieces and measuring $S_{Angles}$ values separately for each of them. These four values are averaged and used as error bars. This procedure is adopted to calculate the error for $S_{Ort}$ as well as $C_{Ort}$ parameters.

Up till approximately 2.5 hours the values of $S_{Angles}$ lie outside the regions defined by the error values. Above this, although the $S_{Angles}$ values fall within the error region, the values undergo significant variation. Beyond 4.5 h $S_{Angles}$ values stabilize. Hence a minimum of 4.5-5 hours are required for the crack pattern to truly mature, and for reasonable measurements to be made. In case of the radially sinusoidal substrate, where there is very little accelerated drying, it is even more important to let the bentonite slurry dry out for a long duration. To ensure that the crack pattern is mature, the slurries are dried over night. Details of the process are given in the materials and the methods chapter.

## 4.3   Fourier methods

In the previous chapter, Fourier methods were used on a single image to acquire the power spectrum. The power spectrum is used to differentiate between ladder-like like, wavy and isotropic cracks. This is possible since ladder-like cracks show periodicity which is absent in wavy cracks and ladder like cracks. Spectral power is calculated by first computing the
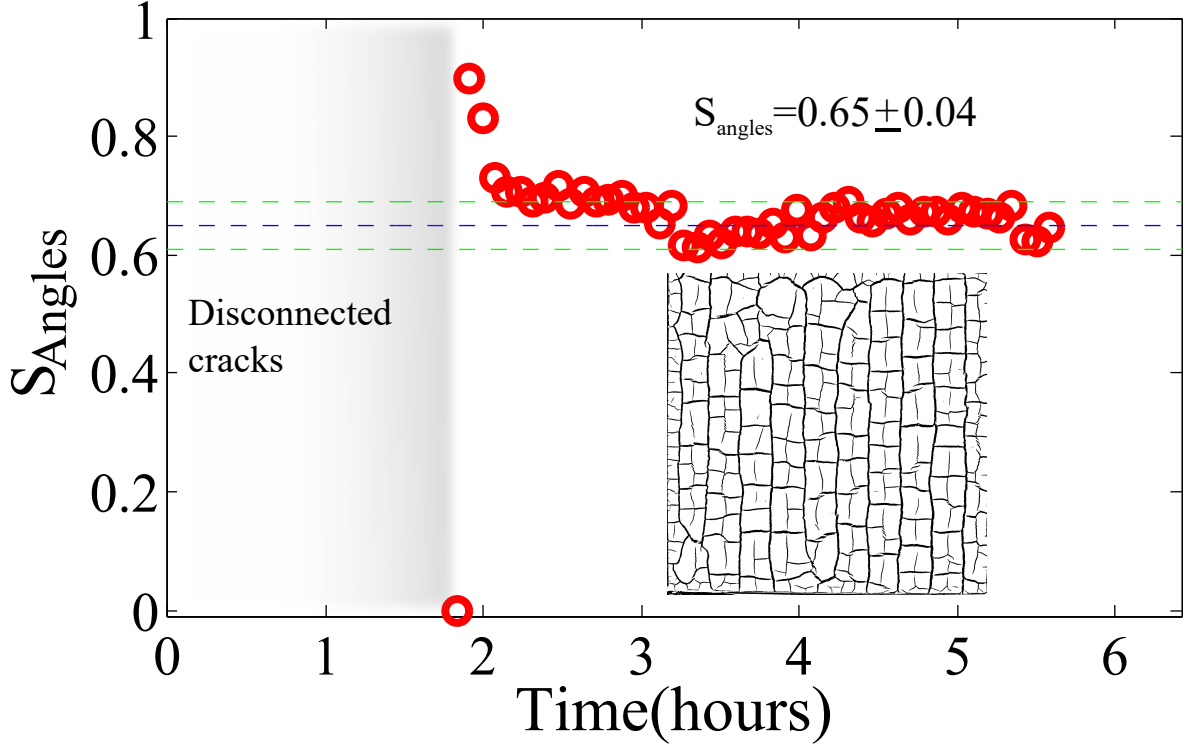
Figure 4.2: Time evolution of $S_{\text{Angles}}$ for a sample crack pattern. The final value of $S_{\text{Angles}} = 0.65 \pm 0.04$. The final crack pattern is shown in the figure inset. Below two hours it was observed that most of the cracks were unconnected. On average, it took a minimum of 4 hours under halogen lamps for bentonite slurries to dry before a mature crack pattern formed. To ensure the crack pattern was mature, a minimum of 6 hours is before taking the final image used in the analysis of crack patterns. In case of the radially sinusoidal plate, since the substrate was sensitive to high temperature, the slurry was left to dry over night at a minimum. For large layer heights, usually above $h \geq 2$, the slurry was dried for over two days to ensure that the crack pattern was mature.

Fourier transform $f\left(\xi_x\right)$ of the crack density $C_d\left(x\right)$ -

$$f\left(\xi_x\right) = \int\limits_{-\infty}^{\infty} C_d\left(x\right)e^{-i2\pi x}dx, \tag{4.1}$$

Here $\xi_x$ is the cycles per unit distance in the image, it is referred to as the wave-number. In order to ascertain which wave-numbers are dominant in the Fourier transform, the spectral power is calculated and normalized. The spectral power is given by -

$$P\left(\xi_x\right) = |f\left(\xi_x\right)|^2 \tag{4.2}$$

Three modes of the spectral power are used for all crack patterns $\xi_x\lambda = 1, 2, 4$. $\xi_x\lambda = 4$ is used to show that there is no signal at higher modes.

In figure 4.3 the spectral power is plotted against relative wave number $\xi_x\lambda$. The power approaches zero for all wave-numbers in figure 4.3 beyond $h = 0.75$, for figure 4.3 (a) and for $h = 1.5$ in figure 4.3 (b). Below this limit, non monotonic behaviour is observed for spectral
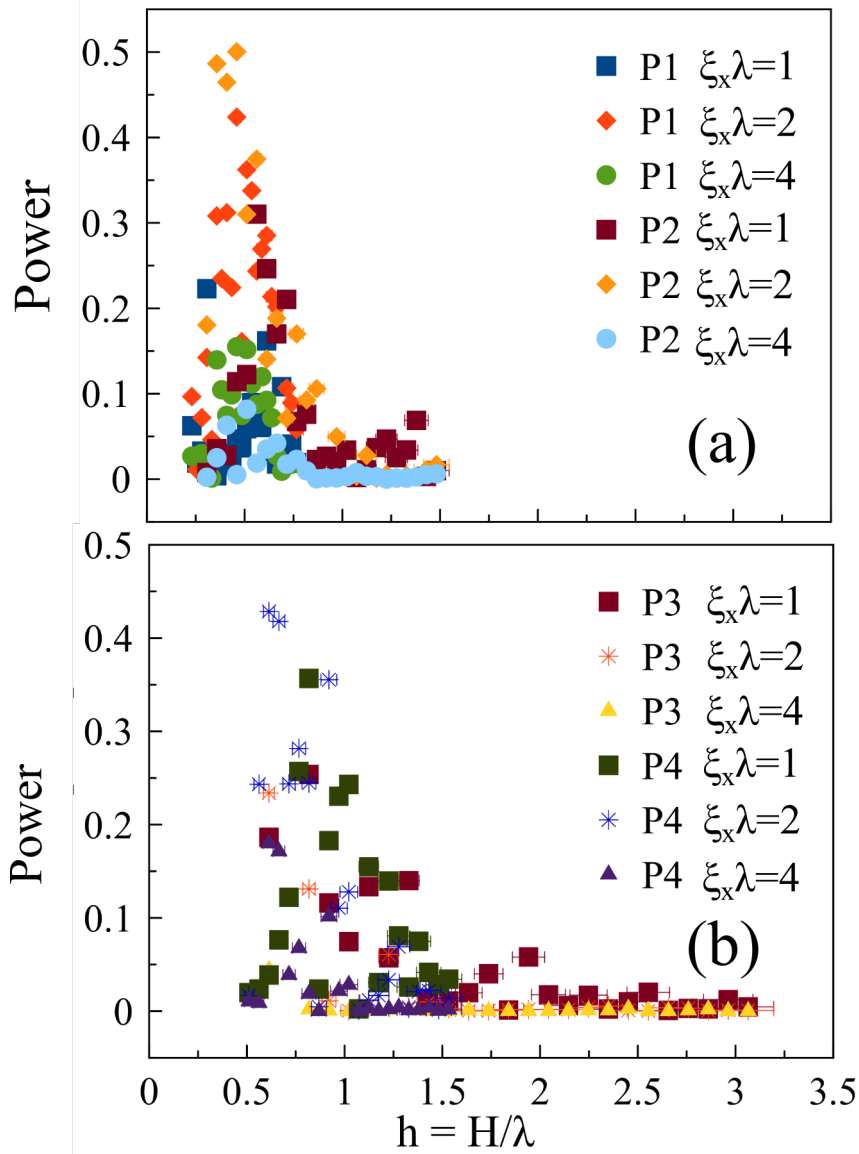
Figure 4.3: spectral power plotted vs dimensionless layer height $h$. (a) Is for $A/\lambda = 0.25$ and (b) for $A/\lambda = 0.5$. The spectral power is plotted at three value of wavelengths - $\xi_x\lambda = 1, \xi_x\lambda = 2, \xi_x\lambda = 4$. $\xi_x\lambda = 1$ corresponds to one crack atop every peak. In (a), the normalized power signal approaches zero for h > 0.75 and in figure (b) for h > 1.5. Below these limits, the normalized power behaves non monotonically.

power. In the region of non monotonic behaviour, the spectral power is highest for $\xi_x\lambda = 2$ and lowest for $\xi_x\lambda = 4$.

From the data it is clear that beyond $h = 0.75$ for figure 4.3 (a) and $h = 1.5$ for figure 4.3 (b) there is very little power in any of the measured wave numbers. At these layers most of the observed crack patterns are isotropic. These results will be discussed further in section 5.1

## 4.4   Measurement parameters

In this section, measurement parameters are applied to crack patterns on plates 1-4, and radial plates 1 and 2. They are plotted against dimensionless layer height $h$. The measurement parameters plotted are-

- Angle distribution of cracks $S_{Angles}$      Section 3.1

- Orientation of individual cracks $C_{Ort}$      Section 3.3

- Orientation of cracked regions $S_{Ort}$      Section 3.2

- The Manhattan metric type parameter $S_{Man}$      Section 3.4

### 4.4.1   Crack angles

$S_{Angles}$ is a parameter based on the angle distribution of crack angles, and applied to crack patterns generated over variety of substrates. The angle between cracks and a unit vector, defined by the substrate symmetry, are measured, processed and plotted against increasing dimensionless layer height $h$ in figure 4.4. For the sinusoidal plate, the angles are measured between a vector $\vec{r}_{ij}$ and $\hat{x}$ where $\vec{r}_{ij}$ is the vector that connects the $i^{th}$ crack intersection point with its $j^{th}$ neighbour and $\hat{x}$ is a unit vector that lies perpendicular to the substrate peaks. In case of radially sinusoidal plates, the definition of $\vec{r}_{ij}$ remain the same, while the unit vector becomes $\hat{r}_i$ which connects the center of the image to the $i^{th}$ intersection point. The measured angles are plotted as an angle distribution and using equation 3.5 to acquire the parameter $S_{Angles}$ .

$S_{Angles}$ reduces the information about the crack pattern to a single number which lies in between 1, that represents a crack pattern where the cracks are parallel and perpendicular to the substrate, and -1, where the cracks lie at $45°$ and $135°$ with respect to the substrate. When $S_{Angles} = 0$, the cracks have no preferential direction.

The parameter $S_{Angles}$ is found for all crack patterns generated over plates 1-4 and radial plates 1 and 2. In figure 4.4 two figures, one for $A/\lambda = 0.25$  (figure 4.4) (a) and $A/\lambda = 0.5$ (figure 4.4) (b) show how $S_{Angles}$ changes with increasing dimensionless layer height. The figure 4.4 (a) shows the data for all three plates- plate 1, plate 2 and radial plate 2. The maximum dimensionless layer height value vary, since plate 1 has a higher wavelength ($\lambda=2$) than plate 2 and radial plate 2. The values of $S_{Angles}$ for all three plates vary between an upper limit of approximately 0.9 and a lower limit of -0.2. At low $h$ values, reasonable data collapse is observed for all three plates where a maximum in $S_{Angles}$ value occurs at
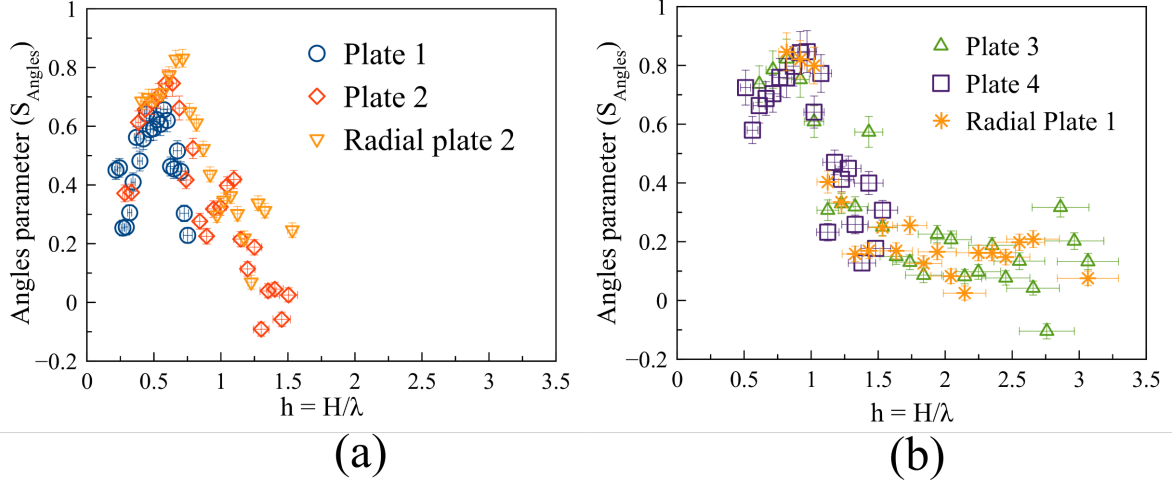
Figure 4.4: Evolution of the parameter $S_{Angles}$ with increasing layer height. (a) contains the data for $A/\lambda = 0.25$ and figure (b) for $A/\lambda = 0.5$. In both figures reasonable data collapse is observed for all plates in each figure. In Figure (a), for low layer heights, $S_{Angles}$ is small. With increasing $h$, a peak in $S_{Angles}$ occurs at $h \approx 0.5$. The magnitude of this peak differs for all three plates. Values of $S_{Angles}$ over $h \geq 0.5$ decreases for all plates. In (b), a similar trend to figure (a) can be seen in the region $0.5 \leq h \leq 1.5$ where a peak in the data occurs at $h \approx 1.0$ for both plates 3 and 4. No noticeable peak in the data occurs for radial plate 1 in this region of $h$ values. Values of $S_{Angles}$ in the region $h \geq 1.5$ remains close to $S_{Angles} \approx 0.1$ with large scatter in values for large layer heights.

$h \approx 0.6$. The maximum value is not the same for all three plates, for plate 1, the maximum $S_{Angles}$ value is approximately 0.7, where as the maximum for plate 2 and the radial plate 2 are within close to each other. With increasing dimensionless layer height, $S_{Angles}$ decreases and for large values of dimensionless layer height, the scatter in the data is also also observed for large layer heights.

In case of the $A/\lambda = 0.5$ (figure 4.4 (b)) a larger range of dimensionless layer heights are explored with $h_{max} \simeq 3.0$. Similar to plate 1, due to a large wavelength ($\lambda = 1$), plate 4 goes upto $h_{max} \simeq 1.5$ whereas plate 3 and radial plate 1 go till $h_{max} \simeq 3.0$. The spread of $S_{Angles}$ values remains similar to what is observed in figure (a). The behaviour of $S_{Angles}$ in figure 4.4 (b) is, in principle, is also similar to figure (a) where a peak in $S_{Angles}$ is observed at $h \approx 1.0$.

$S_{Angles}$ measures the orientation of cracks with respect to the substrate. The data suggests that for a specific layer height, there is a peak in the $S_{Angles}$ values. This layer height depends on the $A/\lambda$ ratio. $C_{Ort}$ is another parameter that measures the orientation of cracks. In the next section the result of measuring $C_{Ort}$ are discussed.

### 4.4.2 Orientation of crack skeletons

The orientation of cracks $C_{Ort}$ with respect to the substrate is quantified by measuring the angle between the major axis of an elliptical fit to skeletons of individual cracks. Since $C_{Ort}$ and $S_{Angles}$ are defined in the same way, the range of values and their meaning is also
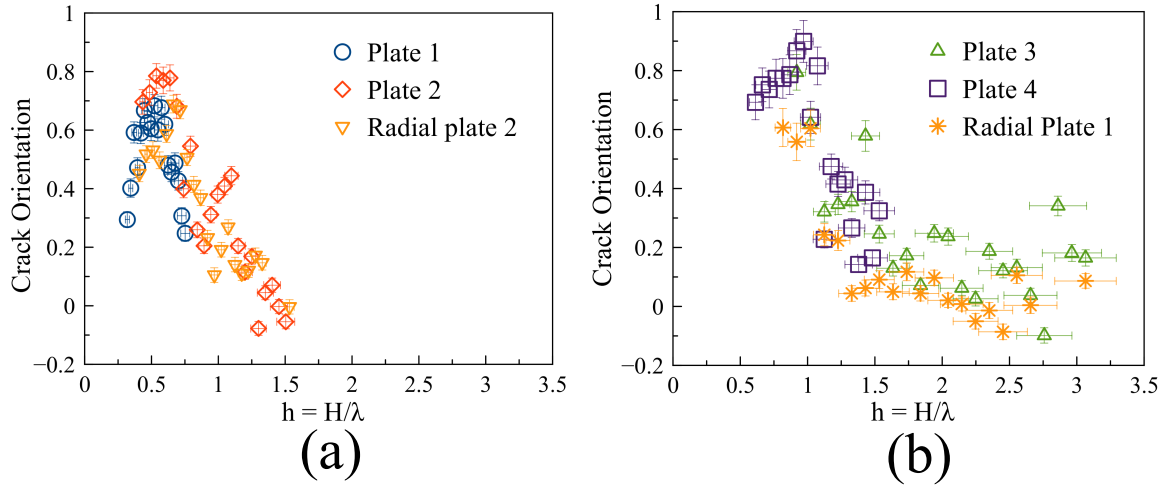
Figure 4.5: The change in the parameter $C_{Ort}$ with increasing layer height. Figure (a) contains the data for $A/\lambda = 0.25$ and figure (b) for $A/\lambda = 0.5$. The data in figure (a) has a peak in the data for all plates at $h \approx 0.5$. The highest value of $C_{Ort}$ is for radial plate 2. For $h \geq 0.5$ the values for $C_{Ort}$ decrease for all plates. The data in figure (b) has a peak at $h \approx 1.0$ for both plates 3 and 4. No peak is observed for radial plate 1. In the region where $1.0 \leq h \leq 1.53$ the parameter $C_{Ort}$ decreases and reaches a value $C_{Ort} \approx 0.1$. for $h \geq 1.5$ the values $C_{Ort}$ remain close to $C_{Ort} \approx 0.1$. Note. the results for $C_{Ort}$ are similar to the data presented in figure 4.4.

the same.

Figure 4.5 shows the data for both $A/\lambda$ ratios. In figure 4.5 (a), For plate 1, $C_{Ort}$ has a maximum value of $C_{Ort} \simeq 0.7$ at $h \simeq 0.52$. For plate 2, a peak in the data is observed at $h \simeq 0.53$ where $C_{Ort} \simeq 0.78$. The $C_{Ort}$ values for $0.53 \leqslant h \leqslant 1.5$ falls to below 0. The data for radial plate 2 has a peak at $h \simeq 0.66$ where $C_{Ort} \simeq 0.69$. In the range $0.66 \leqslant h \leqslant 1.52$ the data for plate 2 decreases and approaches 0.

The data for $A/\lambda = 0.5$ is presented in figure 4.5 (b) which contains data for plate 3,4 and radial plate 1. In this figure dimensionless layer height values range from $0.61 \leqslant h \leqslant 3.0$. Plate 3 decays monotonically starting at its maximum value of $C_{Ort} \simeq 0.79$ at $h \simeq 0.92$ and decreasing rapidly till $C_{Ort}$ reaches close to 0 at $h \approx 1.7$. Above this layer height, the value of $C_{Ort}$ settles around $C_{Ort} \approx 0.1$ and fluctuates. This behaviour is also seen in the data for the radial plate 1 where in region between $0.81 \leq h \leq 1.53$ $C_{Ort}$ falls to 0.1 and fluctuates around this value.

### 4.4.3 Orientation of cracked regions

Cracked regions form because regions of the cracking material are isolated due to formation of the crack pattern and the geometry of these regions is dependent on the type of crack pattern. $S_{Ort}$ measures the orientation of these cracked regions using the methods described in section 3.2. $S_{Ort}$ is acquired for all plates 1-4 and for radial plates 1 and 2. $S_{Ort}$ takes values between 1 to -1 where $S_{Ort} = 1$ represents a state where all the cracked regions lie parallel to the peaks of the substrate. $S_{Ort} = -1$ represents a state where all the cracked
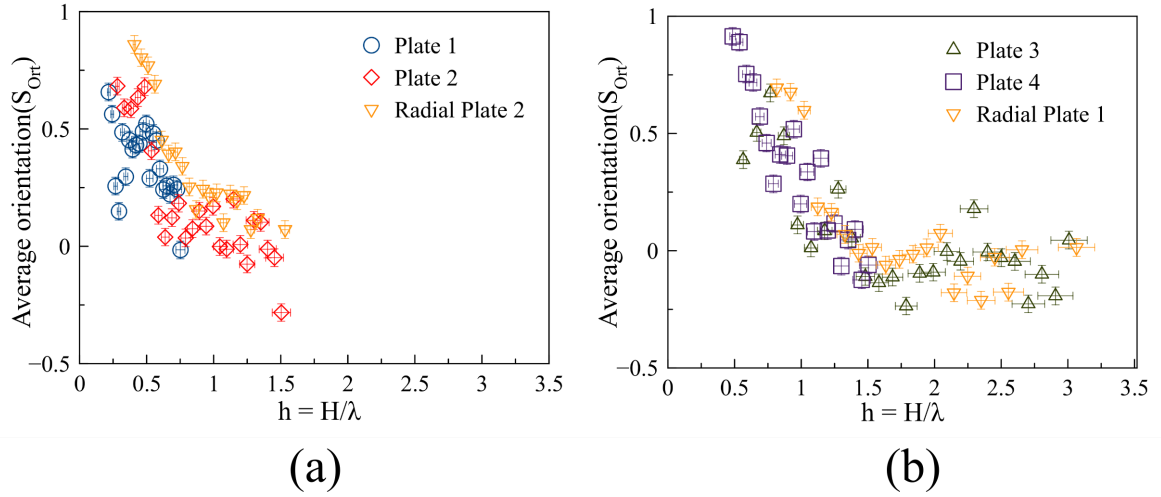
Figure 4.6: The parameter $S_{Ort}$ is plotted for both $A/\lambda = 0.25$ figure (a) and $A/\lambda = 0.5$ (figure (b)). In figure (a) a peak in the data of plate 1 and 2 occurs at approximately $h \simeq 0.5$, no peak is observed for radial plate 2, however the maximum value occurs at $h \simeq 0.5$ as well. For $h \geq 0.5$, values of $S_{Ort}$ keep decreasing. In figure (b) two regimes are observed, in the region $0.5 \leq h \leq 1.5$ the values for all plates decrease till $S_{Ort} \approx -0.1$. Above $h = 1.5$ remains unchanged with a large amount of scatter in the data.

regions lie perpendicular to the substrate. The data for $S_{Ort}$ values over all plates and $h$ values is shown in figure 4.6.

Similar to figure 4.4, two plots are presented in figure 4.6- figure (a) for $A/\lambda = 0.25$ and (b) for $A/\lambda = 0.5$. For all plates, the dimensionless layer height values are the same as figure 4.4. In figure 4.6 (a) the $S_{Ort}$ values range from a range of $-0.1 \simeq S_{Ort} \simeq 0.85$, with an outlier point at $S_{Ort} = -0.28$. For plate 1, $S_{Ort}$ drops for the first three points then increases again to a maximum value of $S_{Ort} \simeq 0.5$ at $h \simeq 0.4$. Plate 2 starts with a higher value compared to plate 1, however follows a similar trend. The maximum for plate 2 occurs at $h \simeq 0.5$ beyond which the $S_{Ort}$ decreases to values around zero. Radial plate 2 data follows a similar trend as that of plate 2 data, however in general is sightly higher than most of plate 2 $S_{Ort}$ values. No peak is observed, radial plate 2 data, the maximum value is the first point. The $S_{Ort}$ values for radial plate 2 do not suffer the same magnitude of scatter as the values for plate 2.

In figure 4.6 (b) the data for plates 3,4 and radial plate 1 are presented. The $S_{Ort}$ has a maximum of $S_{Ort} \simeq 0.91$ and a minimum of $S_{Ort} \simeq -0.22$. Plate 3 has a maximum at $h \approx 0.77$ with $S_{Ort} \simeq 0.67$, above $h = 0.77$ $S_{Ort}$ rapidly falls till $h \simeq 1.5$ beyond which $S_{Ort}$ fluctuates around $S_{Ort} \approx -0.1$. Unlike plate 3, radial plate 1 does not have a maximum, the first point is the highest value for the radial plate 1 which occurs at $h \simeq 0.81$ where $S_{Ort} \approx 0.7$. In region $0.81 \leqslant h \leqslant 1.5$ $S_{Ort}$ falls rapidly and beyond $h \approx 1.5$, $S_{Ort}$ follows a similar trend as plate 3. $S_{Ort}$ values for plate 4 start at $S_{Ort} \simeq 0.91$ and fall till $h \approx 1.5$ where $S_{Ort} \approx -0.07$, which lies in the same neighbourhood as the values for plate 3 and radial plate 1.
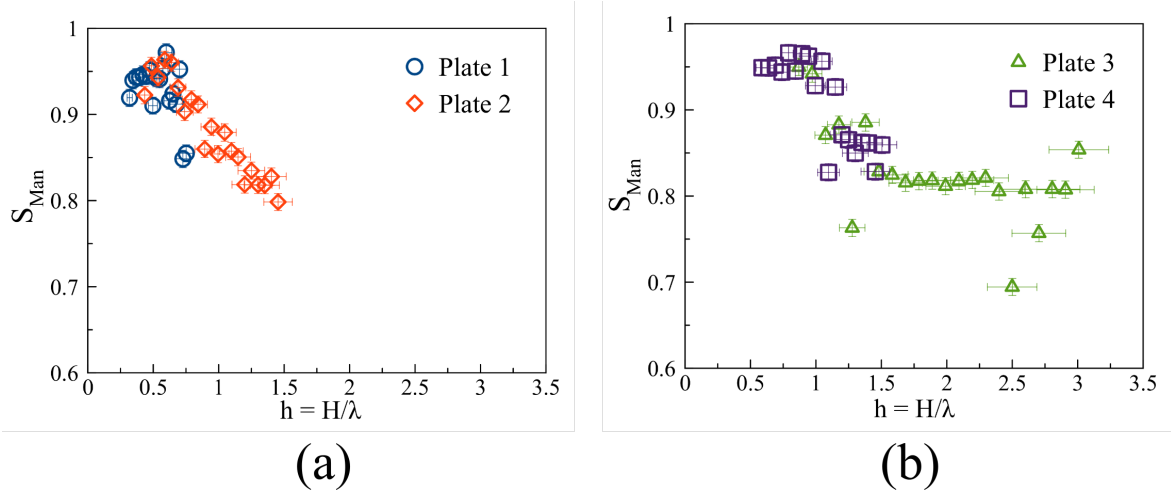
Figure 4.7: $S_{Man}$ for $A/\lambda = 0.25$ figure (a) and $A/\lambda = 0.5$ figure (b). Unlike earlier parameters $S_{Angles}$ and $C_{Ort}$ , there is no peak in the data at $h = 0.5$ in figure (a) and $h = 1.0$ (b). The values of $S_{Man}$ cluster around $S_{Man} = 0.96$ and decrease above $h > 0.5$. In figure (b), the data for plate 4 starts at a slightly lower value than its maximum which occurs at $h1.0$. Plate 3 does not have a peak, it monotonically decreases and then at approximately $h \approx 1.5$ remains fairly constant.

### 4.4.4 Manhattan metric approach

The parameter $S_{Man}$ uses a Manhattan metric type approach to quantify a crack pattern. The parameter $s_{man}$ is calculated for two crack intersection points by taking a ratio of the straight line distance to the distance along the crack network between the two points. This ratio of distances is calculated for all crack intersection points and averaged to yield $S_{Man}$ .

Figure 4.7 shows evolution of the parameter $S_{Man}$ over a range of layer heights for both $A/\lambda = 0.25$ and $A/\lambda = 0.5$. The smallest value that $S_{Man}$ can take is $S_{Man} = 1/\sqrt{2}$ and the maximum is 1. The minimum value of $S_{Man}$ corresponds to the ratio of distances between two non neighbouring points on a grid. $S_{Man}$ values vary from $0.79 \leqslant S_{Man} \leqslant 1.0$. For plate 1, the initial points have $S_{Man} \approx 0.95$. Neither plate 1 nor plate 2 have a peak near $h \approx 0.5$. The $S_{Man}$ values for plate 2 monotonically decay till the last $h$ value.

Figure 4.7 (b) contains the data for plate 3 and 4. The data for plate 4 starts at a high value $S_{Man} \approx 0.95$, for $h > 1$ values the data for plate 4 decreases. The plate 3 data collapses with the upper half of plate 4. Plate 3 decreases until $h \approx 1.5$ and levels off at $S_{Man} \approx 0.83$ with very little scatter until the last few data points. Out of all there points there is one large outlier which lies at $S_{Man} = 0.69$.

The values of $S_{Man}$ show reasonable data collapse, there is little scatter compared to the other parameters.

## 4.5 Crack spacing

The crack spacing is a parameter which captures the scale of the crack pattern. The attempt here is to see if the crack pattern transitions affect the crack spacing. The crack spacing is

measured using a line dropping algorithm. The algorithm involves plotting lines with random orientation onto the skeleton image of a crack pattern and measuring the spacing between crack intersections on these lines. The spacing between the intersections is measured and for each line, averaged over all lines  (see section 3.6.1).

The crack spacing is measured for plates 1-5 and for the flat plate. The results are shown in figure 4.8. The crack spacing is divided by the layer height for each data point, this is done to compare if the crack spacing is proportional to thickness of dried layer.

For the flat plate, at low layer heights, the ratio of crack spacing to layer height has a large value which reaches a minimum around 2, above a layer height of $H \approx 1.25$ cm. For rest of the plates, the crack spacing to layer height ratio for low layer heights is smaller than that of the flat plate. For plates 1,2 and 5, the behaviour of the ratio is similar to flat plate, starting at a large value they decay till a layer height of 0.75 cm beyond which they do not show any large scale variations. The ratio of crack spacing to layer height for plate 3 and 4 remains unchanged over the range of increasing layer heights. It is interesting to note that at large layer heights, the ratio of crack spacing and layer height does not approach values of the ratio of the same for the flat plate. For large H value, the crack spacing for the sinusoidal plates must approach that of flat plate.

Figure 4.9 shows the crack spacing acquired from the $\sqrt{A}$ where $A$ is the area of the cracked regions. The method is described in section 3.6.2. The crack spacing for the flat plate is lower than the spacing for the line dropping method. The spacing for the sinusoidal plates is similar to spacing calculated from the line dropping method.

## 4.6    Average crack length

Similar to crack spacing, the crack lengths are measured to see is crack pattern transitions influence the crack length. Since, with increasing layer height the crack spacing also increases, it can be expected that the length of the cracks that connect each crack intersection point in the crack pattern also increases. Since the crack spacing / layer height ratio approaches a constant value for large layer heights the question then becomes whether this also be true for the ratio of crack length/ layer height. Figure 4.10 shows the data for both A/$\lambda$ = 0.25 ( (a)) and A/$\lambda$ = 0.5  ( (b)).

In figure 4.10 (a), the length/layer height ratio for plate 1 remains close to 1 for the most part. For layer heights larger than 1.25 cm, the value of the ratio falls below 1 . For plate 2 and radial plate 2, the data starts at a higher value of length/layer height ratio and for large layer heights end at approximately 0.9. The data for plates 3,4 and radial plate 1 are presented in figure 4.10 (b). Here, too, the ratio crack length /layer height remains fairly constant and close to 1.

The ratio of crack length/layer height does not show any dramatic changes with increasing layer height. This result is similar to the result from the previous section where no variation in the crack spacing/ layer height is observed with increasing layer height.
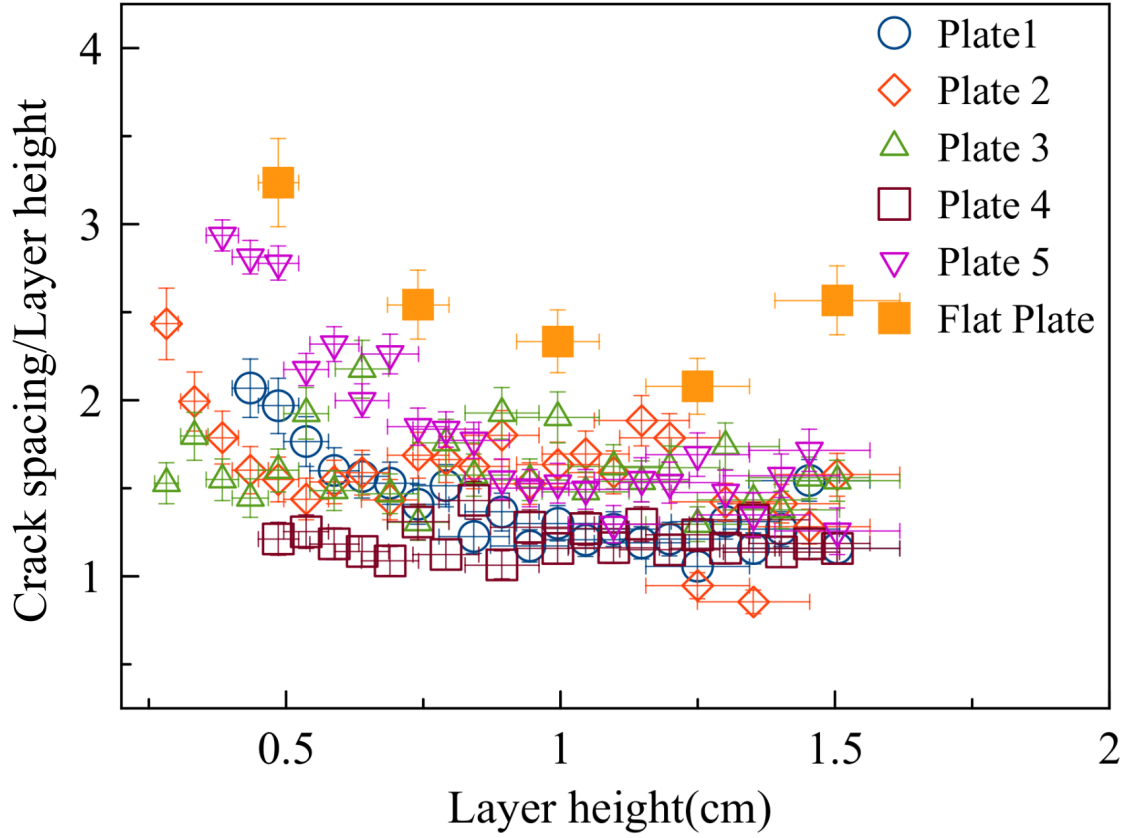
Figure 4.8: The ratio of crack spacing/layer height with increasing layer height. The figure contains the data for plates 1-5 and the flat plate. For the flat plate, all values of the ratio are higher than for the rest of the plates. At low layer heights, plates 1,2 and 5 follow a similar trend to the flat plate, they start with high values and decrease with increasing layer height. For large layer heights approximately above 1.25 cm, the ratio remains constant with small amount of scatter in the data. The value of the ratio remains essentially constant for plates 3 and 4.
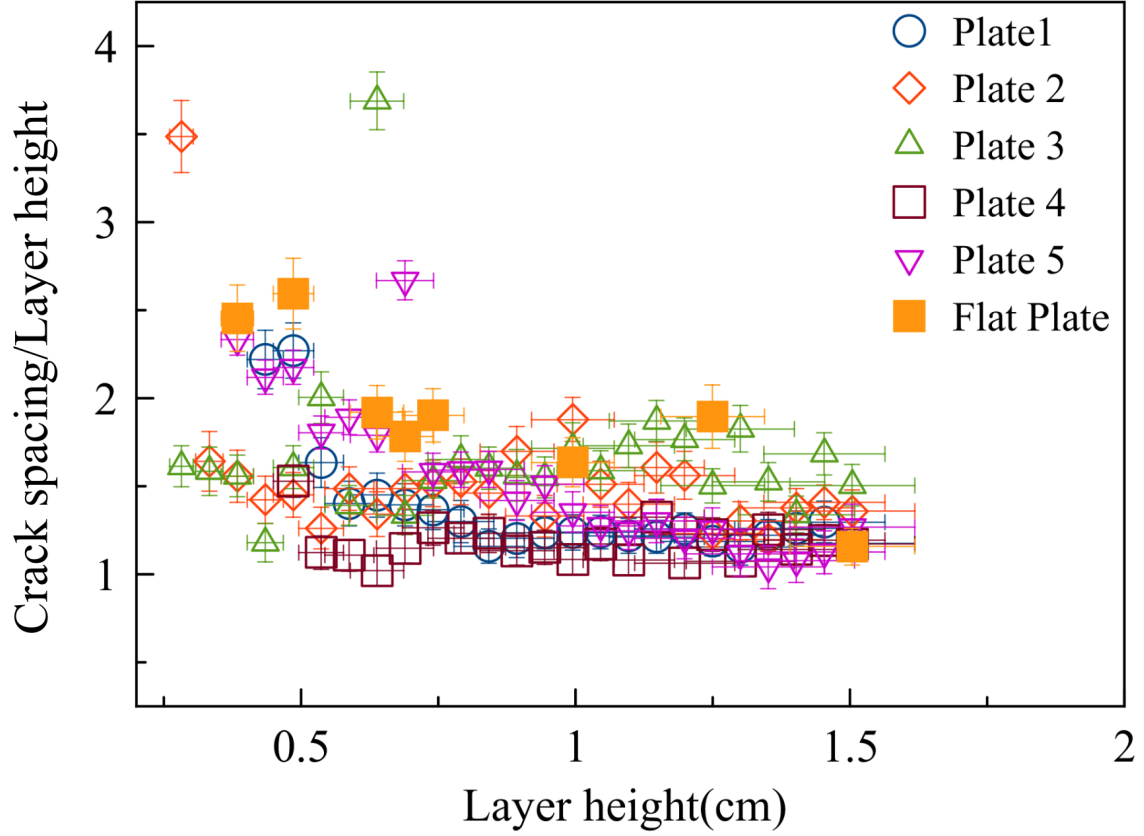
Figure 4.9: Crack spacing calculated using the $\sqrt{A}$ method for plates 1-5 and the flat plate. The crack spacing for the flat plate is slightly lower than the spacing calculated using the line dropping method. There is little other difference between the crack spacing acquired from the line dropping and $\sqrt{A}$ method.
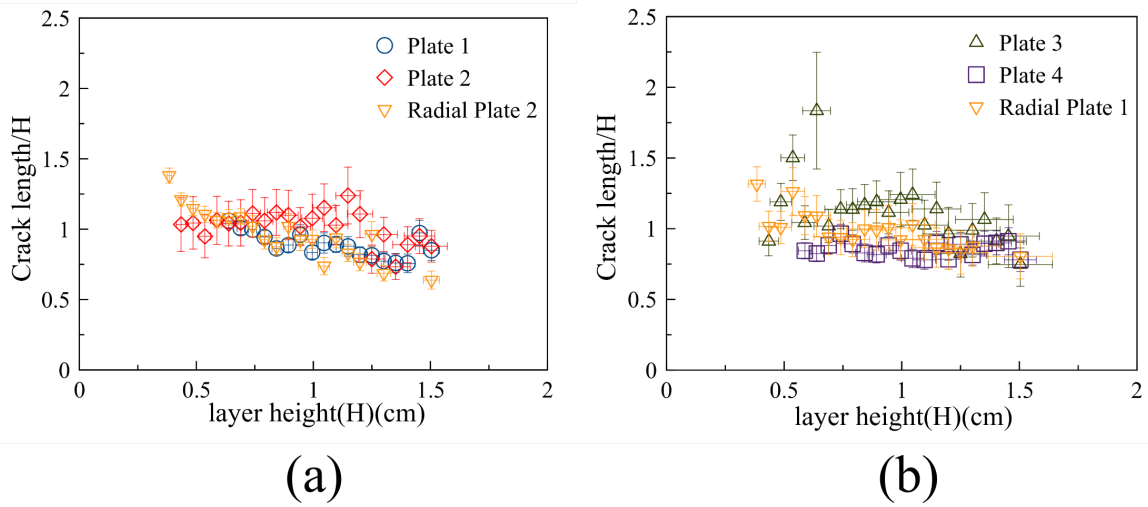


(a)



(b)

Figure 4.10: Figure (a) and (b) represent the change in crack length/$H$ for increasing layer height $H$. Figure (a) shows the data for A/$\lambda$ = 0.25 and figure (b) for A/$\lambda$ = 0.5. In both plots of figure 4.10 the ratio crack length / layer height remains close to 1 for all plates.

# Summary

Crack patterns were quantified in this chapter by applying the methods of crack pattern analysis developed in the previous chapter. Observations of crack pattern transitions were presented in figure 4.1 where each crack pattern was labeled to be either a wavy, ladder-like or isotropic crack pattern. It is essential to note that there is no necessity that a crack pattern must strictly follow such a classification. A crack pattern may contain regions where it is isotropic and regions where it is ladder-like, this assignment is merely a guide to the different regimes of the observed crack patterns.

The time evolution of $S_{Angles}$ is presented for a sample crack pattern generated on plate 1. This crack pattern is used as an example to justify the drying and waiting time before which the crack pattern is considered mature enough to be measured. In general a minimum of 4 hours must be waited before a crack pattern has dried enough to be measured. While the primary crack pattern forms fast, in less than 2.5- 3 hours, the finer cracks must make connections before the crack pattern reaches a stage where it will remain unchanged.

Fourier methods are applied to crack patterns and the power of the Fourier transform of the normalized crack density is acquired. Fourier methods are naturally suited for this problem due to the periodic nature of the crack patterns. They are applied for plates 1-4 for all layer heights. It is observed that above $h = 1.5$ no periodicity is seen any of the crack pattern. Below this limit, peaks at value dimensionless layer heights are observed, the highest of peaks are observed at around $h = 0.5$.

Section 4.4 presents the data for all the measurement parameters- $S_{Angles}$ , $C_{Ort}$ , $S_{Ort}$ and $S_{Man}$ . These parameters are calculated for all crack patterns generated on plates 1-4 and radial plates 1 and 2. It is observed that, for both $S_{Angles}$ and $C_{Ort}$ have similar data collapse. These parameters behave non monotonically for all dimensionless layer heights with peaks in the data at $h = 0.5$ for plates 1 and 2 which have an $A/\lambda = 0.25$ and for plates 3 and 4 at $h = 1.0$ with an $A/\lambda = 0.5$. It is observed that for plate 3, beyond $h = 1.5$ all three parameters show scatter in the data. However they level off close to a constant value in this regime.

The average crack spacing is measured using the line dropping method and presented for all layer heights and for all plates including plate 5. All the curves collapse except for the curve for the flat plate. This is true even for crack spacing at large layer heights. The crack spacing is also determined by a second method where the $\sqrt{A}$ is calculated plotted for all plates. Here, the flat plate crack spacing was lower than the values acquired from line dropping, the data for the sinusoidal plates were similar to data acquired from the line dropping method

The chapter ends with the data of crack length measurement over all layer heights. The data for all plates collapses and the the crack length/thickness ratio is close to 1. For a few plates like plate 4 this value is slightly less that 1. This suggests that the length of individual cracks is proportional to the layer height and is unaffected by the crack pattern transitions.

With this the quantification of the current experimental observation is completed, the next chapter tackles interprets the results. It expands further on the descriptions of each

measurement method presented in the previous chapter, and view them in the light of the experimental observations. This comparison addresses both questions of the central questions of the thesis which are - how are substrates influenced by crack patterns and how can crack patterns be quantified.

# Chapter 5

# Discussion

In the previous chapter, the data acquired from applying methods of crack pattern analysis were presented. The cartoon in figure 5.1 provides a general outline of the goals of this chapter. The first question to be addressed in this chapter is, how can the observations by eye (figure 4.1 be connected to the data obtained from measurement parameters. Does this data reflect the crack pattern transitions from wavy to ladder-like to isotropic? The second crucial question that is being answered is, how applicable are the methods to the current experimental system? Do all measures of provide similar information about a crack pattern, if not, how are they different? The third question addressed is, what are the strengths and the weaknesses of each method? There are limits of each method and they will break down under certain conditions. Furthermore, certain assumptions about crack patterns have been made in order to calculate each parameter, how these assumptions affect the measurements are discussed.

The first section of the chapter deals with analysing crack patterns using Fourier methods, combining the data acquired by calculating the power of crack density and the observations presented in 4.1. Certain conclusions are drawn about the relevance of the peaks observed in the data of figure 4.3.

The second section compares the flat plate crack spacing data with data obtained by Goehring et al.[36]. The crack spacing data for the sinusoidal plates is discussed in context of the pattern transitions observed in experiments, the lack of any change in the crack spacing due to these transitions is explored.

The third section recaps the data for the parameter $S_{Angles}$ and reconciles the non monotonic behaviour of $S_{Angles}$ with the crack pattern transitions observed in experiments. The significance of the substrates symmetry is briefly discussed. This discussion is applied to the parameter crack orientation $C_{Ort}$ and the measure of orientation of cracked regions $S_{Ort}$. The angle distribution for wavy, ladder-like and isotropic cracks are presented and briefly discussed. In addition to the data in chapter 4, figure 4.4, the flat plate limit is presented and its implications are discussed. This section also discusses the similarities between $S_{Angles}$ and $C_{Ort}$.

The fourth section of the chapter briefly discusses $S_{Ort}$ in context of crack transitions. It compares the difference between the parameters $S_{Angles}$ and $S_{Ort}$. This section also illustrates
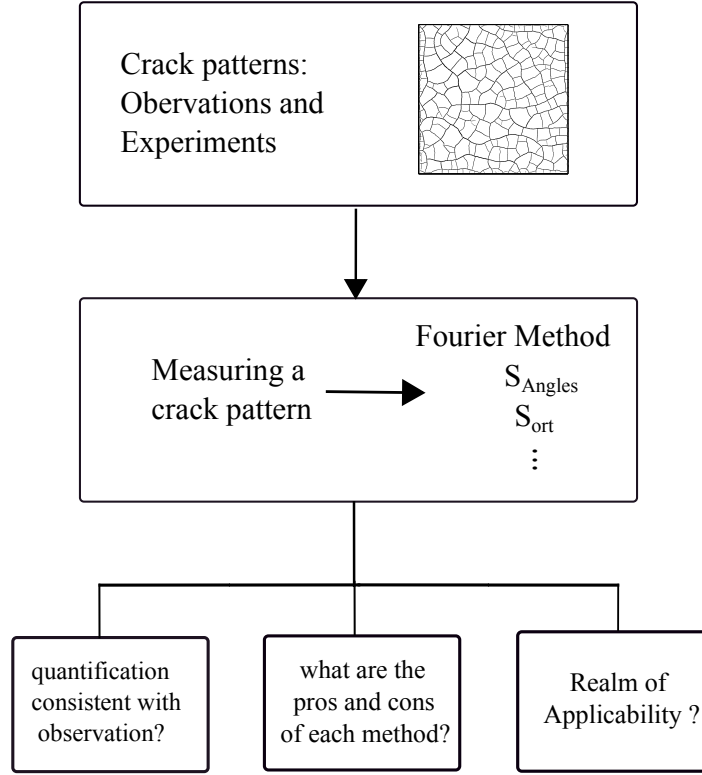
Figure 5.1: Goals of the chapter

the similarity between orientation of liquid crystals and orientation of cracked regions.

The final section highlights the results of applying the Manhattan metric method to crack patterns. The metric is a global parameter in contrast to $S_{Angles}$ and $S_{Ort}$ which are local measures of the crack pattern. The implication of this are discussed.

## 5.1 Crack pattern analysis using Fourier methods

The normalized power is one of the measures of a crack pattern. This measure provides a comparison between crack patterns by quantifying the periodicity of the pattern. Figure 5.2 shows the spectral power for $\xi_x \lambda = 2$ for plates 1 and 2. In figure 5.2, the power reaches a peak at $h = 0.5$ and then falls off to zero.

To better understand the data for power for non isotropic cracks, the power values for plate 2 are picked and plotted in figure 5.4.

Figure 5.4 shows the spectral power for plate 2 and suggests a transition from two cracks per wavelength to one crack per wavelength. In figure 5.4, three modes of the spectral power are plotted - $\xi_x \lambda = 1$, $\xi_x \lambda = 2$, $\xi_x \lambda = 4$. There is peak in the spectral power for $\xi_x \lambda = 2$ at $h \leqslant 0.4$ and a peak in the data for $\xi_x \lambda = 1$ for $h = 0.60$. Beyond this regime the spectral power falls to zero for all relative wavenumber. Three inset images are also shown in figure 5.4, two of the images show the crack pattern near the peaks of the two modes. The crack pattern corresponding to $\xi_x \lambda = 2$ has two cracks per wavelength, it contains mostly straight primary cracks with few wavy secondary cracks. The crack pattern corresponding to the peak at $h = 0.6$ contains a ladder-like crack pattern where there no secondary cracks

parallel to the primary cracks.

The data in figure 5.4 suggests that the maximum in spectral power for modes $\xi_x\lambda = 1, 2$ occurs for crack patterns that are most ladder-like. A ladder-like crack pattern is representative of the structure of the substrate. Before a ladder-like crack pattern is observed, a transition region exists for $0.4 \leq h \leq 0.6$. The lower end of the transition region tends to have two cracks per wavelength, where the primary cracks are aligned with the substrate. However the secondary cracks tend to either be perpendicular to the substrate or be wavy. These wavy cracks meander near the trough. Close to the higher end of the transition region the secondary cracks appear perpendicular to the substrate. At values close to $h = 0.6$, a ladder-like pattern is formed where the primary cracks are parallel and the secondary cracks are perpendicular to the substrate. There are thin tertiary cracks that appear parallel to the primary cracks as show in figure inset for $h = 0.6$ in figure 5.4.

In a crack pattern containing wavy cracks or an isotropic crack pattern, the spectral power is very small. Two examples to are presented here : the first one is the comparison of power vs $h$ for crack patterns generated on the same plate at different layer heights and a second example where the power for $\xi_x\lambda = 2$ is compared for two plates with the same A/$\lambda$. The first example is illustrated in figure 5.3 where, the crack patterns are shown for three different layer heights for the same substrate. Figure 5.3 depicts the crack patterns observed plate 1 at three layer heights, low, intermediate and high. For a crack pattern generated at low layer heights, cracks are observed in the troughs, however no cracks are observed on the peaks. In figure 5.3 (b), ladder-like cracks are shown where roughly two cracks per wavelength are observed, For a crack pattern generated with a large layer height, (figure 5.3 (c)) the crack pattern is isotropic, hence no information about the substrate can be gathered from looking at the crack pattern. This is represented by small values of spectral power. Comparing these crack pattern images with the data in figure 4.3, it is possible to observe that the values of spectral power are small for wavy and isotropic cracks.

For two different substrates, as long as they have the same A/$\lambda$, the spectral power will behave the same way and it must be scaled by the wavelength of the substrate to be compared. In figure 5.2 the crack patterns at different points are shown. Similar to the behaviour described above, wavy, ladder-like and isotropic cracks are observed. The spectral power for the inset images of figure 5.2 are shown in figure 5.5, where the spectral power is plotted against the wave-number. For a wavy crack pattern (figure 5.5 (a)) $\xi_x\lambda = 1$ and $\xi_x\lambda = 2$ are extremely small. This is consistent with figure 5.2. The spectral power for the ladder-like cracks is shown in figure 5.5 (b), where the order of highest to least is $\xi_x\lambda = 2$, $\xi_x\lambda = 1$ and $\xi_x\lambda = 3$. This crack pattern represents the highest point in figure 5.2. The spectral power behaviour in figure 5.5 (c) is representative of isotropic crack patterns. Here there are no peaks at the realtive wave-number of 1, 2 or 4. Figure 5.2 suggests that only a few of the plate 1 points are isotropic whereas for plate 2 a larger collection of $h$ values lead to isotropic crack patterns. This happens because the wavelength of plate 2 is smaller than than of plate 1.

A limitation of the Fourier method is that prior knowledge about the substrate is required.
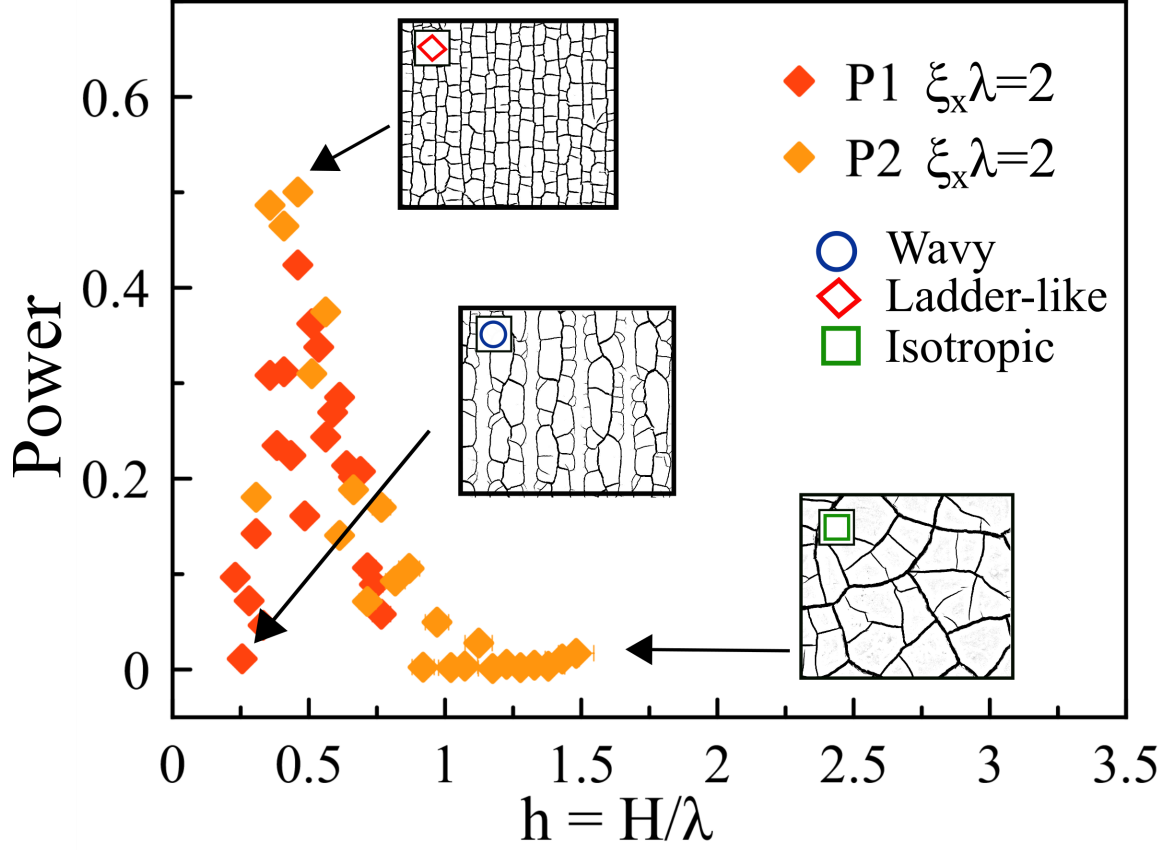
Figure 5.2: Spectral power vs $h$ for $A/\lambda = 0.25$ (Plate 1 and 2). At low layer heights, the spectral power has small value. At these layer heights, wavy cracks are observed at these layer heights. The crack pattern shown in the inset is from plate 1. At slightly higher layer heights, ladder-like crack patterns can be seen, the inset figure is for plate 2. In plate 2 at low layer heights both wavy cracks and ladder-like crack patterns can be seen. Here, straight cracks lie on the peaks of the plate and the cracks between the peaks tend to be wavy, such a pattern will still have a high value of spectral power at $\xi_x\lambda = 2$ since peak power does not differentiate between line shapes. It merely represents how many divisions there are per wavelength. Finally at large layer heights, crack patterns are isotropic. The inset figures are is from plate 2. In figure 5.5, the spectral power vs the wave number is shown for each of the crack patterns in the insets
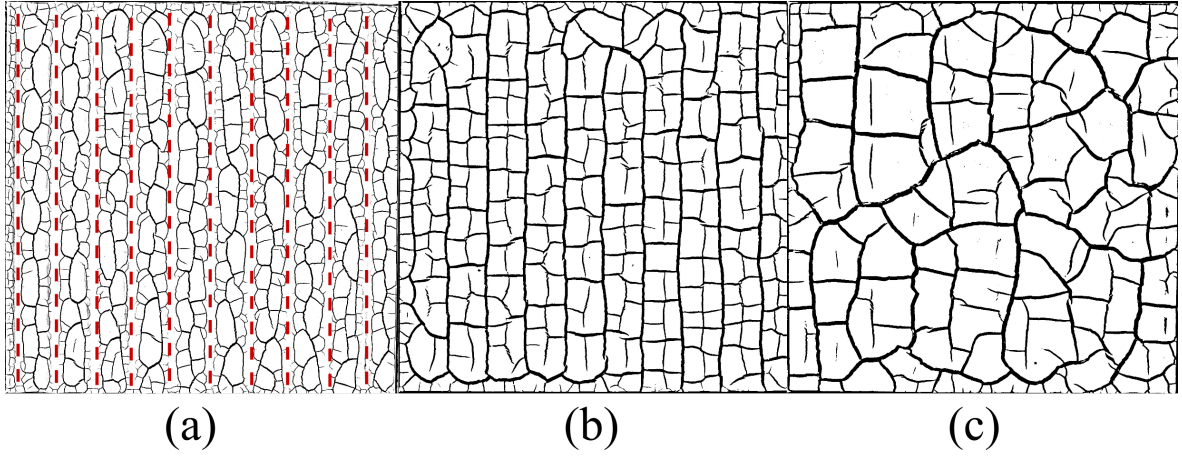
Figure 5.3: (a) Wavy, (b) ladder-like, (c) isotropic crack patterns. All crack patterns are generated on plate 1 which has $\lambda = 2$ cm. Hence, 10 wavelengths within the width of the image. Figure (a) represents a crack pattern at low layer heights where wavy cracks are observed. The dotted lines indicate the location of the peaks on the substrate. Extremely thin cracks which run perpendicular to the dotted lines appear on peaks, however in the process of creating a binary image they are eliminated due to the threshold. The spectral power for such a pattern is very low. Figure (b) is ladder-like crack pattern. For such a pattern, spectral power would have a maximum at $\xi_x\lambda = 1$ or 2. Figure (c) is an isotropic pattern which is generated due to large layer heights. Here very little information from the substrate is passed upto the crack pattern.

Without knowing the inherent symmetry of the substrate and, in case of the sinusoidal substrate, wavelengths of the substrate, it is not possible to plot figure 4.3 and hence acquire the power. While the symmetry of the substrate can be easily determined by studying the of the crack pattern, it is not possible to acquire the wavelength of the substrate by merely looking at the crack pattern.

The wavelength of the sinusoidal or radially sinusoidal plates can only be determined when the layer height at which the power has a maximum is determined, however in order to plot the power, wavelength must be know. For example, In figure 5.3 (b), one can conclude the crack pattern has a plane symmetry. Whereas without knowing the number of wavelengths of the substrate, it is not possible acquire the power for any crack patterns. This dependence of the crack pattern on structural information about the substrate makes it a unsuitable candidate for general applicability.

## 5.2    Cracking over a flat substrate

The crack spacing of an isotropic crack pattern was measured by Goehring et al. (2012) [36]. The results are presented in figure 5.6 (a). Goehring et al. measured the crack spacing of mud cracks dried in 150 mm Petri-dishes where the layer height was varied from 1 mm to 7 mm. They measured the crack patterns using the same methods presented in previous chapter : line dropping and the square root of the area of the cracked region $\sqrt{A}$. They observed that
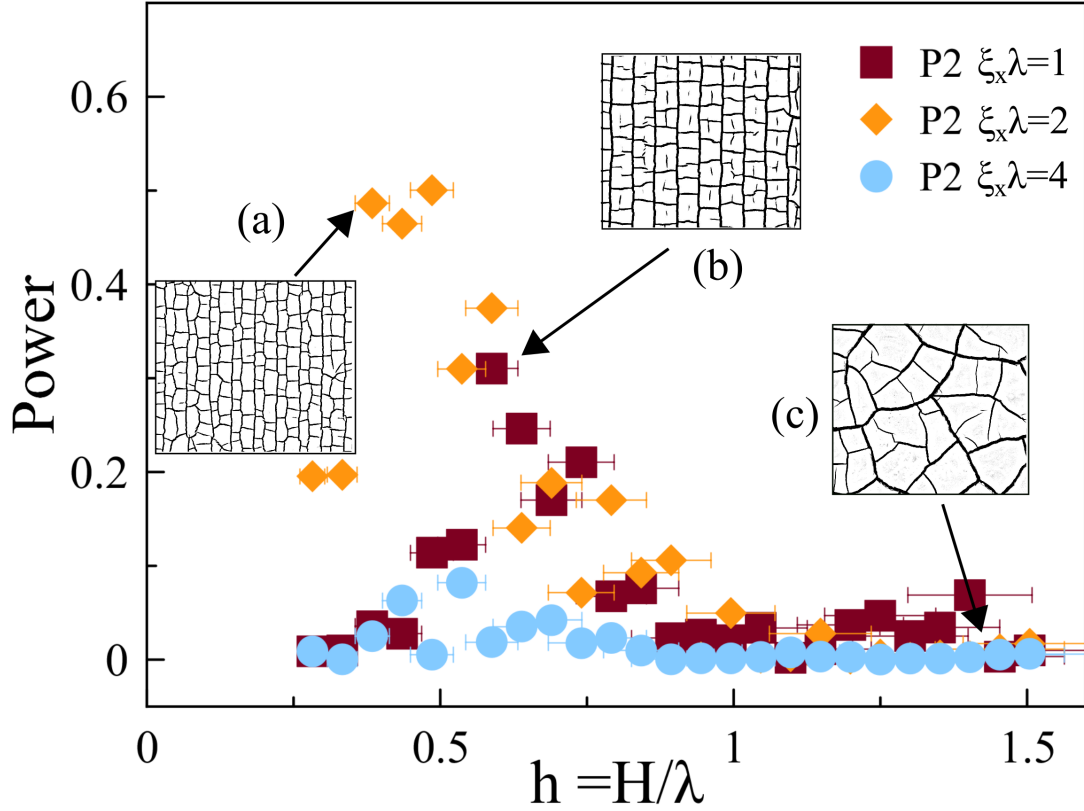
Figure 5.4: Normalized power at the selected wavenumbers for plate 2. Figure (a) shows a crack pattern where there are roughly two cracks per wavelength, figure (b) shows a crack pattern which has one crack per wavelength and figure (c) shows an isotropic crack pattern. The crack patterns near the peak at $h \approx 0.4$ have two cracks per wavelength, as the layer height increase, the crack pattern becomes ladder-like and in the regime $0.4 \leqslant h \leqslant 0.6$ the crack patterns go from having two cracks per wavelength to one crack per wavelength.

Figure 5.5: Power vs wave number for three types of cracks. In each case, the base wave number represents the number of wavelengths in the box. The wave number is proportional to inverse of the wavelength.
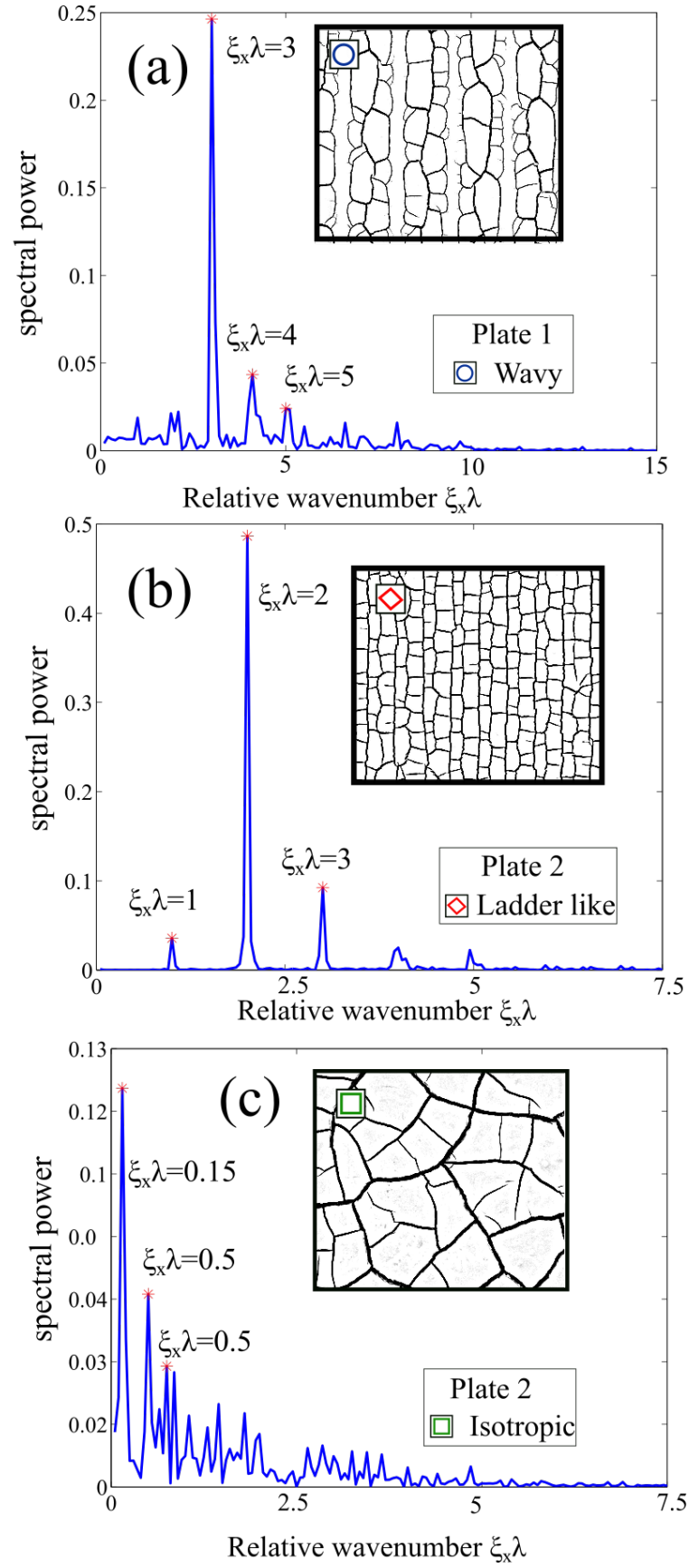
the crack spacing increases with increasing layer height and that for small layer heights the ratio of the crack spacing to layer height was significantly larger than for large heights. They also observed a $10-15\%$ decrease in the crack spacing using the line dropping method when compared to the $\sqrt{A}$ method [36].

Since the isotropic crack patterns generated by Goehring et al. are on a flat substrate, their measurements are compared against the experiments and the subsequent measurements on the flat plate. Figure 5.6 (b) shows the results of experiments conducted on the flat plate where both line dropping and $\sqrt{A}$ are used to a measure the cracking. In the figure, the ratio of the crack spacing and layer height is large for small layer heights and for increasing layer height the ratio decreases in magnitude.

In comparison to the results acquired by Goehring et al., the crack spacing in figure 5.6 is slightly lower, however the trend remains the same. In figure 5.6 (b), the crack spacing is calculated using two different methods. The first is the line dropping second is by calculating the $\sqrt{A}$ of each cracked region. The data shows that the $\sqrt{A}$ method is lower than line dropping method. This too is in agreement with the results acquired by Goehring et al. The crack spacing for flat plate is a control experiment and checks if at large layer heights the crack spacing for the sinusoidal plate will converge close to the results of Goehring et al. and the results in figure 5.6 (b).

The difference between the current result and Goehring et al. is also mainly because, Goehring et al. measure the dry layer height whereas here the wet layer height is measured. This means that the difference between their results and the results here represent the strain developed due to drying.

## 5.3 Crack spacing over sinusoidal substrate

The crack spacing for all the sinusoidal substrates are significantly lower compared to the crack spacing/$H$ ratio for the flat plate (figure 4.8 where $H$ is the layer thickness in centimetres. In the figure, the crack spacing values for plates 1,2 and 5 end at lower values than their starting values. However, it is important to keep in mind that this difference is not significant enough to constitute a trend. The crack spacing/$H$ ratio for plate 5 is higher than all the other plates. Conversely, the data for plate 4 and plate 1 have crack spacing values lower than all other plates. Plate 5 has an amplitude of A =0.25 and plate 1 and 4 both have A = 0.5. The plates with the higher amplitude seem to have lower crack spacing/$H$ ratio. While these difference in magnitude do exist between the crack spacing/$H$ ratio of the sinusoidal plates, they are not significant compared to the difference of crack spacing/$H$ ratio between the sinusoidal and the flat plate.

One reason why the crack spacing/$H$ ratio results in figure 4.8 for the sinusoidal plates do not agree with the flat plate results, especially at large wavelengths could be because the thickness in the sinusoidal plates is not constant. In the crack spacing/$H$ ratio the value for $H = \text{A}\sin\left(\ (2\pi x/\lambda)\right)$ where $\lambda$ is the wavelength of the plate. Hence, the ratio of crack spacing/$H$ using line dropping may not give the desired comparison.
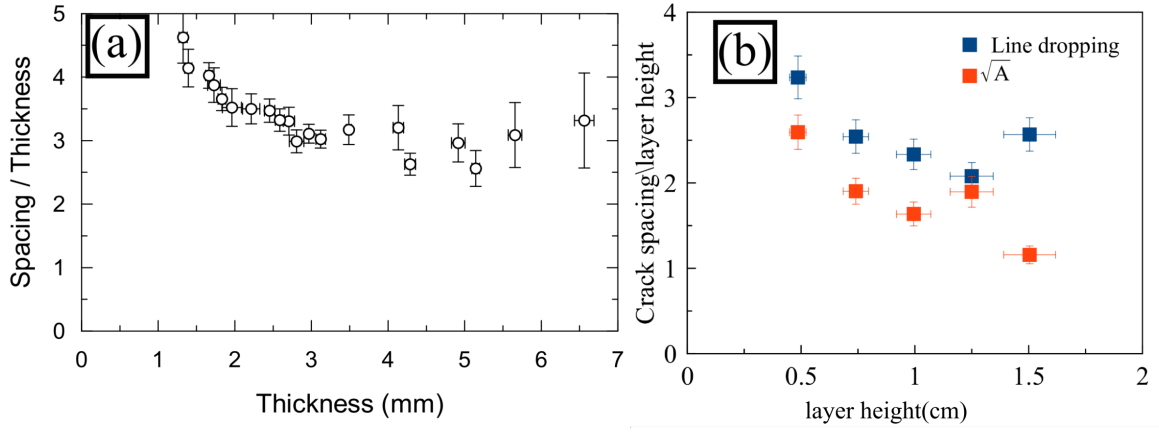
Figure 5.6: The crack spacing for an isotropic crack pattern. The pattern is generated on flat substrate. The ordinate is the crack spacing by the layer height. For small layer height, Goehring et al. find that the crack spacing is significantly larger than the layer height. Reprinted with permission of Dr L.Goehring. Figure (b) is the result of calculating crack spacing using two methods of crack spacing calculations are employed. The red data points were calculated using the $\sqrt{A}$ method, whereas the blue data points were calculated using the line dropping method.

In figure 4.9, crack spacing is calculated using the $\sqrt{A}$ method. As mentioned, the data collapse for this method is better. While calculating the $\sqrt{A}$, the shape of the cracked region is ignored and only the area is used. Hence while measuring a cracked region, the line dropping algorithm may drop a line in a direction in which the length of the region is the longest this value will be greater than the $\sqrt{A}$ method, which explains lower values of crack spacing/$H$ ratios for the flat plate. Furthermore, consider two different cracked regions which have very different shaped but the same area. In such a case, the line dropping algorithm would yield different values for the crack spacing, where as the $\sqrt{A}$ would yield the same spacing. Hence this may also influence the result for the flat plate. What is interesting is that there is little difference between the data for the sinusoidal plates in figures 4.8 and 4.9. In both figures, the data for plates 1 and 4 essentially behave in the same way, the data for plate 5 in figure 4.9 as compared to figure 4.8. While the values are lower, the trends seem to be the same.

The crack spacing contains no information about the transition from wavy to ladder-like to isotropic crack patterns since it remains relatively constant over the range of layer height. While there is no signature of crack pattern transitions in the crack spacing/$H$ ratio, there is however an impact on the ratio due to presence of an uneven substrate. For example, the flat plate approximation is not valid even in case of plate 5 regardless of having a low A/$\lambda$ and at large layer heights. Hence, since the crack spacing cannot be used as a means to distinguish crack patterns of different geometry and topology, the various parameters developed in the previous chapter are used quantify crack patterns.

## 5.4    Angle distributions of crack pattern

The angle distribution provides a measure of the crack pattern. The advantages of using the angle distribution as a measure over the Fourier methods was discussed in the last chapter. One major advantage is that, it is not necessary to know anything about structure of the substrate. What is required, however, is information about the the symmetry of the substrate. The symmetry of the substrate decides the direction of the unit vector that is used to measure the angles. In general, by looking at the direction of the primary cracks the symmetry of the crack pattern can be deciphered. Using this it is possible to assign an appropriate unit vector. Take for example the crack pattern in figure 5.3 (b). Without knowing anything about the structure of the substrate and by looking at the direction of the primary cracks, one can conclude that the angles for such a crack pattern are best measured in Cartesian coordinate system where the unit vector lies parallel or perpendicular to the crack pattern. Contrast this with the cracks in figure 5.7 (a) where the symmetry of the crack pattern suggests the use of a radial unit vector is appropriate in order to calculate the angle distribution. What of figure 5.7 (b)? Which unit vector should be used to calculate the angle distribution for such a crack pattern? The answer is that it does not matter. This can be inferred from the values of the various measurement parameters at large layer heights which all leads to zero for isotropic patterns regardless of the choice of reference vector.

In present experimental geometries, as mentioned in the previous chapter, the two unit vectors used to measure angles are : $\hat{\mathbf{x}}$ which is the unit vector perpendicular to the peaks of the sinusoidal plate and $\hat{\mathbf{r}}$ which is used for the radial plates. It lies in the direction of the vector that connects the center of the image and the $i^{th}$ crack intersection point. In figure 5.8, the angle distributions for the three representative crack patterns are shown for plate 1 and 2. Figure 5.8 (a) shows the angle distribution of a crack pattern with wavy cracks. In this distribution, there is large peak at $\theta = 90°$ with gradual decay in the distribution of angles on either side of the $90°$ peak. This suggests that in a wavy crack pattern, many cracks lie along the direction of the substrate. This happens because most of the slurry settles in the troughs of the substrate. Only a thin layer of the slurry remains atop the peak. Here the layer height is too small for the dried slurry to crack. As the slurry dries, wavy cracks form because a crack approaches the peak and either turns away due to the small layer heights, or eliminates at another crack forming a crack intersection point. In figure 5.3 (a), the primary cracks are wavy cracks which approach the peak then turn away, they travel from the top to the bottom of the plate. The primary cracks are surrounded by secondary curved cracks. This curvature ensures that while the primary cracks lie parallel to the peaks, angles other than $90°$ are also present.

Going back to the earlier discussion of the Fourier method where it was stated that the power cannot distinguish between a straight line and a curved line. The angle distribution differs for a crack pattern where the primary cracks are wavy cracks. Compare figure 5.8 (a) which is a wavy crack pattern to figure 5.8 (b) where the crack pattern is ladder-like. There are three prominent peaks in the distribution at $\theta = 0°, 90°, 180°$, where as in the former, while there is a peak at $90°$, the peaks $0°$ and $180°$ are absent. This angle distribution of

figure 5.8 (b) strongly reflects a pattern where there are crack parallel and perpendicular to the substrate. There are virtually no other angles present near $\theta = 45°, 135°$. For the crack pattern in figure 5.8 (a), the cracks are perpendicular to the substrate are absent. Hence no peaks are seen 0°and180°. Hence, the angle distributions can be used distinguish between crack patterns that are wavy and ladder-like. The final image in figure 5.8 is the angle distribution of an isotropic crack pattern where there is no peak at $\theta = 90°$, there are no dominant angles in this specific angle distribution. This shows that the crack have no preference of direction.

The angles distributions generated so far need to be condensed into a single number and this is done by calculating $S_{Angles}$. This parameter has a maximum value of 1 and a minimum value of -1. In figure 4.4, $S_{Angles}$ was used as a means to quantify crack patterns. One interesting exercise is to use $S_{Angles}$ to check how the results of figure 5.8 (b) vary with changing bin size. In figure 5.9, using two different bin sizes angle distributions are generated. For the bin size of 2°, $S_{Angles} \approx 0.74$ and for 10°, $S_{Angles} \approx 0.72$. For the standard bin size of 5°, $S_{Angles} = 0.75$, hence this variation is not significant and is within the error values of point for a standard bin size.

Applying $S_{Angles}$ to plates 1-4 and radial plates 1 and 2, one finds that the $S_{Angles}$ behaves non monotonically with increasing layer height. At low layer heights $h < 0.6$, wavy cracks are observed. Plate 1 is observed to have the maximum number of crack patterns with wavy cracks. This is reflected in the $S_{Angles}$ values for plate 1 where close to half of the data points lie to the right of peak in $S_{Angles}$. Plate 4 has wavy cracks as well and they are captured by the low values of $S_{Angles}$ at small layer heights in figure 4.4 (b).

As mentioned in Chapter 4, peaks are observed for A/$\lambda = 0.25$ at approximately $h \approx 0.5$ and for A/$\lambda = 0.5$ at approximately $h \approx 1$. These peaks suggest that there is a relationship between the periodicity of the substrate and the periodicity of the crack pattern. At this point, the crack pattern is representative of the substrate since the crack pattern contains the same number of primary cracks as the number of wavelengths of the substrate. With the primary cracks lying on the peaks, the secondary crack generally occur perpendicular to the peaks, this is what is observed in a ladder-like crack pattern. Hence a ladder-like crack pattern represents a condition where the influence of the substrate on the crack pattern is maximum. The influence of the substrate wanes with increasing layer height. The change from a ladder-like crack pattern to an isotropic pattern is quantified by the decay of $S_{Angles}$ at large layer heights in figure 4.4. The decay of $S_{Angles}$ for A/$\lambda = 0.25$ i.e plate 1 and 2 has a constant slope, whereas for plate 3 and 4 A/$\lambda = 0.5$ the decay tends levels off at $h \approx 1$ beyond this there is a large amount of scatter in the data. At $h \approx 1$, $S_{Angles}$ reaches a minimum.

$S_{Angles}$ values for the sinusoidal and radially sinusoidal plates, at large $h$ values must be comparable to the $S_{Angles}$ value for crack patterns generated on the flat plate. This is shown in figure 5.10 where the black line is $S_{Angles}$ value for the flat plate ($S_{Angles} = 0.0079 \pm 0.1$). The red lines are the errors for the flat plate $S_{Angles}$ values. In figure 5.10 (a) plate 2 and radial plate 2 values either come close to or lie within the flat plate error range. In case of figure 5.10 (b), both plate 3 and radial plate 1 have values within the flat plate error range.

These trends for both 5.10 (a) and (b) suggest that even at large layer heights, plate 1, plate 4 do not generate crack patterns that are entirely isotropic. This is essentially due to the large wavelengths of the both plates which restricts them from exploring higher $h$ values.
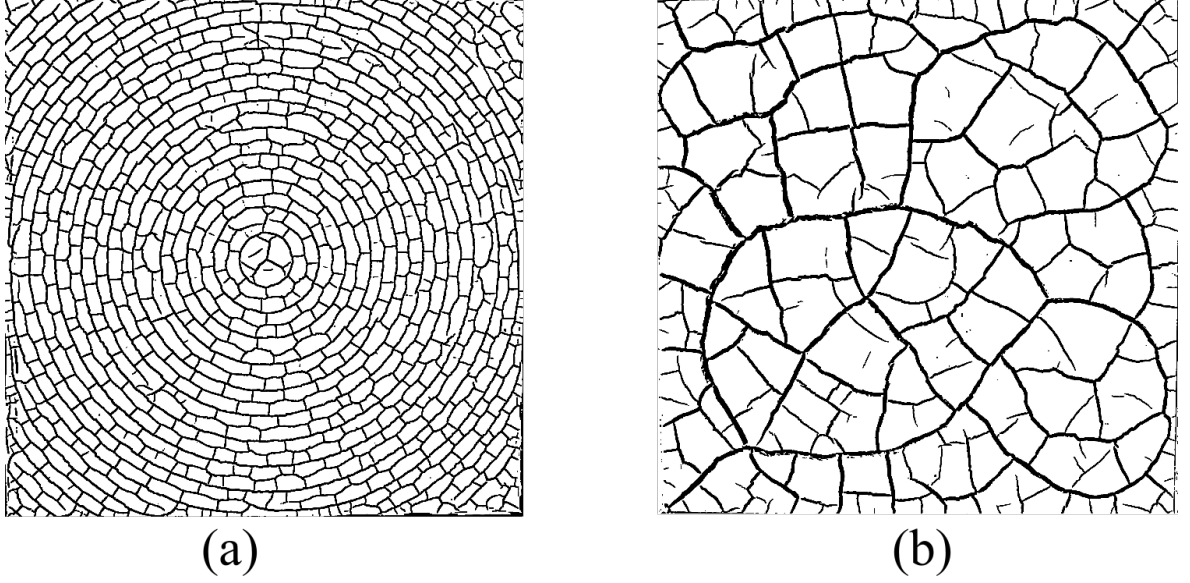


(a)

(b)

Figure 5.7: Crack patterns generated on radial plate 2. For both crack patterns a radial unit vector $\hat{\mathbf{r}}$ is used to measure the angles. Figure (a) is a crack pattern at low layer height where the primary cracks rest atop the peaks. Between peaks, the presence of wavy crack can be see. Figure (b) is a crack pattern at a large height, in such a situation it is difficult to decipher whether to use a radial unit vector or a Cartesian unit vector.

The behaviour of $S_{\text{Angles}}$ with increasing $h$ values captures the essential features of crack pattern transitions for all plates. A supporting case for the behaviour of $S_{\text{Angles}}$ is made by measuring the orientation of crack skeletons. The average crack orientation $C_{\text{Ort}}$ yields angle distributions similar to the one observed in figure 5.8 for the three types of cracks. The crack orientation in figure 4.5 bear close resembles to figure 4.4. At low layers heights, in both figure 4.5 (a) and figure 4.4 (a), the values start close to 0.2 and in both cases there are peaks at $h \approx 0.5$. For figure 4.4 (b) and figure 4.5 (b) the results are also the same for the sinusoidal plate, however the values of radial plate 1 are lower in figure 4.5 (b) compared to figure 4.4 (b). Nevertheless, $C_{\text{Ort}}$ for radial plate 1 behaves similarly to the data in figure 4.4 (b) especially at large layer heights.

$C_{\text{Ort}}$ not only confirms the results of $S_{\text{Angles}}$ , but also provides a new way to calculate the angle distribution with certain advantages. A major advantage of $C_{\text{Ort}}$ over $S_{\text{Angles}}$ is that $C_{\text{Ort}}$ does not require the calculation of crack intersection point neighbours. This is useful at low layer heights where the crack pattern contains many connected network. In such networks, finding neighbours of crack intersection points is difficult but since $C_{\text{Ort}}$ does not require a connected network, it can be used to quantify crack patterns. This also means that $C_{\text{Ort}}$ can be applied in quantifying and measuring the average orientation of unconnected cracks. This would not be possible with $S_{\text{Angles}}$ . One situation where $C_{\text{Ort}}$ may not work would be when the curvature of the cracks is too high, since calculating $C_{\text{Ort}}$ involves the
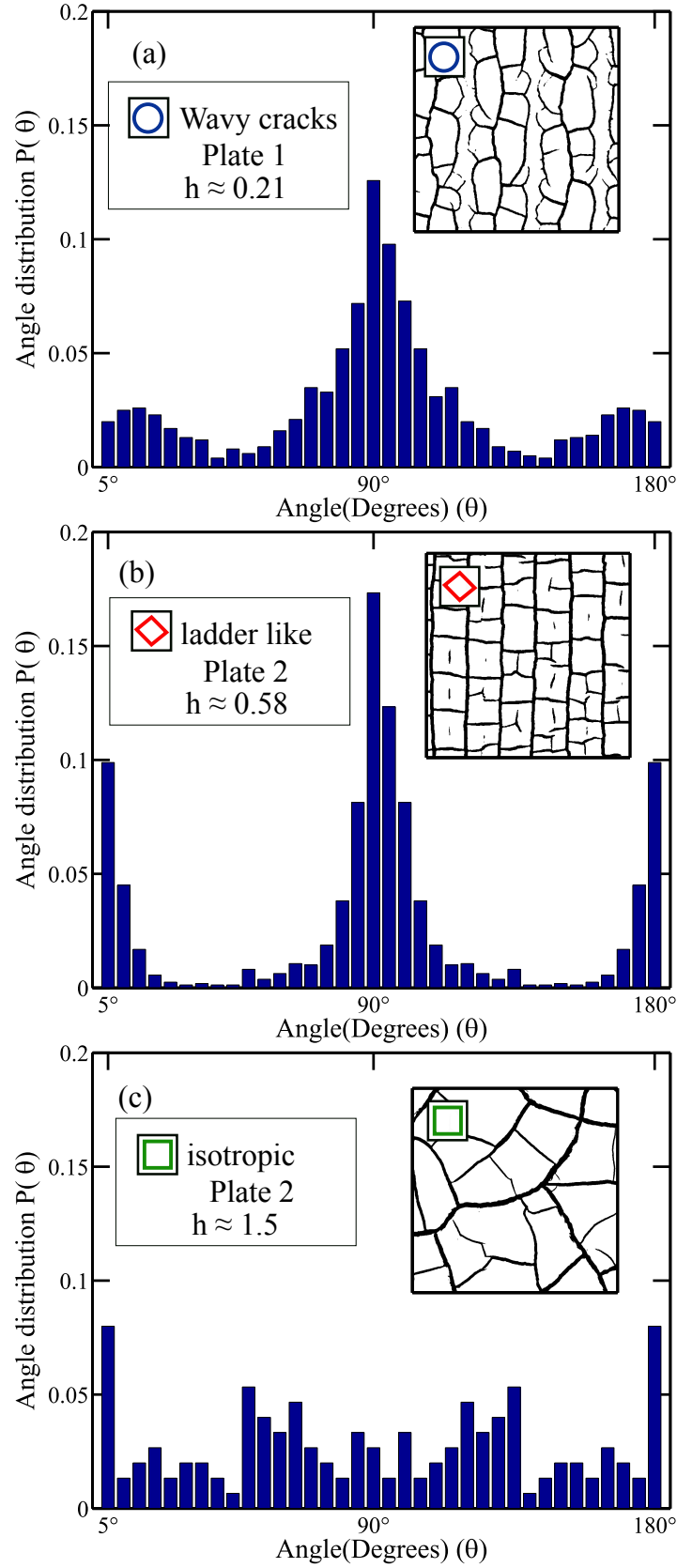
Figure 5.8: Angle distribution of the three types of crack pattern : wavy (figure (a)), ladder-like (figure (b)) and isotropic (figure (c))
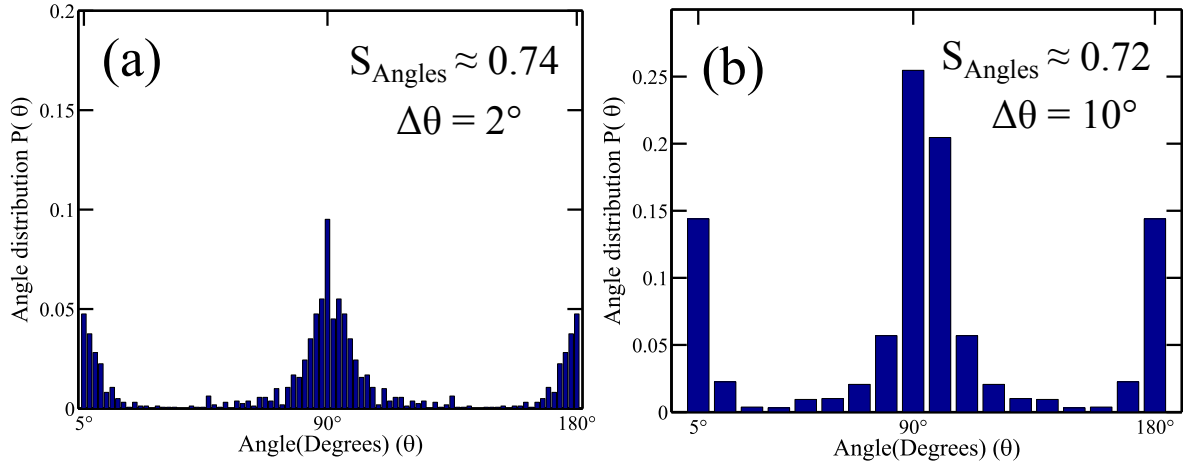
Figure 5.9: Variation of angle distribution with the bin size. The standard bin size used to calculate the angle distributions for all dimensionless layer heights was 5°. In figure (a) the bin size used is 2°, in figure (b) the bin size is 10°. The $S_{Angles}$ value for the standard bin size is $S_{Angles} \approx 0.75$, as shown above there is little variation in $S_{Angles}$ values

.

orientation of an elliptical fit of the crack skeleton.

Both $S_{Angles}$ and $C_{Ort}$ measure information about the crack pattern at the level of the crack intersection points. While this has certain advantage, this may become cumbersome for crack patterns with large number of crack intersection points. In such situations, the parameter $S_{Ort}$ can be used.

## 5.5 Orientation of cracked regions as measure of crack patterns

The parameter $S_{Ort}$ serves to forego the use of crack intersection points and instead relies on crack regions to measure a crack pattern. The crack patterns must still be connected networks for this method to work. $S_{Ort}$ is applied to the same system as in last section, plates 1-4 and radial plates 1 and 2. Figure 4.6 shows the data for plate 1-4 and the two radial plates. The behaviour of $S_{Ort}$ is similar for plates 1 and 2 with a peak at $h \approx 0.5$. However there is no peak observed in the data for $A/\lambda = 0.5$. The data for radial plate 1 collapses with the data for plate 2, it does not however share the peak with plate 1 and 2.

The lack of a peak in figure 4.6 (b) will be first addressed. Recall, in the last section, it was mentioned that cracks below the peak were wavy, however as per figure 5.11 this turns out to be not true. This discrepancy highlights the difference between the parameters $S_{Angles}$ and $S_{Ort}$ . In figure 5.10 (b), although the values of $S_{Angles}$ are lower than that of the peak, this does not necessarily mean that the crack pattern is wavy. Notice in figure 5.10 (a), the initial values for plate 1 are as low as $S_{Angles} \approx 0.3$, whereas for figure 5.10 (b) the lowest value on the left side of the peak is $S_{Angles} \approx 0.6$. Somewhere between these two values, the crack patterns start becoming more ladder-like, however, wavy cracks are also present in the pattern. The parameters $S_{Angles}$ and $C_{Ort}$ are sensitive to coexistence of wavy cracks and
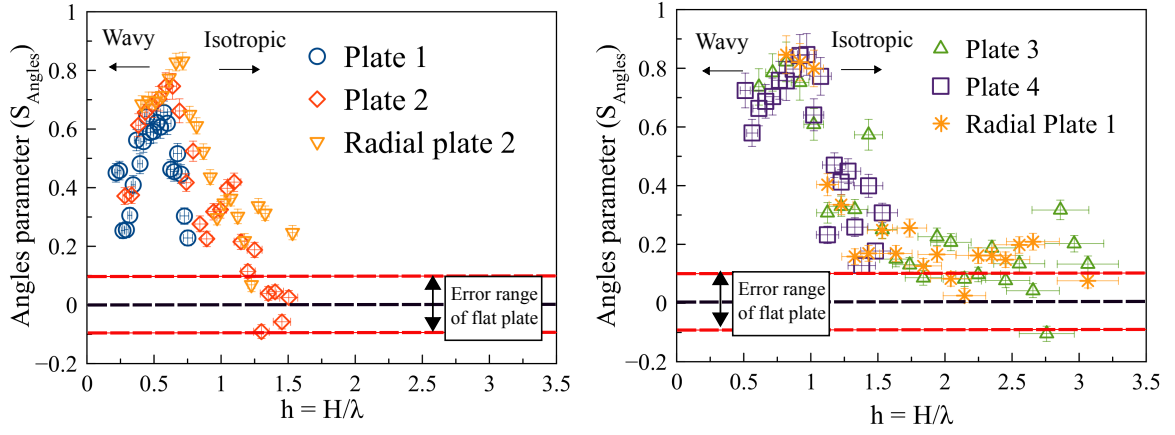
Figure 5.10: $S_{Angles}$ over all layer heights. The black lines represents the flat plate data where $S_{Angles} = 0.0079 \pm 0.1$, the red lines represents the error range values for the flat plate. The peaks in the data represent the point where the crack pattern has strictly one vertical crack per wavelength. This crack will be located on the peak, below this limit wavy cracks occur to the left of peak. To the right of the peak, an isotropic crack patterns are observed.

ladder-like cracks, and this where $S_{Ort}$ is different. $S_{Ort}$ is unaffected by the local curvature of the crack. For example, if $S_{Ort}$ values are calculated for an ellipse whose major axis is parallel to the length of a rectangle, both geometries will yields the same value of $S_{Ort}$. Any changes in local curvature along the edges of the ellipse will not greatly alter the average orientation of the ellipse. This applies to cracked regions as well, hence in patterns like those presented in figure 5.11, the curvature of the wavy cracks is of little consequence to the parameter $S_{Ort}$. Even for the wavy cracks, if both their ends terminate at a crack intersection point and they form a closed region which is long in direction parallel to the peak of the substrate then their orientation will be close to $\theta = 90°$. Due to this insensitivity to local curvature, the initial values of $S_{Ort}$ are very high. This is also the same reason why there is no peak in the radial plate 2 data for $S_{Ort}$.

The insensitivity to curvature has its benefits. Looking back, suppose, only the data in figure 5.10 (a) and (b) were presented, one would naively jump to the conclusion that the crack patterns to the left and the right of any peak in the data are not affected by the the substrate. However, measuring $S_{Ort}$ would clearly show that this is not the case.

The one major drawback of using $S_{Ort}$ occurs at large layer heights where there a very few cracked regions. For example, in case of plate 3, at the lowest layer heights, 1291 cracked regions are measured, but at the highest layer height, only 63 regions are measured. The small number of regions is what is responsible for the scatter in the values of the $S_{Ort}$ at large layer heights. With increasing layer height, the crack spacing increases which cause the area of the cracked regions to increase as well. As the cracked region area keeps increasing, the scatter in the data for $S_{Ort}$ also increases. Hence, for large layer heights $S_{Ort}$ will break down and will not yield consistent results but will have large errors.

An interesting parallel exists between $S_{Ort}$ and the orientational order parameter defined for liquid crystals given by Stephen et al. (1974) [83]-

$$S = \left\langle \frac{d\cos^2{(\theta)} - 1}{d - 1} \right\rangle = \langle \cos{(2\theta)} \rangle, \tag{5.1}$$

where $\theta$ is the orientation of a single molecule, the angled brackets indicate an average over all molecules in the system. The orientation of the molecule is measured with respect to a director, which is calculated by averaging the orientation of all the molecules in the neighbourhood of the molecule. The values of S range from -1 to 1. The value of 1 represents a nematic structure, whereas the value of 0 represents an isotropic state. The order parameter S quantifies the change in structure of the system, for example with increasing temperature, liquid crystals will transition from an ordered phase to an isotropic phase. This is reflected in the sharp drop of S at a certain temperature.

The order parameter S and $S_{Ort}$ are similar. Both measure orientations around a director. In case $S_{Ort}$ , the director is a global director. It is predefined by the structure of the substrate. $S_{Ort}$ can though as a two dimensional analogue to the order parameter S.

An interesting extension to $S_{Ort}$ would be add the concept of the director. This would identify a direction of bias for the crack pattern which in turn would aid in quantify the crack pattern in for example, a condition where the layer height is not constant. In such a situation a crack pattern can suddenly transition between wavy cracks to a ladder-like pattern.

$S_{Ort}$ , as a measure of the crack pattern, is less local than $S_{Angles}$ and $C_{Ort}$ , it does not depend on crack intersection points or the local orientation of the cracks. $S_{Angles}$ and $C_{Ort}$ operate on the level of a pair of intersection points, whereas it would take a minimum of three crack intersection points to define a cracked region, for large layer height, larger number of crack intersection points are required to define a cracked region, therefore it $S_{Ort}$ can be considered less local than $S_{Angles}$ and $C_{Ort}$ . However, $S_{Ort}$ will always be influenced by the orientation of the neighbouring regions . In the next section a global measure of the crack pattern, $S_{Man}$ , is presented.

## 5.6   Walking along a crack pattern: The Manhattan metric

The measures of a crack pattern discussed so far have all been local. $S_{Angles}$ and $C_{Ort}$ measure crack angles around a crack intersection point, $S_{Ort}$ measures the orientation of regions which contain few cracks. What is lacking is a global measure of the crack pattern. A measure that uses points or structures that are not nearest neighbours to quantify a crack pattern. The benefit of such an approach is that local variations in the structure do not affect the overall measurement of the crack pattern. $S_{Man}$ is a measure that utilizes the full crack pattern. $S_{Man}$ involves calculating the ratio of distances $s_{Man}$ for each pair of crack intersection points that lie on opposite ends of the image and averaging them to yield $S_{Man}$  (note: it is small s for each pair of points compared to S for the whole pattern). The ratio of distances is the ratio of the Euclidean distance over the distance traveled over the crack pattern. A caveat with the measurement of $S_{Man}$ is the low range of values explored, $S_{Man}$ goes from 1 which occurs for a straight line to $1/\sqrt{2}$ where $\sqrt{2}$ represents the least distance, calculated using the Manhattan metric, between two non-neighbouring grid points. The implications of this

# Plate 4 : Crack patterns below h=1



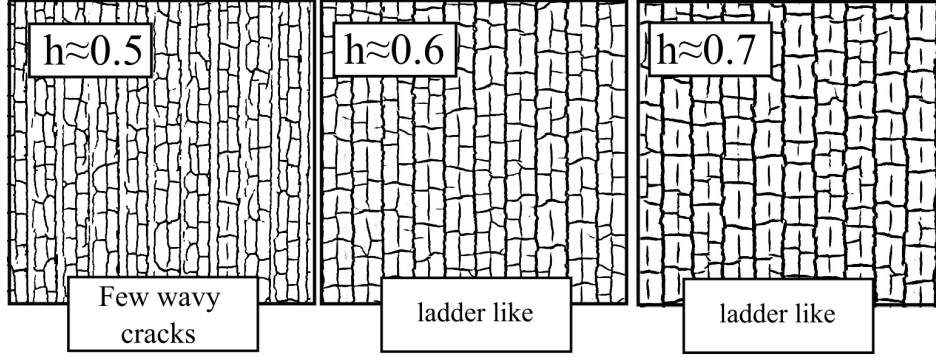h≈0.5 — Few wavy cracks

h≈0.6 — ladder like

h≈0.7 — ladder like

Figure 5.11: Crack patterns generated on plate 4. From left to right the dimensionless layer height $h = 0.48, 0.58, 0.69$. For $h \approx 0.5$, Most of the cracks are parallel to the peaks however some wavy cracks are present. These wavy cracks are generally between the peaks. For $h \approx 0.6$ and $h \approx 0.7$ the crack pattern is ladder-like. It is interesting to note that second figure contains many secondary cracks that are connected to main ladder-like crack pattern, contrast this with the third figure where there is a ladder-like crack pattern however most of the secondary cracks that lie parallel to the peaks are disconnected from the main crack pattern. The Fourier methods presented in the earlier section will distinguish between these two crack patterns, however $S_{Ort}$ makes no such distinction.

range and the effectiveness of $S_{Man}$ will be discussed below in context to the data acquired for the sinusoidal plates.

Figure 5.12 shows the data for $S_{Man}$ measurements over plates 1-4. For $A/\lambda = 0.25$ $S_{Man}$ does not behave similar to any of the order parameters. Most of the values for $S_{Man}$ are clustered around $S_{Man} = 0.96$ for plate 1. Plate 2 does approach the values for the flat plate, however here too the ordinate values are very small. The situation is better for $A/\lambda = 0.5$ plates where a peak can be seen at $h \approx 1.0$. This figure also contains the data for the Manhattan metric with the flat plate data averaged and shown as the black line. The red dashed lines are the error values for the flat plate. One would expect that since the flat plate represents a completely isotropic pattern. The value of $S_{Man}$ would be close to 0.707. However, this is not observed. For all the flat plate crack patterns. the ratio $S_{Man}$ is $0.81 \pm 0.025$. This difference could be due to restriction placed during the calculation of $S_{Man}$ that two crack intersection points can form pairs if they are within $10°$ of each other. The selection of this range is arbitrary however, it is done to ensure that measurements are made along the direction of the substrate. Another aspect that could be responsible for the higher values of $S_{Man}$ is that while the ratio of distances does involve traversing the crack pattern, the distance between two neighbouring crack intersection points is the Euclidean distance. This means in certain situations below such the $s_{Man}$ values will be higher that what one would achieve traversing along the crack pattern.

In figure 5.12 the points labelled 1 and 2 represent the crack patterns in figure 5.13 (a) and (b), which show the path traversed along a ladder-like and an isotropic crack pattern. For the ladder-like crack pattern, the Manhattan metric approach gives $s_{Man}$ close to 1, and
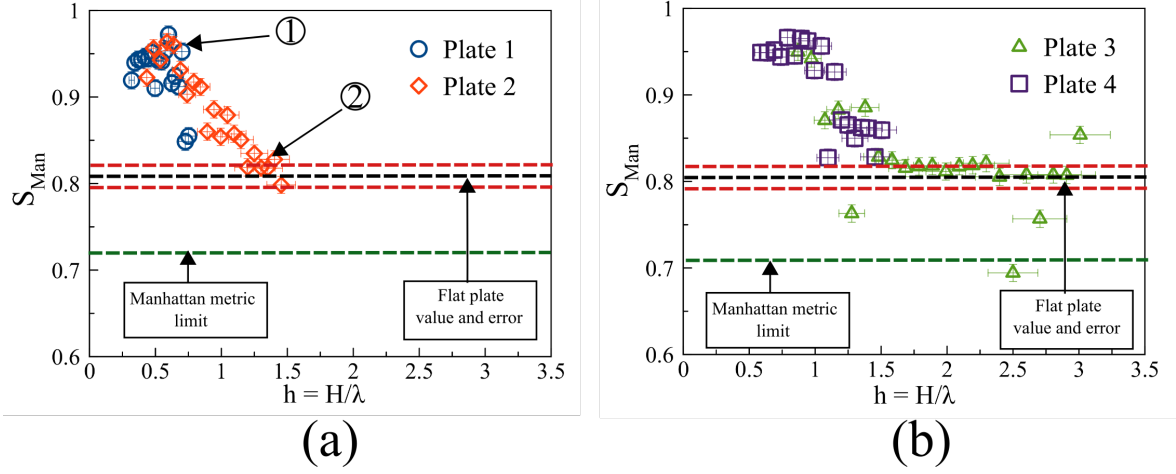
Figure 5.12: $S_{Man}$ for all layer heights. The black line in the image represents $S_{Man} = 0.81 \pm 0.025$. The red lines are plus and minus of the error. The green line represents the value 0.707 which is the shortest distance between two non neighbouring points on a grid using the Manhattan metric. $S_{Man}$ does not differentiate between wavy cracks and ladder-like cracks for $A/\lambda = 0.25$ hence no peak is observed in figure (a). The numbers 1 and 2 refer to figure 5.13 (a) and (b).

for isotropic cracks the values lower, close to 0.8. Notice despite large variations in the path for the isotropic cracks the $s_{Man}$ values are still close to 0.8. This suggests that $S_{Man}$ values are extremely sensitive to variations in the crack pattern. While the range of y values for $S_{Man}$ is small, the error one of these values is also extremely small. Hence even a difference of 0.1 is significant in representing changes in crack pattern. This is seen in figure 4.1 (b) where the scatter in $S_{Man}$ values at large layer heights is very minor. While scatter is present at larger layer heights, this is because there are fewer vertices and here forming a top section and bottom section of crack intersection points is not possible.

Unlike the parameters $S_{Angles}$ and $S_{Ort}$ there is no definitive signature of wavy cracks within the data for $S_{Man}$ . This is because, as it is currently defined, $S_{Man}$ would not follow the curvature of the cracks since between neighbouring points, the traveled path is a straight line. While it cannot identify wavy cracks, $S_{Man}$ can be used to differentiate between ladder-like and isotropic cracks.

The attempt so far as been to experimentally study various substrates and understand how crack patterns change with changing layer heights. In the next section a model proposed by Dr. L.Goehring is presented and the data for $S_{Angles}$ is compared with the model.

## 5.7   Comparison with simulations

The experimental data is compared to FEM simulations carried out by Lucas Goehring. These simulations explain the transition from wavy cracks to straight cracks by calculating the strain energy due to a crack opening over a sinusoidal surface.

The drying clay is modeled as a poroelastic material. The stress in the medium is described
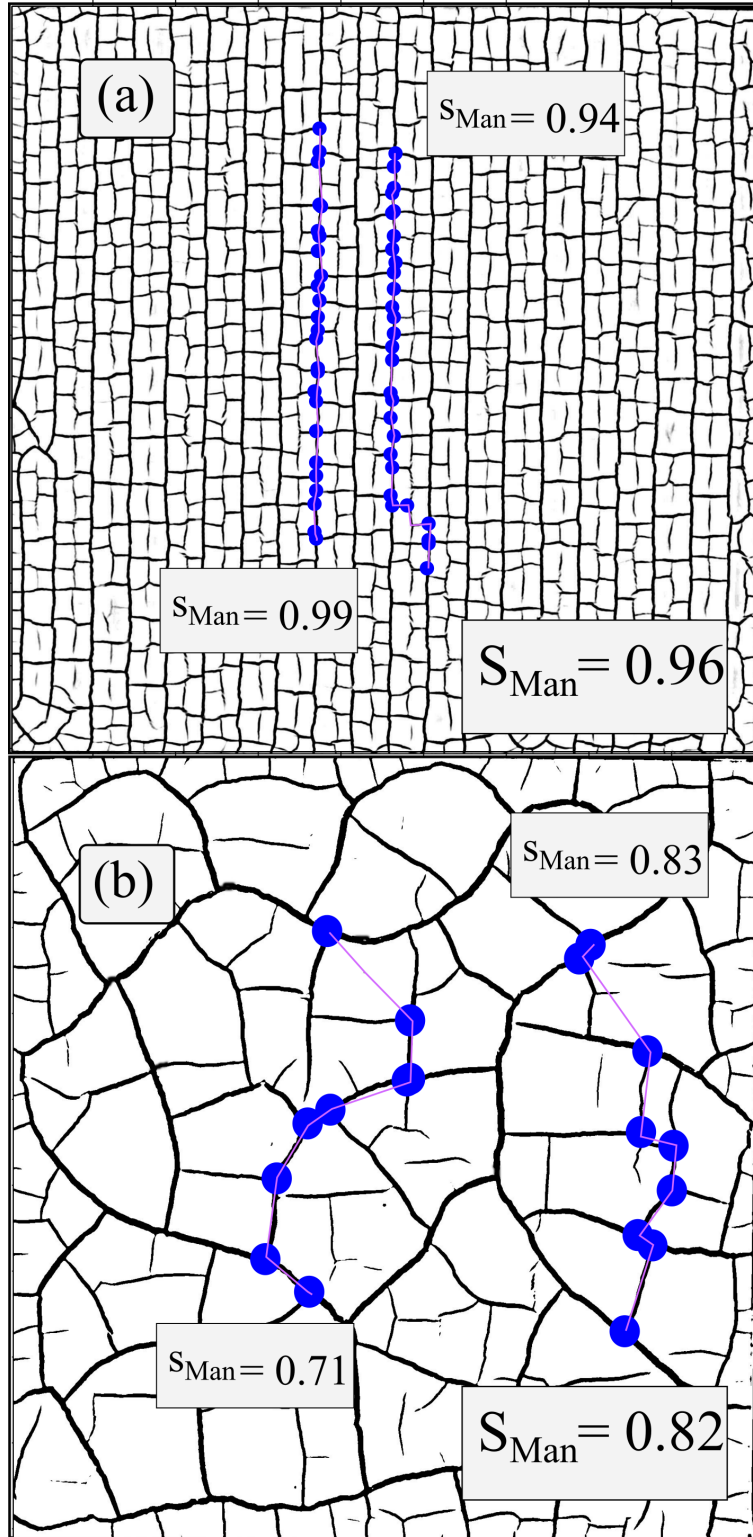
Figure 5.13: $s_{Man}$ measurements on a ladder-like and isotropic crack pattern. Two paths are presented for each image. Figure (a) corresponds to 1 in figure 5.12 and figure (b) corresponds to 2 on in figure 5.12.
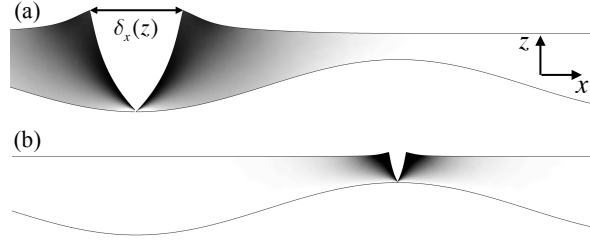
Figure 5.14: Examples of the simulation region where FEM simulations are carried out. $\delta\,(x)$ represents the crack opening displacement. This region has been exaggerated for clarity. The bottom profile in both figures is given by equation 5.4. The black regions are regions of high stress release, and the white region is stressed.

by

$$\bar{\sigma}_{ij} = \sigma_{ij} - p, \tag{5.2}$$

where $\bar{\sigma}_{ij}$ is total stress in the material which depends on the stress in the clay stress in the clay network, which is denoted by $\sigma_{ij}$ and $p$ is the capillary pressure within the pores. The stress in the clay network $\sigma_{ij}$ can be expresses in terms of the strain as

$$\sigma_{ij} = \frac{E}{1+\nu}\left(e_{ij} + \frac{\nu}{1-2\nu}e_{ll}\delta_{ij}\right), \tag{5.3}$$

the strains in the material $e_{ij}$ can be expressed in terms of the displacement of the cracking medium (equation 1.2).

Equations ( 5.2, 5.3, 1.2) are solved in regions such is shown in figure 5.14 where the top surface is $z = 1$ and the bottom surface is given by

$$z = 1 - \ell = A\cos\left(\frac{2\pi x}{\lambda} + \phi\right), \tag{5.4}$$

where $\ell$ is the local layer thickness, $A$ is the amplitude of the cosine wave and $\lambda$ is the wavelength. The left side of both the regions in figure 5.14 is set to $x = 0$ and the right side is set to $x = 10$. There are no displacements along the $y$ axis i.e a plane strain condition is applied in the $y$ direction. The surface of the cracking medium which is $z = 1$ is assumed to be traction free. The lower surface is set to $u = 0$ which means there is a no slip.

The model involves calculating the amount of work done in creating the crack. The drying slurry has internal stresses that build up, this is the stress in the material before it cracks **??**. The work done due to a crack opening can be expressed as a product of the displacement and the forces on the cracking medium-

$$G = \frac{1}{2\ell}\int_{1-\ell}^{1}\delta_x\sigma_x^* + \delta_z\sigma_{xz}^*dz, \tag{5.5}$$

where $\delta_x$ is the crack opening in the $x$ direction, $\delta_z$ is the displacement in the z direction, $\sigma_x^*$ is the stress in the material in the $x$ direction before the crack opening and $\sigma_{xz}^*$ is the shear stress in the material due to crack opening.

For a value of $A$ and $\lambda$ the pre-stress in the material is calculated for $\phi = 0$. Then values of $\phi$ over the sinusoidal substrate, the strain energy released $G$ and the crack opening
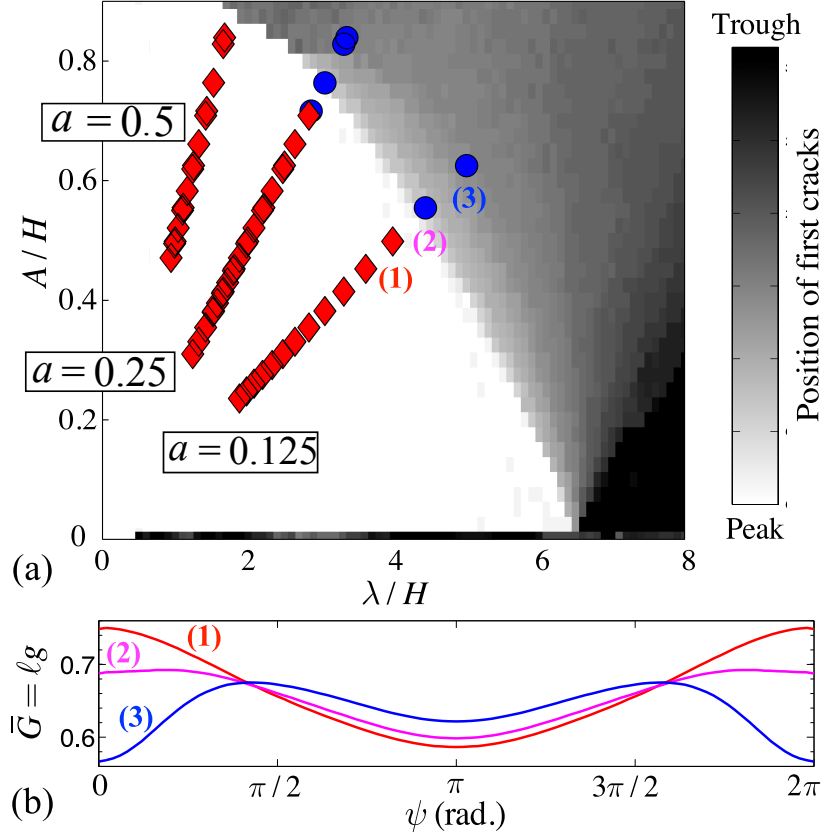
Figure 5.15: Transition from wavy to straight cracks. (a) Shows for various values of $A$ and $\lambda$ the location of the crack is represented by the color of at point. The red and blue points are the experimental data, the red diamonds are the ladder-like cracks, the blue circles are the wavy cracks. The three lines of points represent the three amplitude to wavelength ratios $a = A/\lambda = 0.5, 0.25, 0.125$. Point (1) represents a ladder-like crack pattern, point (2) represents a crack pattern that is predominantly ladder-like however contains some wavy cracks, point (3) is a wavy crack pattern. Figure (b) shows the strain energy release curves for all three points.

is acquired. This procedure is carried out over a large range of values and is plotted in figure 5.15 (a). The wavelength and the amplitudes are normalized by the layer height $H$.

In figure 5.15 (a), the lighter regions represent cracks that are close to the peak. They darker regions represents cracks located in the trough. A transition can be seen between the white region and the grey region. This represents the transition from a ladder-like to wavy crack pattern. Near the transition region, it is possible to observe a mixture of wavy and ladder-like crack patterns. The experimental data points in figure 5.15 (a) are the same in figure 4.1. No wavy cracks are present for $a = 0.5$ and this is reflected in the figure 5.15 (a). For $a = 0.25$ at few layer heights, there are wavy cracks in crack pattern. This is reflected well in figure 5.15 (a). The crack pattern for $a = 0.125$ show a transition from wavy crack to ladder-like cracks and this is capture by the numerical model. Three points from the experiments are picked up and the strain energy released according to model is plotted in figure (b). Point (1) represents a ladder-like crack, point (2) represents a mixture of ladder-like and wavy cracks and point (3) represents a wavy crack pattern.

The strain energy release curves for points (1), (2) and (3) are plotted in figure 5.15 (b). The ordinate of the figure is $\hat{G}$ which is the normalized value the strain energy release. Strictly speaking $G$ corresponds to the crack energy release rate [12]

$$G = \frac{1}{2} \frac{\sigma^2_0 h}{\bar{E}} \pi g, \tag{5.6}$$

where $\bar{E} = E/ \left(1 - \nu^2\right)$, $\sigma_0$ is the stress in the medium, $h$ is the depth of the crack in the film and $g$ is a dimensionless value which is a function of the elastic mismatch between the substrate and the cracking film[12, 29]. Using $\nu = 1/3$, $G$ can be rescaled by $2\bar{E}/\pi\sigma^2_0$ to get $\bar{G}$. In the model, $h = \ell$ hence $\bar{G} = \ell g$.

In 5.15 (b), (1) represents the strain energy released for a ladder-like crack, it is evident that $G$ is a maximum at the peaks of a substrate i.e when $\phi = 0$ or $2\pi$. This suggests that cracks will occur first on the peaks of the substrate. The strain energy release curve for (2) is lower than that of (1). The maxima of the curve have moved closer to $\phi = \pi/2$. This is closer to the halfway point between the peak and the trough which suggests that the crack can be located on either side of the peak. Empirically, this represents a condition where the primary cracks lie atop the peaks but can slightly meander. In curve (3), there are two peaks at $\phi = \pi/2$ and $\phi = 3\pi/2$ . These two peaks mean that there are two solution which are permitted and that the experiment chooses both solutions. This condition is found at low layer heights. For example point (3) is approximately $\lambda/H \approx 0.2$ which, for plate 5, is one of the lower layer heights. In figure 4.1, it is observed by visual inspection as wavy. Hence, it can be concluded that wavy cracks can be observed for any of the gray regions in 5.15 (a). While this model explains the experimental data, it also provides a predictive tool for future experiments.

# Summary

The aim of this chapter was to bring together the experimental observations and the methods of quantifications developed earlier. To facilitate a union of these ideas, three questions were posed in the beginning of the chapter. The first question was : are the results of quantification consistent with the experimental observations? The measures of crack pattern capture the crack transitions to varying degree of success. The best results are seen with the parameters $S_{\text{Angles}}$ , $C_{\text{Ort}}$ and $S_{\text{Ort}}$ . For each parameter, the non monotonic behaviour in the data can be attributed to the influence of the substrate on the crack pattern. At low layers heights, wavy cracks are observed for plates 1,2 and 3, the amplitude of wavy cracks is directly controlled by the wavelength of the substrate, hence the plates exerts influence on the crack pattern even at low layer heights. For all the three parameters $S_{\text{Angles}}$ ,$C_{\text{Ort}}$ and $S_{\text{Ort}}$ the peaks in the data occur at intermediate layer heights $h \approx 0.5$ for plates with $A/\lambda = 0.25$ and $h \approx 1.0$ for plates with $A/\lambda = 0.5$. At these layer heights, there is a correlation between the crack pattern and substrate, hence ladder-like crack patterns are observed. The region of large heights yields some interesting results as well. It is observed in the data for all measurement parameters that for plates with $A/\lambda = 0.5$, a constant value is reached after $h \approx 1.5$, this value as, shown for $S_{\text{Angles}}$ and $S_{\text{Man}}$ falls within the error range of measurements made on crack patterns generated on the flat plate.

What is consistently true for all measurement parameters is that there is data collapse between the sinusoidal plate data and the radially sinusoidal plate data depending on the $A/\lambda$, the small differences, especially observed for $S_{\text{Ort}}$ are aberrations compared to consistent agreement that the radial plate data has with the sinusoidal plates. The Fourier methods developed in this chapter are interesting tools to analyse crack patterns. These methods capture well the transition from two crack per wavelength to a single crack per wavelength, that occurs around the peaks in the data of the measurement parameters.

Lastly, the crack spacing remains unchanged with increasing layer height, showing no drastic changes as the crack pattern undergoes transitions. The crack spacing, in its current form, may not be the most illuminating tool to characterize crack patterns over sinusoidal substrate. The various height of the cracking layer must be taken into account while comparing the crack spacing with the thickness of the cracked layer.

The second question posed in the beginning of the chapter was is what are the strengths and weakness of each method? The methods $S_{\text{Angles}}$ ,$C_{\text{Ort}}$ and $S_{\text{Ort}}$ have very little difficulty in measuring crack patterns. $S_{\text{Ort}}$ is not particularly suited for analysing wavy crack patterns since it is unaffected by the local structure of the crack pattern.$S_{\text{Ort}}$ is also not well suited for measuring crack patterns with very few cracked regions, but this restriction applies to all parameters since any measurements on very few cracks will not yield a significant result. $S_{\text{Man}}$ struggles at low layer heights and very large layer heights. This is because at low layer heights it is difficult obtain a well connected network, and at large layer there are very few vertices hence only a small number of pairs can be formed leading to $S_{\text{Man}}$ with large fluctuations. While the method is useful to provide global measures for ladder-like and isotropic crack patterns at intermediate and high layer heights, newer ways of neighbour

detection are needed for better results at low and very large layer heights. One can argue that since beyond $h \approx 2$ no new changes in the crack pattern are seen. This is true to a large extent. However, to generalize the method, it must be well defined within the conditions that is defined in. Therefore, a with better neighbouring algorithms algorithms, the $S_{Man}$ parameter has the potential to be an extremely good measure of crack patterns.

The final question posed during the introduction was what is the realm of applicability of each crack pattern measures? For almost all parameters, crack patterns at large extremes of low and layer heights pose problems. At low layer heights, the crack pattern is not well connected and, as stated earlier, a well connected network is essential to measure crack patterns with the current algorithms. With the except of $C_{Ort}$ and $S_{Ort}$ , all the other parameters require a well connected skeleton image for neighbour detection which is needed calculate the final result. At large layer heights, the methods break down due to different reasons. The measures $S_{Ort}$ and $C_{Ort}$ have too few regions and cracks to measure hence any measurement will not be statistically significant, this is readily seen in the large scatter in their data at high layer heights. Out of all the parameters, $S_{Man}$ is best used for distinguishing ladder-like cracks from isotropic cracks, although the range of values of $S_{Man}$ are small. It is also useful since it is a global measure of the crack pattern. Fourier methods can be applied at all layer heights and yield consistent results, they are best applied to periodic patterns like the ones presented in this thesis. The generality applicability of Fourier methods to other types of crack patterns remains to be explored.

In chapter 1 of this thesis, it was mentioned that the attempt was to address two issues- one was to develop methods to analyse crack patterns and second was to apply this to crack patterns generated on uneven substrates. The work until now has focused one type of uneven substrate, which is the sinusoidal substrate with two different symmetries. Methods have been developed to analyse these sinusoidal crack patterns. In the upcoming chapter, new systems with uneven substrates are presented and how the existing parameters can be applied to such systems will be discussed.

# Chapter 6

# Future directions

Crack patterns form at various length scales. In the previous chapters, crack patterns were studied on the centimeter scale and methods were developed to analyse them. Crack patterns are however prevalent at many length scales. In the introductory chapter, examples of crack patterns at the micro meter and the kilometer scale were shown. In this chapter, these length scales will be further explored and the findings of the thesis briefly applied.

Two approaches are presented in this chapter. One approach looks at extending the current experimental system to include sinusoidal substrates at the micro scale. This approach is useful since it provides a means to check if the methods of crack pattern quantification would carry over to lower length scales. It is reasonable to expect certain differences at the micro scale when it comes to cracking since various factors such as interfacial forces, electrostatic forces of the deposited material, the ratio of the particle size to the wavelength of the sinusoidal structure of the substrate would all be factors that affect the drying process and the final crack pattern. Furthermore, if the material properties of the cracking medium or the substrate are chosen inappropriately, then the deposited material may not even form cracks. Hence it is imperative to ensure that the right type cracking material and substrate are selected.

The main focus of this section is the fabrication of a sinusoidal substrate which is done generating wrinkling instabilities on Polydimethylsiloxane (PDMS). Previous literature on the various methods to create wrinkling instabilities in PDMS are discussed followed by the experimental details for creating wrinkle patterns. These pattern are characterized by using atomic force microscopy, some result of these characterization are also shared.

The second approach, looks towards large length scales. In the introductory chapter, crack patterns over craters were mentioned and as an example, the existence of graben patterns on Mercury's craters was briefly discussed. Inspired by these patterns, an attempt is made to study contraction cracks on craters. Since it is not possible to fill in real craters with mud and dry them, craters from the surface of Mars were selected and scaled down to be used as substrates. These scaled down substrates were 3d printed and it was ensured that not just the crater but the terrain around it was also properly scaled. Martian craters were chosen primarily due to availability of high resolution images of the planet's surface. Once the craters were fabricated, bentonite slurries were deposited onto these miniature craters

and crack patterns generated on them were studied. Finally, the chapter ends with a general summary providing a brief recap of all the chapters.

## 6.1   Surface buckling on PDMS

The work carried out in this section was the outcome of a collaboration with Alina Mielke [66]. Details about the experimental methods and measurements are found in her Bachelor thesis titled : "Wrinkling Instabilities in PDMS".

Wrinkling or buckling instabilities are created by holding a sheet under tension or compressing them. A common example is stretching a rectangular sheet of plastic. When such a sheet is pulled along its long axis, buckles will form perpendicular to the applied tension. On the other hard compressing an elastic sheet will also create buckles [22]. For a bulk medium, buckling is induced by stretching or compressing a substrate and the depositing a stiff film to substrate. Once the substrate is relaxed, the elastic mismatch between the stiff film and the soft substrate will cause buckling. An argument of energy balance between the bending energy of the film and the deformation energy of the substrate can be used to write down a relationship between the thickness of the film atop the substrate and wavelength of the buckling instability ( [17, 82, 13] )

$$\lambda = 2\pi t \left( \frac{E_f \ (1 - \nu_s)}{E_s \ (1 - \nu_f)} \right)^{1/3} \tag{6.1}$$

where $E_f$ is the Young's modulus of the substrate, $\nu_f$ is the Poission's ratio of the film, $\nu_s$ Poission's ratio of the substrate and $t$ is the thickness of the film.

PDMS is used as the soft substrate since it is easy to control its stiffness. There are various methods to create buckles on the surface of PDMS-

1. Bowden et al. [17] used three different methods to create buckles the surface of PDMS. The first method involved heating PDMS block, then depositing a 5 nm titanium film, followed by a 5 nm gold film. As the PDMS cools, buckles with a wavelength of $\lambda \backsim 50 \mu$m form atop the surface of the PDMS.

2. Another method described by Bowden et al. is to heat the PDMS substrate, expose it to $O_2$ plasma and cool down the same.

3. Bowden et al. produced buckles by oxidizing the surface of PDMS and compressing it. Buckles created in such a way are parallel to each other.

4. Chan and Cosby, [23] fabricated ripples on the surface of PDMS by swelling a block of PDMS and a layer of silicate in the same system. The silicate does note swell greatly. Since the silicate and the PDMS are bonded to the PDMS, as the PDMS tries to expand beyond the interface length of the silicate, buckles form.

5. Stafford et al. [82] deposit polystyerene films atop PDMS substrates and gently compress the substrate to create buckles atop the PDMS.
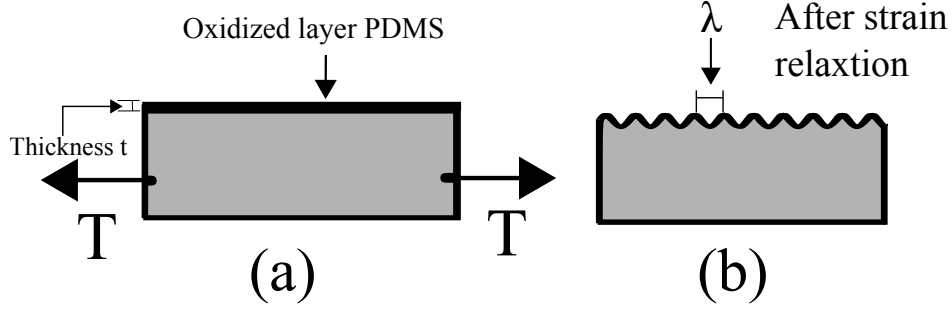
Figure 6.1: Inducing buckles on the surface of PDMS. Figure (a) A block of PDMS is pulled and held with tension T. The surface is exposed to plasma, the top layer of the PDMS oxidizes. Figure (b) : the strain is removed, as the block of PDMS relaxes, surface ripples form.

Above are some of the most common and successful methods to create ripples atop PDMS. In the current experiments, method 2 was used to create sinusoidal buckles. The schematic in figure 6.1 gives a brief outline of the process.

The PDMS blocks were prepared using SLYGARD silicon elastomer and curing agent, a ratio of 5:1 elastomer were mixed together, degassed and baked for an hour at 65°. The ratio of 5:1 was chosen to ensure that the PDMS was soft enough to be cut into rectangular pieces of length 1 cm by 0.5 cm. The thickness of these pieces varied between 0.1-0.3 cm.

The pieces of PDMS were put into the setup where they of PDMS were clamped and stretched to induce 33%, 50% or 66% strain. The whole setup was put into a plasma cleaner, and exposed to plasma for 10-30 minutes based on the experiment. The setup was removed from the plasma cleaner and left to cool, after which the PDMS pieces were slowly relaxed and removed.

A sign of buckle formation is iridescent colour observed in the region of plasma exposure (figure 6.2 (b)) which occurs due to diffraction. The plasma exposed samples were then scanned using an atomic force microscope (AFM) and the wavelength was measured for varying conditions. Table 6.1 provides a summary of the results. It shows the change in the wavelength with oxidation time and strain ([66]). It was observed that with large oxidation times the wavelength increases. The [72] change in stiffness or the height of the oxidation layer due to expose to plasma has not been studied in depth, however it is known that the atomic composition does get al.tered when it is exposed to oxygen plasma [72, 17]. Looking at equation 6.1, it is possible that with increasing oxidation times the stiffness of the film also goes up. This idea reconciles with the observation that at larger oxidation times, there are more cracks. The increase in crack density could also be due to an increase in the stiffness of the film. The change in the wavelength with the strain was also measured. No significant change in the wavelength was observed with the change in strain. This is consistent with equation 6.1.

The largest wavelength of buckles seen using the current methods is approximately $\lambda \approx$ 4 $\mu$m. In general, a wavelength of $\lambda \approx 1$ $\mu$m was the most reproducible with the least amount of variation in the wavelength. While nanometer sized particles can be dried to create crack

Table 6.1: Variation of wavelength $\lambda$ with oxidation time and strain.

| Time (min) | $\lambda$ (nm) | std.dev |
|------------|----------------|---------|
| 10.0 | 924.5 | 158.5 |
| 20.0 | 1610.0 | 277.4 |
| 30.0 | 4124.0 | 367.7 |

| Strain% | $\lambda$ (nm) | std.dev |
|---------|----------------|---------|
| 50.0 | 1753.0 | 171.5 |
| 66.0 | 1766.7 | 217.3 |

patterns on such a surface, the difference between the wavelength and size of the particles is still too small. The next step, is to find means to increase the wavelength of the buckles. This can be done by attempting the same experiment with compression, rather than stretching.

The best cracking material at the micro scale would be colloids. For instance, Polystyrene beads with a diameter of 20 nm are available and would be well suited as a cracking medium. An other option is to use silica particles, they are available with diameters as small as 11 nm [87]. [61].

Attempts have been made here to make sinusoidal substrates that are similar to the macroscopic experiments. Fabrication of controlled uneven substrates at the micro scale are necessary to study cracking at the micro scale. Various methods have been presented which can be explored further to fabricated sinusoidal micro substrates. Due to variety of other interactions between the constituents of the system ( the cracking material, the substrate), there are many options to explore in cracking in uneven substrates at the micro scale.
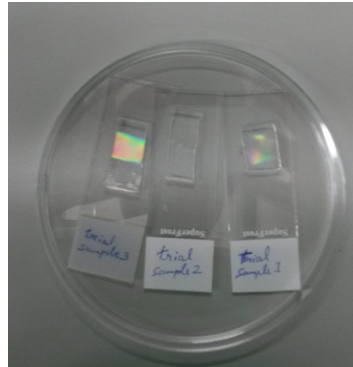


Figure 6.2: Image shows three samples of PDMS which were stretched, exposed to plasma and relaxed. Iridescent color is observed on the surface of the PDMS pieces.

## 6.2 Crack patterns in craters

The work in this section was carried out in collaboration with Emmanuel Tobias Regenhardt as part of his MSc lab course.

Crack patterns in craters are studied by scaling down the structure to the centimeter scale and drying bentonite slurries atop them. On the geological scale, crack patterns or graben patterns have been studied on the surfaces of Mercury and Mars [34]. However, these are mature crack patterns whose substrates are inaccessible. In many cases, the substrates are buried around hundreds of meters below surface of a planetary body. Knowing the structure of
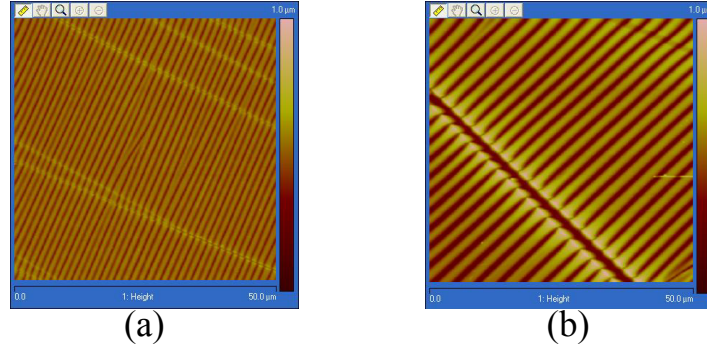
<div align="center">(a)               (b)</div>

Figure 6.3: AFM scans of buckles in PDMS. (a) AFM scan of PDMS where 50% strain is applied to the sample. The sample is oxidized for 20 minutes, the amplitude is $\lambda \approx 1350$nm. (b) AFM scan of PDMS where 33% strain is applied to the sample. The sample is oxidized for 30 minutes. The amplitude is $\lambda \approx 2600$nm. The $A/\lambda$ ratio is approximately 0.1.

the substrate, experiments can be performed at the meter scale in order to better understand how these crack patterns form at such large length scales. While the exact conditions may not be reproducible (for example factors such as- strength of gravity, the thermal conditions, volcanic activity cannot be easily reproduced), it is still illuminating to study geological structures as substrates for crack pattern since they will highlight the difference of how crack patterns form on Earth and other planetary bodies.

Craters are chosen as the substrates to study crack patterns because craters are ubiquitous on the surface of most planetary surfaces. Open craters and buried craters have been observed on the surfaces of Mercury, Venus, Mars, Earth, Moon and many of Jupiter's moons. Craters have been extensively studied from a geophysical perspective [65, 64, 35] . Attempts have been made to create surface profiles of cracters through throught high speed impact experiments in sad beds. [79, 27]. Craters also have a radial symmetry which makes it ideal for application of the various measurement parameters that have been developed in the previous chapters.

A Martian crater was used as a model crater (figure (6.4) since high resolution images of the crater was available. In figure 6.4 the color represents the elevation. Using the elevation data, a 3d model were generated. This model is shows in figure 6.5. The 3d model was fabricated using CNC milling. The substrate is 10 cm by 10 cm. The diameter of crater is approximately 3.4 cm and the depth of the crater is 1.6 cm. The aspect ratio is approximately $depth/diameter$ 0.47

Mud cracks were generated on the crater by drying Bentonite slurries prepared with 1:2 ratio of Bentonite to water. These slurries were deposited on the substrate and left to dry for anywhere between 2-6 hours based on the layer height. The slurries were dried at room temperature.

Figure 6.6 is a raw image of a a crack pattern generated at low layer height where $H_c = 0.16$ cm. The value of $H$ is made dimensionless by dividing the wet layer height for a given bentonite mass in a flat plate of dimensions 10 cm by 10 cm by the depth of the crater. Hence at $h_c=1$ the wet layer height in a flat box of dimension of 10 cm by 10 cm would be the same height as the depth of the crater. Hence, the layer height in figure 6.6 becomes

<div align="center">97</div>

$H$/depth of crater $= h = 0.1$. At the largest layer height, there is a circular crack. The diameter of this circular crack is smaller than the diameter of the crater. There are no cracks inside the primary circular crack that is inside the crater. There are cracks that radially spread outwards from the circular primary crack but terminate near the inner edge of the crater.

Figure 6.7 shows binary images crater crack patterns at figure (a) $H = 0.20$ cm and figure (b) $H = 0.38$ cm . In Figure 6.7 (a), some radially outward cracks are present whereas no radial cracks are present in figure (b). As the layer height increase, while the circular crack remains, the radial cracks disappear which suggests that with increasing layer height information about the structure of the crater is lost.

In the current experimental set-up, only a small region around the crater is selected, however, the region around a crater can also make for interesting surfaces to study cracking. The regions around a crater tend to have smaller craters and ejecta patterns. Evidence of this can be seen in figure 6.4 (a) where there are smaller craters that dot the landscape, these could be smaller pieces of a fragmenting body. Figure 6.4 (b) contains ejecta patterns that surround the crater which has radial symmetry.

## Summary

At the micro scale, experiments were performed to fabricate sinusoidal substrates by oxidizing the surface of rectangular pieces of PDMS with oxygen plasma while they were stretched. The PDMS pieces were scanned with an AFM, buckles were observed on the surface. The buckles were characterized and it was found that the wavelength increased with increasing oxidation time. The largest wavelength of $\lambda \approx 4$ $\mu$m was achieved for 30 minutes of plasma exposure. Apart from the current method to construct sinusoidal substrates, various other methods were presented as well. In order to continue these experiments, it would be essential to investigate and identify the best method of fabricating sinusoidal substrates. While the current methods is easily implementable the range of wavelengths is not sufficient for cracking experiments.

On large length scales, a Martian crater was scaled down and mud cracks were generated on its surface by drying bentonite slurries. The crack pattern in and around the craters were observed to have radial symmetry. The scaled down version of a crater must be further explored at larger layer heights. Craters are the starting point of geological structures that represents uneven substrates. Another example of geological structures that can be studied are dried river beds.

The micro scale and the kilometer scale systems show promise in further exploring and better understanding the effect of uneven substrates on a crack pattern. These two directions are pertinent extensions to the current set of experiments. They will also assist in refining or even redefining the measures of a crack pattern.
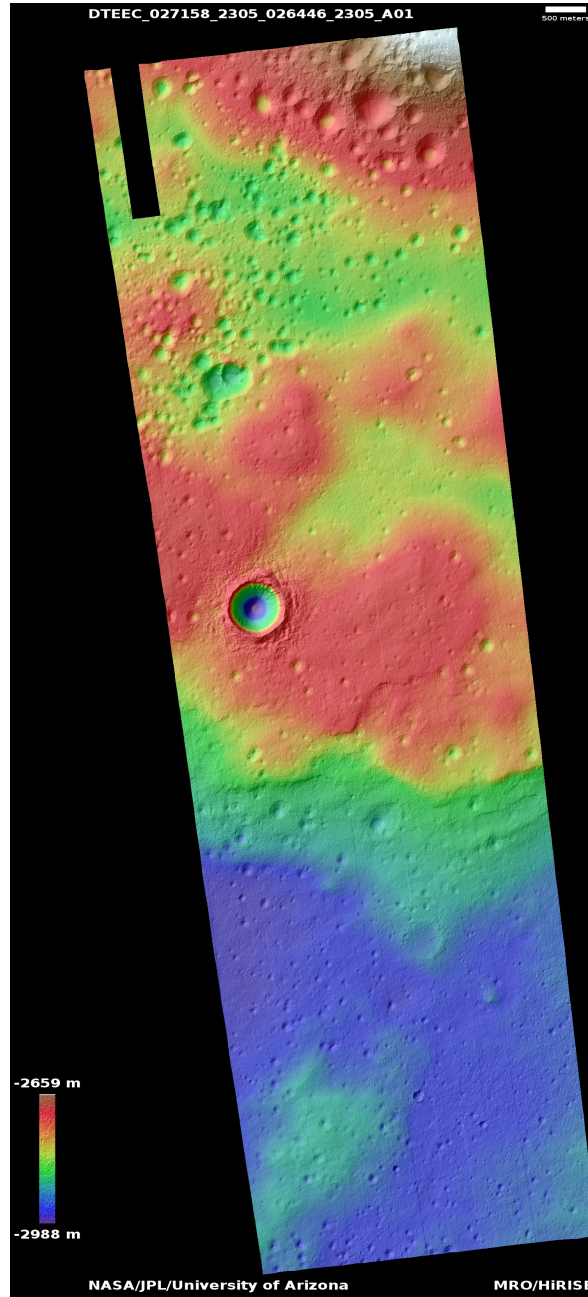
Figure 6.4: Satellite image of the Northern plains crater. The image resolution is 0.99 meters/pixel. The scale bar on the top right of the image read 500 meters. Image: NASA/JPL/University of Arizona.
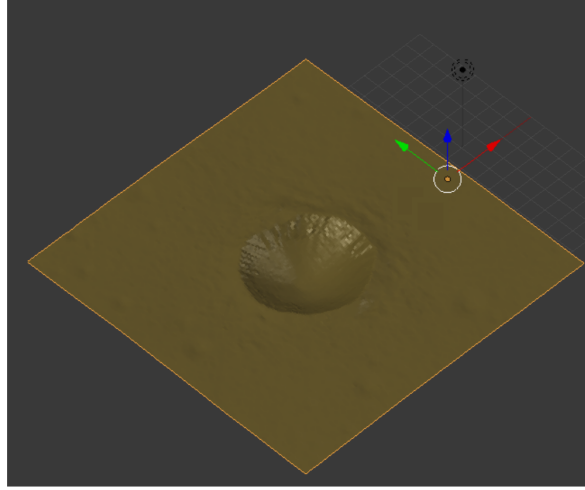
Figure 6.5: 3d model of crater. This model was created using Blender [25] which converts the color to height and generates a 3d model. The 3d model was scaled down and cropped.



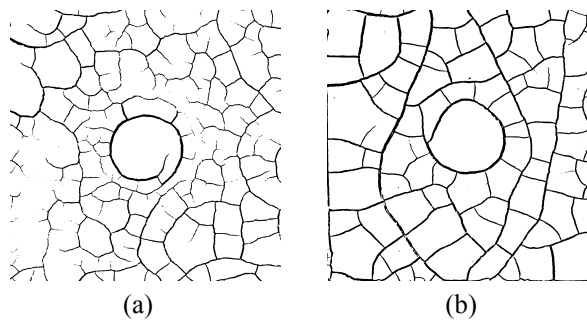Figure 6.6: Raw image of cracks in a crater. The wet layer height here is $H = 0.16cm$.



Figure 6.7: Binary images of crack patterns generated over a crater. In figure (a) $H = 0.20$ cm and in figure (b) $H = 0.38$ cm.

# Conclusion

In the beginning of the thesis, two questions were asked. How can crack patterns be quantified? and what is the influence of an uneven substrate on a crack pattern? To answer these questions, crack patterns were generated on sinusoidal plates and radially sinusoidally plates by drying Bentonite slurries. The dominant control parameter in generating these crack patterns was the dimensionless layer height $h = \mathrm{H}/\lambda$. The generated crack patterns were roughly classified into three types- wavy, ladder-like and isotropic. These crack pattern were analysed using various methods.

First of these methods was using Fourier methods to study if there was a connection between the periodicity of the crack pattern and the substrate. It was found that at certain layer heights there are two cracks per wavelength and there is a transition to one crack per wavelength. As this transition occurs, the crack pattern becomes increasingly ladder-like. At large layer heights no relation between the crack pattern and substrate.

Next, measures of a crack pattern were developed by using the symmetry of the substrate and the geometry of the crack patterns. The measurement parameters $S_{Angles}$, $C_{Ort}$ were developed by calculating the angle distribution of the cracks and condensing it to a single number.$S_{Ort}$ which is the orientation of cracked regions was calculated by measuring the orientation each cracked piece and averaging it.$S_{Man}$ used a Manhattan metric type approach to calculate the ratio of the Euclidean distance between two crack intersection point and the distance traveled along the crack pattern. All these parameters, except $S_{Ort}$, provided hint towards a dimensionless layer height where the influence of the crack pattern is the strongest. Incidentally, this point lies at the end of a region where the crack pattern transitions from two cracks per wavelength to one crack per wavelength which is observed in the analysis of the crack patterns using Fourier methods.

To analyse how uneven substrates affect crack patterns, quantification of the crack pattern was required. This quantification was provided by the various measurement parameters. Hence, the answer to the first question was required to answer the second question i.e both question are intertwined. The effect of an uneven substrate cannot be studied without developing adequate methods which quantify a crack pattern.

Furthermore, a model based on Griffith' criteria was introduced. This model maximized the strain energy released due to the crack and showed that there is a transition between wavy and ladder-like cracks. It predicted that at low layer height, there are two maxima of strain energy release and that with increasing layer height the cracks occur atop the peaks. The experimental data supports the model.

While, measurement methods have been developed during the course of this work, more needs to be done. The current set of experiments were restricted to the centimeter scale, suggestions for experiments at the kilo-meter scale and the micro meter scale were also furnished. In conclusion, crack patterns at various length scales must be studied and the presented measurement parameters must be improved upon or redefined in the context of the system to better understanding of how uneven substrates affect crack patterns.

# Acknowledgements

Firstly I would like to thank Dr. Lucas Goehring who is my Ph.D. advisor. He taught me many invaluable lessons, both in physics and life. He was always available for the silliest of questions, his patience and willingness to engage at a moment's notice has been a pillar of support through my Ph.D. I could not have had a better advisor than him.

I would like to thank my family, My mother Rukmini, dad Nandakishore, and sister Pallavi. Their constant love,affection and support through the years kept me going. Any successes I have, I owe it all to them.

I thanks my lab mates - Antoine Fourriere. He has always been kind and supportive. He provided a welcoming atmosphere in the lab. He patiently listened to my bad ideas and helped me refined the good ones. His suggestions especially with the image analysis were very useful. I would also like to thank Arnaud Hemmerle, for his help with the x-ray nanotom. He has always been helpful at fassberg. Thanks to (Jan) Sudaporn Vesaratchanon, (Shaka) Shaghayegh Javadi, Pree-Cha Kiatkirakajorn. I thank my student Tobias-Emanuel Regenhardt and Alina Mieke, I do not know how much I have taught but I learnt a lot from interacting with them. Herr Morris Wolff for fabricating the levelling plates and in general helping out in the lab, Herr Udo Schmeinke for patiently listening to my questions and fabricating the sinusoidal substrates. Marco Mazza,Eleni katifori, Jonathan Dawson for all the advice and motivation during my Ph.D.

I would like to thank my friends Ankit Awasthi , Heena Sharma, Kundan Sharma, Veena Anjana J, jai Vinita Bharat, Avani Shukla, Sumir Pandit. You guys gave me a real sense of family away from home. Ankit- for all the great discussions, intellectual and otherwise, Heena- for all the fun moments and arguments, Kundan for eternally being the comic relief and helping me out in times of need, Avani- for all the great times we have had through the years, Vinita- for listening to all my bad jokes and the immense amount of emotional support, especially during thesis writing, Veena for being a little rock, pragmatic and sharing all the poor jokes with me, showing me the joy of cooking, Sumir- mainly for food, but also in general for the great company, and shrikand.

I would like to thank Oliva Saldanha, for all the bad and the good times we shared together from Mysore to Göttingen. I was great to have your support all these years through my Ph.D. Puneet Murthy for his constant sense of encouragement and drive to do better.

I would like to also thank Shashi Thutupalli for all the support he gave me when I arrived here. His mentor-ship and advice has been invaluable. Tanmoy for being their, it was amazing fun with you being around. I thanks Mayur Vadhvani, Shalaka Wahane, Varun

Thakre, Anjali Singh, Sonia Baloni, Sharath Dantu, Shweta Agarwal and Ishwar for all the good times in Göttingen.

Last, but surely not the least, I would like to thank two teachers, my high school teacher Mr.Lacarte, he instilled in me the drive to pursue whatever I wanted. His guidance serves me well to this day, and secondly Master Yoda, he is an ocean of knowledge, guiding light to this.

# Bibliography

[1] Image j, band pass filter. `http://imagej.nih.gov/ij/plugins/fft-filter.html`.

[2] FS Abas and K Martinez. Craquelure analysis for content-based retrieval. In *Digital Signal Processing, 2002. DSP 2002. 2002 14th International Conference on*, volume 1, pages 111–114. IEEE, 2002.

[3] SM Allameh, J Lou, F Kavishe, T Buchheit, and WO Soboyejo. An investigation of fatigue in liga ni mems thin films. *Materials Science and Engineering: A*, 371(1):256–266, 2004.

[4] John Robert Laurence Allen. Desiccation of mud in the temperate intertidal zone: studies from the severn estuary and eastern england. *Philosophical Transactions of the Royal Society of London. Series B, Biological Sciences*, pages 127–156, 1987.

[5] Christian André Andresen, Alex Hansen, Romain Le Goc, Philippe Davy, and Sigmund Mongstad Hope. Topology of fracture networks. *arXiv preprint arXiv:1203.4510*, 2012.

[6] T Bai, DD Pollard, and H Gao. Explanation for fracture spacing in layered materials. *Nature*, 403(6771):753–756, 2000.

[7] Raph B Baldwin. Lunar crater counts. *The Astronomical Journal*, 69:377, 1964.

[8] W Bruce Banerdt and Charles G Sammis. Small-scale fracture patterns on the volcanic plains of venus. *Journal of Geophysical Research: Planets (1991–2012)*, 97(E10):16149–16166, 1992.

[9] Gustav Berger and William H Russell. *Conservation of paintings: research and innovations*. Archetype Publisher, 2000.

[10] Gustav A Berger and William H Russell. An evaluation of the preparation of canvas paintings using stress measurements. *Studies in conservation*, 33(4):187–204, 1988.

[11] Gustav A Berger and William H Russell. Deterioration of surfaces exposed to environmental changes. *Journal of the American Institute for Conservation*, 29(1):45–76, 1990.

[12] JL Beuth. Cracking of thin bonded films in residual tension. *International Journal of Solids and Structures*, 29(13):1657–1675, 1992.

[13] Maurice A Biot. General theory of three-dimensional consolidation. *Journal of applied physics*, 12(2):155–164, 1941.

[14] David M Blair, Andrew M Freed, Paul K Byrne, Christian Klimczak, Louise M Prockter, Carolyn M Ernst, Sean C Solomon, H Jay Melosh, and Maria T Zuber. The origin of graben and ridges in rachmaninoff, raditladi, and mozart basins, mercury. *Journal of Geophysical Research: Planets*, 118(1):47–58, 2013.

[15] S Bohn, S Douady, and Y Couder. Four sided domains in hierarchical space dividing patterns. *Physical review letters*, 94(5):054503, 2005.

[16] S Bohn, J Platkiewicz, B Andreotti, M Adda-Bedia, and Y Couder. Hierarchical crack pattern as formed by successive domain divisions. ii. from disordered to deterministic behavior. *Physical Review E*, 71(4):046215, 2005.

[17] Ned Bowden, Wilhelm T. S. Huck, Kateri E. Paul, and George M. Whitesides. The controlled formation of ordered, sinusoidal structures by plasma oxidation of an elastomeric polymer. *Applied Physics Letters*, 75(17), 1999.

[18] Ned Bowden, Wilhelm TS Huck, Kateri E Paul, and George M Whitesides. The controlled formation of ordered, sinusoidal structures by plasma oxidation of an elastomeric polymer. *Applied Physics Letters*, 75(17):2557–2559, 1999.

[19] Spike Bucklow. The description of craquelure patterns. *Studies in Conservation*, 42(3):129–140, 1997.

[20] Spike Bucklow. The description and classification of craquelure. *Studies in Conservation*, 44(4):233–244, 1999.

[21] DL Buczkowski, DY Wyrick, KA Iyer, EG Kahn, JEC Scully, A Nathues, RW Gaskell, T Roatsch, F Preusker, PM Schenk, et al. Large-scale troughs on vesta: A signature of planetary tectonics. *Geophysical Research Letters*, 39(18), 2012.

[22] Enrique Cerda and Lakshminarayanan Mahadevan. Geometry and physics of wrinkling. *Physical review letters*, 90(7):074302, 2003.

[23] Edwin P Chan and Alfred J Crosby. Spontaneous formation of stable aligned wrinkling patterns. *Soft Matter*, 2(4):324–328, 2006.

[24] François Chaumette. Image moments: a general and useful set of features for visual servoing. *Robotics, IEEE Transactions on*, 20(4):713–723, 2004.

[25] Blender Online Community. Blender - a 3d modelling and rendering package,

[26] Arturo Corte and Akira Higashi. Experimental research on desiccation cracks in soil. Technical report, 1964.

[27] John R de Bruyn and Amanda M Walsh. Penetration of spheres into loose granular media. *Canadian Journal of Physics*, 82(6):439–446, 2004.

[28] Nicholas J Douville, Zhengyu Li, Shuichi Takayama, and MD Thouless. Fracture of metal coated elastomers. *Soft Matter*, 7(14):6493–6500, 2011.

[29] J Dundurs. Elastic interaction of dislocations with inhomogeneities. *Mathematical theory of dislocations*, pages 70–115, 1969.

[30] M Ramy El Maarry, Jayantha Kodikara, Sasika Wijessoriya, Wojciech J Markiewicz, and Nicolas Thomas. Desiccation mechanism for formation of giant polygons on earth and intermediate-sized polygons on mars: Results from a pre-fracture model. *Earth and Planetary Science Letters*, 323:19–26, 2012.

[31] MR El Maarry, WJ Markiewicz, MT Mellon, W Goetz, JM Dohm, and A Pack. Crater floor polygons: Desiccation patterns of ancient lakes on mars? *Journal of Geophysical Research: Planets (1991–2012)*, 115(E10), 2010.

[32] S Faulhaber, C Mercer, M-W Moon, JW Hutchinson, and AG Evans. Buckling delamination in compressed multilayers on curved substrates with accompanying ridge cracks. *Journal of the Mechanics and Physics of Solids*, 54(5):1004–1028, 2006.

[33] Melissa L Fender, Frédéric Lechenault, and Karen E Daniels. Universal shapes formed by two interacting cracks. *Physical review letters*, 105(12):125505, 2010.

[34] Andrew M Freed, David M Blair, Thomas R Watters, Christian Klimczak, Paul K Byrne, Sean C Solomon, Maria T Zuber, and HJ Melosh. On the origin of graben and ridges within and near volcanically buried craters and basins in mercury's northern plains. *Journal of Geophysical Research: Planets (1991–2012)*, 117(E12), 2012.

[35] Donald E Gault, John E Guest, John B Murray, Daniel Dzurisin, and Michael C Malin. Some comparisons of impact craters on mercury and the moon. *Journal of Geophysical Research*, 80(17):2444–2460, 1975.

[36] Lucas Goehring, Rebecca Conroy, Asad Akhter, William J Clegg, and Alexander F Routh. Evolution of mud-crack patterns during repeated drying cycles. *Soft Matter*, 6(15):3562–3567, 2010.

[37] Lucas Goehring and Stephen W Morris. Cracking mud, freezing dirt, and breaking rocks. *Physics Today*, 67(11):39–44, 2014.

[38] Lucas Goehring, Akio Nakahara, Tapati Dutta, So Kitsunezaki, and Sujata Tarafdar. *Desiccation Cracks and their Patterns: Formation and Modelling in Science and Nature*. John Wiley & Sons, 2015.

[39] Richard Greenberg, Paul Geissler, Gregory Hoppa, B Randall Tufts, Daniel D Durda, Robert Pappalardo, James W Head, Ronald Greeley, Robert Sullivan, and Michael H Carr. Tectonic processes on europa: Tidal stresses, mechanical response, and visible features. *Icarus*, 135(1):64–78, 1998.

[40] Alan A Griffith. The phenomena of rupture and flow in solids. *Philosophical transactions of the royal society of london. Series A, containing papers of a mathematical or physical character*, pages 163–198, 1921.

[41] A Groisman and E Kaplan. An experimental study of cracking induced by desiccation. *EPL (Europhysics Letters)*, 25(6):415, 1994.

[42] Andreas Hafver, Espen Jettestuen, Maya Kobchenko, Dag K Dysthe, Paul Meakin, and Anders Malthe-Sørenssen. Classification of fracture patterns by heterogeneity and topology. *EPL (Europhysics Letters)*, 105(5):56004, 2014.

[43] James W Head, Scott L Murchie, Louise M Prockter, Mark S Robinson, Sean C Solomon, Robert G Strom, Clark R Chapman, Thomas R Watters, William E McClintock, David T Blewett, et al. Volcanism on mercury: Evidence from the first messenger flyby. *Science*, 321(5885):69–72, 2008.

[44] Gregory V Hoppa, B Randall Tufts, Richard Greenberg, and Paul E Geissler. Formation of cycloidal features on europa. *Science*, 285(5435):1899–1902, 1999.

[45] Anil K Jain. *Fundamentals of digital image processing*. Prentice-Hall, Inc., 1989.

[46] Adam Karpowicz. In-plane deformations of films of size on paintings in the glass transition region. *Studies in Conservation*, 34(2):67–74, 1989.

[47] Adam Karpowicz. A study on development of cracks on paintings. *Journal of the American Institute for Conservation*, 29(2):169–180, 1990.

[48] Sheldon Keck. Mechanical alteration of the paint film. *Studies in Conservation*, 14(1):9–30, 1969.

[49] Denis E Kerfoot. Thermal contraction cracks in an arctic tundra environment. *Arctic*, pages 142–150, 1972.

[50] Byoung Choul Kim, Toshiki Matsuoka, Christopher Moraes, Jiexi Huang, MD Thouless, and Shuichi Takayama. Guided fracture of films on soft substrates to create micro/nano-feature arrays with controlled periodicity. *Scientific reports*, 3, 2013.

[51] Byoung Choul Kim, Christopher Moraes, Jiexi Huang, MD Thouless, and Shuichi Takayama. Fracture-based micro-and nanofabrication for biological applications. *Biomaterials science*, 2(3):288–296, 2014.

[52] EM Kindle. Some factors affecting the development of mud-cracks. *The Journal of Geology*, pages 135–144, 1917.

[53] Elissa Koenig and David D Pollard. Mapping and modeling of radial fracture patterns on venus. *Journal of Geophysical Research: Solid Earth (1978–2012)*, 103(B7):15183–15202, 1998.

[54] Arthur H Lachenbruch. Mechanics of thermal contraction cracks and ice-wedge polygons in permafrost. *Geological Society of America Special Papers*, 70:1–66, 1962.

[55] Lev D Landau and EM Lifshitz. Theory of elasticity, vol. 7. *Course of Theoretical Physics*, 3:109, 1986.

[56] Richard C Larson and Ghazala Sadiq. Facility locations with the manhattan metric in the presence of barriers to travel. *Operations Research*, 31(4):652–669, 1983.

[57] Brian R Lawn. *Fracture of brittle solids*. Cambridge university press, 1993.

[58] Renée A Lawton, Colin R Price, Anne F Runge, Walter J Doherty, and S Scott Saavedra. Air plasma treatment of submicron thick pdms polymer films: effect of oxidation time and storage conditions. *Colloids and Surfaces A: Physicochemical and Engineering Aspects*, 253(1):213–215, 2005.

[59] JH Li and LM Zhang. Geometric parameters and rev of a crack network in soil. *Computers and Geotechnics*, 37(4):466–475, 2010.

[60] BK Lucchitta and JA Watkins. Age of graben systems on the moon. In *Lunar and Planetary Science Conference Proceedings*, volume 9, pages 3459–3472, 1978.

[61] Weining Man and William B Russel. Direct measurements of critical stresses and cracking in thin films of colloid dispersions. *Physical review letters*, 100(19):198302, 2008.

[62] Yousuke Matsuo and Akio Nakahara. Effect of interaction on the formation of memories in paste. *Journal of the Physical Society of Japan*, 81(2):024801, 2012.

[63] Michael T Mellon. Small-scale polygonal features on mars: Seasonal thermal contraction cracks in permafrost. *Journal of Geophysical Research: Planets (1991–2012)*, 102(E11):25617–25628, 1997.

[64] H Jay Melosh. Global tectonics of a despun planet. *Icarus*, 31(2):221–243, 1977.

[65] HJ Melosh and CA Williams. Mechanics of graben formation in crustal rocks: A finite element analysis. *Journal of Geophysical Research: Solid Earth (1978–2012)*, 94(B10):13961–13973, 1989.

[66] Alina Mielke. Wrinkling instabilites in pdms. 2013.

[67] KL Mills, Xiaoyue Zhu, Shuichi Takayama, and MD Thouless. The mechanical properties of a surface-modified layer on polydimethylsiloxane. *Journal of materials research*, 23(01):37–48, 2008.

[68] Akio Nakahara, Yuu Shinohara, and Yousuke Matsuo. Control of crack pattern using memory effect of paste. In *Journal of Physics: Conference Series*, volume 319, page 012014. IOP Publishing, 2011.

[69] Hari Singh Nalwa. *Handbook of thin film materials*. Academic Press, 2002.

[70] R Nicholson and DD Pollard. Dilation and linkage of echelon cracks. *Journal of Structural Geology*, 7(5):583–590, 1985.

[71] Nobuyuki Otsu. A threshold selection method from gray-level histograms. *Automatica*, 11(285-296):23–27, 1975.

[72] Michael J Owen and Patrick J Smith. Plasma treatment of polydimethylsiloxane. *Journal of adhesion science and technology*, 8(10):1063–1075, 1994.

[73] Don T Phillips and Alberto Garcia-Diaz. *Fundamentals of network analysis*. Prentice Hall, 1981.

[74] JB Plescia and MP Golombek. Origin of planetary wrinkle ridges based on the study of terrestrial analogs. *Geological Society of America Bulletin*, 97(11):1289–1299, 1986.

[75] David D Pollard, PAUL Segall, and Paul T Delaney. Formation and interpretation of dilatant echelon cracks. *Geological Society of America Bulletin*, 93(12):1291–1303, 1982.

[76] Allan M Rubin. Dike-induced faulting and graben subsidence in volcanic rift zones. *Journal of Geophysical Research: Solid Earth (1978–2012)*, 97(B2):1839–1858, 1992.

[77] Martin H Sadd. *Elasticity: theory, applications, and numerics*. Academic Press, 2009.

[78] VB Shenoy, AF Schwartzman, and LB Freund. Crack patterns in brittle thin films. *International journal of fracture*, 103(1):1–17, 2000.

[79] J Simon and John R de Bruyn. Shape of impact craters in granular media. *Physical Review E*, 76(4):041306, 2007.

[80] Benjamin Sobac and David Brutin. Structural and evaporative evolutions in desiccating sessile drops of blood. *Physical Review E*, 84(1):011603, 2011.

[81] Benjamin Sobac and David Brutin. Desiccation of a sessile drop of blood: Cracks, folds formation and delamination. *Colloids and Surfaces A: Physicochemical and Engineering Aspects*, 448:34–44, 2014.

[82] Christopher M Stafford, Christopher Harrison, Kathryn L Beers, Alamgir Karim, Eric J Amis, Mark R VanLandingham, Ho-Cheol Kim, Willi Volksen, Robert D Miller, and Eva E Simonyi. A buckling-based metrology for measuring the elastic moduli of polymeric thin films. *Nature materials*, 3(8):545–550, 2004.

[83] Michael J Stephen and Joseph P Straley. Physics of liquid crystals. *Reviews of Modern Physics*, 46(4):617, 1974.

[84] Stephen Timoshenko. *Strength of materials*. New York, 1930.

[85] Stephen Timoshenko. *History of strength of materials: with a brief account of the history of theory of elasticity and theory of structures*. Courier Corporation, 1953.

[86] Luca Valentini, Diego Perugini, and Giampiero Poli. The 'small-world' topology of rock fracture networks. *Physica A: Statistical Mechanics and its Applications*, 377(1):323–328, 2007.

[87] Gene Vigil, Zhenghe Xu, Suzi Steinberg, and Jacob Israelachvili. Interactions of silica surfaces. *Journal of Colloid and interface science*, 165(2):367–385, 1994.

[88] Joost J Vlassak. Channel cracking in thin films on substrates of finite thickness. *International Journal of Fracture*, 119(4):299–323, 2003.

[89] Thomas R Watters and F Nimmo. The tectonics of mercury. *Planetary Tectonics*, pages 15–80, 2009.

[90] Z Cedric Xia and John W Hutchinson. Crack patterns in thin films. *Journal of the Mechanics and Physics of Solids*, 48(6):1107–1131, 2000.

[91] T Ye, Z Suo, and AG Evans. Thin film cracking and the roles of substrate and interface. *International Journal of Solids and Structures*, 29(21):2639–2648, 1992.